Single molecule conduction of engineered cytochrome b_{562} bonded to metallic electrodes

Eduardo Antonio Della Pia

A thesis submitted to Cardiff University

for the degree Doctor of Philosophy

School of Physics and Astronomy

School of Biosciences

Cardiff University

March 2011

UMI Number: U585471

UMI

Dissertation Publishing

ProQuest

Abstract

Measuring single molecule conductance is a fundamental step in order to realise the basic elements of future electronic circuits. This work describes the use of an engineered electron transfer protein, cytochrome b_{562} (cyt b_{562}), as a single molecule junction point between a gold surface and a metallic tip through defined thiol-metal interactions. Two separate cysteine residues were introduced in the cyt b_{562} amino acid sequence at strategic positions; the single-molecule conductivity of the two double cysteine mutants SH-SA and SH-LA was investigated using atomic force microscopy (AFM), scanning tunnelling microscopy (STM), current-voltage (I-V) and current-distance (I-z) experiments.

The haem binding properties of the cysteine variants were similar to that of the wild-type cyt b_{562} confirming that the mutations had not altered the protein's core properties. AFM and STM studies revealed that the SH-SA and SH-LA molecules bound to gold electrode in defined orientations, dictated by the thiol-pair utilised. A strong and stable interaction between the proteins bearing the thiol groups and a Au(111) surface was achieved, and a single-molecule conductance of ~ 1 nS was measured in air. In contrast, the unengineered wild-type cyt b_{562} bound much less robustly to the gold surface and the measured conductance was at least one order of magnitude less. Crucially, using electrochemical STM (EC-STM) approaches a change in conductance of the cytochrome over different overpotentials was observed, demonstrating that the molecule can act as an electrochemical gate. The protein became most conducting when the substrate potential was set close to the redox potential of the protein. The electrochemical, I-V and I-z STM measurements suggested a two-step model for electron transfer.

This study illustrates the possibility of exploiting a haem binding protein directly adsorbed onto a conducting surface as a nanoelectronic element and offers new perspectives for future biomolecular electronic circuits.
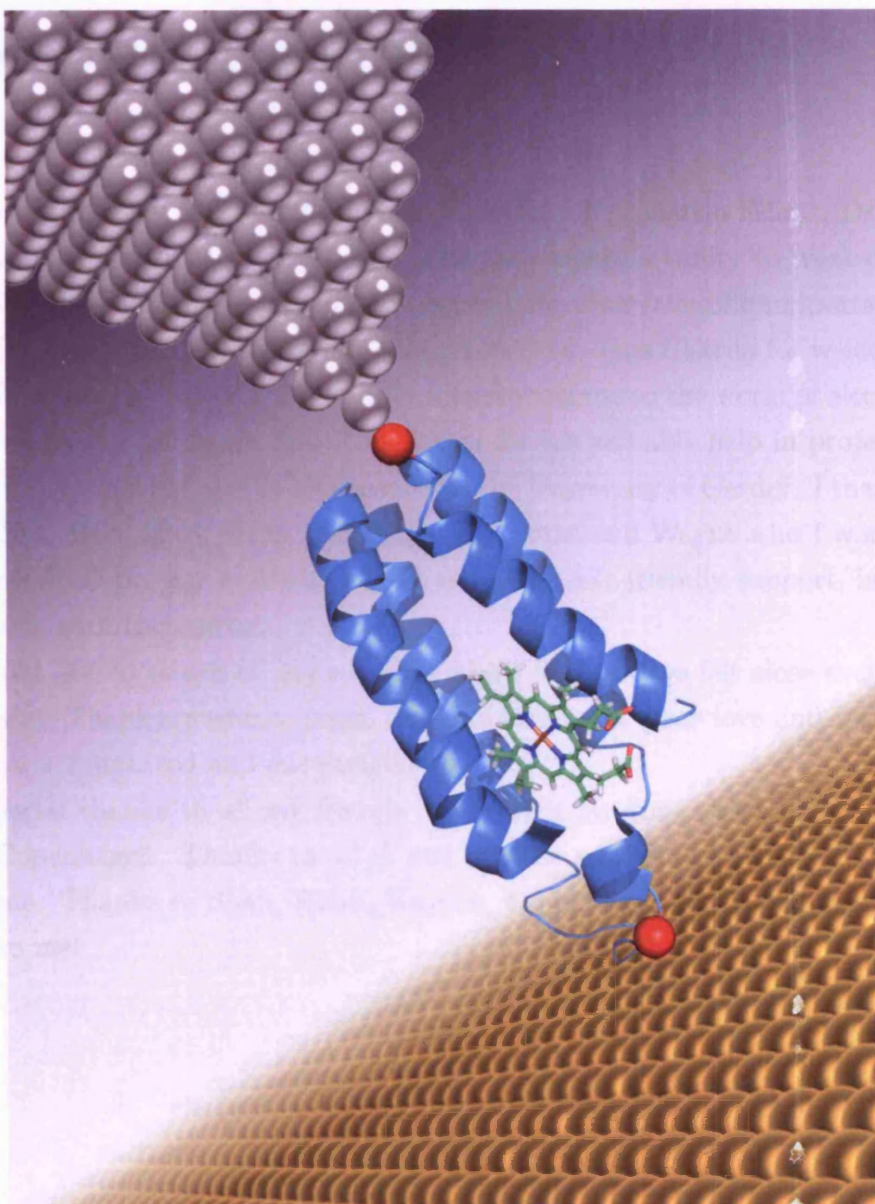
A schematic of a single protein (cytochrome b_{562}) covalently bound to a gold surface and a platinum STM tip.

Acknowledgments

I wish to express my gratefulness to my supervisors Dr. Martin Elliott, Dr. Dafydd Jones and Dr. Emyr Macdonald for giving me the opportunity to work on a very interesting and challenging research project and for their scientific supports. Thanks also to Dr. Qijin Chi, Dr. Jingdong Zhang and Prof. Jens Ulstrup for welcoming me to the NanoKemi group at DTU and for introducing me to the world of electrochemistry. I would like to thank Mr. Rob Tucker for his valuable help in projecting the electronics of the STM and to all the staff at the University of Cardiff. I thank all my friends Neil, Hen, Mark, Ellis, Gengzhao, Pip, Mike and Wayne who I worked with during my PhD project and who helped me with their friendly support, interesting suggestions and discussions.

I would like to thank all my relatives who I have always felt close even if living miles away. Thanks mamma, papà, ada and nonna for your love and because you have always supported and encouraged me.

A special thanks to all my friends met during my time spent living in Cardiff and in Copenhagen. Thanks to all of you because you made the last three years a great time. Thanks to Shah, Rohit, Kayode, Samu, Amy and Keftie, you are very special to me!

Contents

Chapter 1

Introduction

The purpose of this study is to characterize the conduction properties of two engineered cytochrome b_{562} (cyt b_{562}) adsorbed on Au(111) surfaces by scanning probe microscopy. The project aim is related to the need of a better understanding of the conduction mechanism of organic molecules that has risen during the last two decades in the scientific community. The interest in the conductivity of single molecules has been stimulated by the possible realization of molecular electronic devices [25, 121] and significant steps have been made towards their design and fabrication [81, 125].

In particular, strong interest has developed in the nanoscience community in exploiting redox metalloproteins for single molecule electronics and nanosensor devices. Proteins such as cytochrome c, azurin and ferritin have been extensively studied by theoretical and experimental approaches [3, 35, 38, 39, 94, 136]. These self-assembling molecules have evolved over millions of years to optimize molecular recognition of redox-active components and tune the redox properties for their biological function and thus are natural candidates for bioelectronics and biosensors elements [58, 59, 60, 61]. The inherent ability to self-assemble coupled with their capacity to organise and tune redox active components also makes proteins attractive as a scaffold for single molecule components in nanoelectronics [3, 27, 43, 72, 137]. However, the realization of single protein electronic elements seems still to be at the early stage. For instance, both suitable and stable anchoring of proteins onto electrodes and efficient electron-transport at the electrode-molecule interface are still problems to be solved.

Redox metalloproteins represent about a quarter of the known proteins [3]. These biomolecules contain in their active site one or more metal ions that are usually coordinated to the side chains or to the polypeptide backbone. The linked metals (cobalt, copper, iron, magnesium, manganese, molybdenum, nickel) are fundamen-

tal for biological functions (photosynthesis, respiration, catalytic reactions). As their oxidation state can reversibly change they permit the metalloproteins to exchange electrons [61]. These metalloproteins can be subdivided into four families [3]: cytochromes (containing haem groups), copper binding proteins, iron-sulfur complexes, and chlorophyll-based photosynthetic complexes. Specifically some cytochromes (Yeast cytochrome c [21, 22, 42], Horse cytochrome c [10], *E. Coli* cytochrome c [64], cytochrome c_{551} [24]), plastocyanin [6] and ferritin [12] have been studied and modified in order to better understand the natural electron transfer process and to develop new bioelectronic materials. In contrast, to date there have been no comprehensive studies about the electronic properties of the *b*-type cytochromes although they are particularly interesting for the fundamental understanding of the electron transfer process in proteins and for the development of new bioelectronic devices. In fact, as these cytochromes do not link covalently the haem prosthestic group, it is possible to analyse the role of the redox center in the electron conduction mechanism by removing and/or replacing it with other porphyrins modified or containing different metals [115, 126]. Furthermore an extensive study of the electronic properties under physiological conditions of a member of the *b*-type cytochrome family, such as cyt b_{562}, could also help to understand their biological role.

Cyt b_{562} is a particularly attractive protein for use in nanotechnology as a single molecule component. This small, water soluble protein, found in the periplasm of the bacterium *E. coli*, binds non-covalently and modulates the redox properties of haem, an iron-containing porphyrin [13, 49, 76, 78, 79]. The protein has a four α-helix bundle structure (Figure 1.1) and coordinates to the iron of the haem molecule through Methionine 7 and Histidine 102 [13, 69]. The small dimensions, the robust structure, the tolerance to engineering [43], the possibility of tuning its redox potential [112] and of coupling the electron transfer properties to secondary processes [47, 48, 78, 79, 139] make cyt b_{562} an ideal candidate for its integration in hybrid bio-electronic devices. Furthermore, as it does not contain any cysteine residues, thiol chemistry can be precisely defined to allow control over protein orientation on a metal substrate through the introduction of cysteine residues at specific points in the protein structure.

The physical and chemical adsorption of proteins at metallic surfaces is a complex process and is central for the development of molecular electronic devices. In fact, a strong interaction between the adsorbed molecules and metal electrodes is of paramount importance to achieve direct electronic communication. Protein adsorption is governed by Van der Waals forces (attractive or repulsive electrostatic interactions, London dispersion forces) and hydrophobic forces and, if uncontrolled,

typically causes changes of the protein tertiary structure leading to loss of its biological function [40]. Several immobilization techniques have been developed over the past 10 years. Most of them involve the modification of the substrate by the deposition of organic linkers such as self-assembled monolayers presenting thiol groups [24, 51], oxidized single-wall carbon nanotubes [42], charged lipid films and ionic species [94]. These methods have been successfully used to deposit proteins on several substrates, but they do not allow to control the protein surface orientation. Proteins can also be directly deposited on metallic surfaces by using the strong thiol-noble metal interaction (binding energy at room temperature in the range of 85-145 kJ/mol) [38, 95]. The use of naturally occurring linking groups in the protein aminoacidic sequence or the introduction of cysteine residues in the protein sequence via site-directed mutagenesis enables a more controlled, reliable and "site-specific" method to immobilise proteins on metallic substrates. As the physical contact between the molecule and the substrate surface is minimum, the adsorption-induced modifications are minimized too.

Using the "site-specific" technique it has been possible to obtain well defined arrays of proteins and to measure the dimensions of immobilized molecules by scanning tunnelling microscopy (STM) and atomic force microscopy (AFM) [38, 41]. Several researches have also shown that proteins can be contacted between a nanoelectrode and a gold surface enabling measurements of the protein's electric properties [7, 10, 37, 94]. However, even if it has already been shown that the junction contact resistance between two electrodes and small organic molecules can be reduced by several orders of magnitude by exploiting the strong thiol-noble metal interaction [34], the possibility of using two cysteine residues at opposite ends of a protein has never been investigated as a means to contact two separate electrodes.

In this project, exploiting the potential offered by site-directed mutagenesis, cyt b_{562} has been engineered to contain thiol groups at opposite ends of the molecule and to sample two separate orientations: a short axis (SH-SA, sulfhydryl-short axis) and a long axis (SH-LA, sulfhydryl-long axis) (Figure 1.1). Placement of the cysteine mutations was chosen so that binding of only one thiol group to one surface could be possible as steric hindrance would prevent both thiol groups binding in the structured protein; this would leave the second thiol group available to be coupled to a second electrode in a defined manner. The two different orientations were chosen so that the distances between the redox active haem center and/or the two potential surfaces could be altered. Given that the iron center is central to the electron transfer mechanism proposed for redox molecules, it is critical for any electronic applications to investigate the influence of distance to the metallic electrodes on
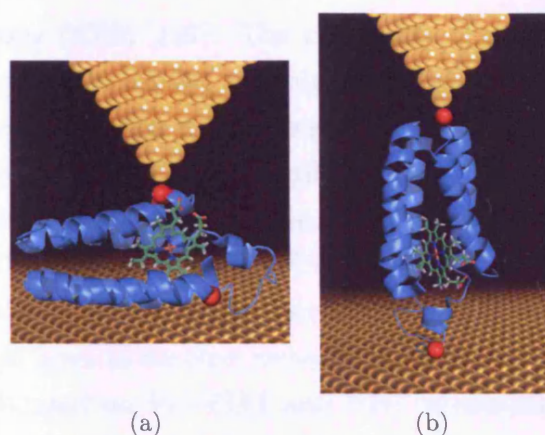
Figure 1.1: Three-dimensional molecular models of the engineered cyt b_{562} (a) SH-SA and (b) SH-LA immobilized onto a gold surface and contacted with a gold STM tip. The relative positions of the amino acid selected for mutation ((a) 5 and 104 and (b) 21 and 50) are highlighted as red spheres and the haem center is shown in the stick representation and coloured green.

the overall protein's conductivity. To generate the SH-SA cyt b_{562} variant, cysteine residues were introduced in place of Asp5 and Lys104. Both these residues are surface exposed on the opposite faces of the long axis of the protein. The targeted residues also lie close to the bound haem and it was anticipated that they orientate haem plane approximately parallel to that of the surface. The iron center is expected to be 12 Å distant from both the two electrodes (Figure 1.1(a)). To generate the SH-LA cyt b_{562} variant, cysteine residues were introduced in place of Asp21 and Asp50. Both these residues are surface exposed and lie at the extreme points of the long axis of the cytochrome. Molecular modelling indicates that SH-LA can anchor metallic surfaces with the iron site being 20 Å and 32 Å distant from the electrodes (Figure 1.1(b)).

Scanning probe microscopy (SPM) techniques can be used to determine the conductance of single molecules [25, 98, 138]. In this study STM has been employed to study the electronic properties of cyt b_{562} adsorbed on Au(111) electrodes. This technique allows to image single molecule adsorbed on a conductive substrate with a resolution of less than 0.1 nm. The STM tip can also be placed above an isolated molecule and current-voltage (I-V$_b$) and current-distance (I-z) measurements of it can be performed [42, 67, 87, 98, 131].

In this study I have also taken advantage of the potentials offered by electrochemistry and electrochemical STM (EC-STM) to display the structure and electronic properties of cyt b_{562} immobilized on pristine Au(111) in a natural, quasi-physiological environment. EC-STM is a technique that combines electrochemical control and STM high-resolution signatures such as molecular imaging and scanning

tunnelling spectroscopy (STS) [137]. The possibility of using EC-STM to observe single-molecule charge transport was speculated upon in the early 1990s [106]. The first experimental demonstration was pioneered by Tao using a system of iron protoporphyrin molecules adsorbed on a highly ordered pyrolytic graphite (HOPG) surface, and the redox-tuned resonant tunnelling effect was directly visualized by EC-STM imaging [117]. Since then, EC-STM has provided a powerful approach to study interfacial electron transfer and molecular conductance of electroactive species at the single-molecule level in an electrochemical environment [98, 137]. However, most studies have focused on EC-STM and STS measurements of small organic molecules in liquid and Azurin has been the only protein extensively studied by EC-STM [27, 30].

Another SPM method that has been considered in this research is tapping mode AFM (TM-AFM). Although it has a lower spatial resolution than STM, it has emerged in the last years as a valid technique for biomolecules imaging studies [22, 94]. Thanks to the low force applied to the scanned sample, the AFM tip does not deform or denature the protein offering a high vertical resolution (sub-Ångstroms) [12, 38]. In this project both STM and TM-AFM have been used to characterize the adsorption modes and the topographic features of the wild-type and of the engineered cysteine mutants cyt b_{562}.

1.1　Dissertation outline

I have carried out the work described in this thesis in the School of Physics and Astronomy and in the School of Biosciences at Cardiff University between September 2007 and March 2011 under the supervision of Dr. Martin Elliott, Dr. Dafydd Jones and Dr. Emyr Macdonald. I have also performed all the electrochemical and EC-STM measurements of the cyt b_{562} in the Nano-Kemi Department at the Technical University of Denmark (DTU) under the supervision of Dr. Qijin Chi, Dr. Jingdong Zhang and Prof. Jens Ulstrup.

The document is organized as follows. The first part of the thesis includes this introductory **chapter 1**. The second part of the thesis includes chapter 2 and 3 and presents the proteins synthesis and the experimental setup used for their characterization in air. **Chapter 2** describes the materials and methods applied for the genomic mutation and the protein expression of the wild-type, the single cysteine variant D50C and the two double cysteine variants cyt b_{562}. It discusses the results concerning the site-directed mutagenesis of the cyt b_{562} DNA, the expression and the purification of the proteins. In the last part of the chapter, the cysteine mutants

absorption spectra and the reconstruction of the proteins with haem are presented and compared with the ones of the wild-type cyt b_{562}. **Chapter 3** outlines the work performed for the design and construction of a home-built STM. It covers some background theory necessary to understand the working principle of STM, describes the mechanical and electronic design and presents atomic resolution images of HOPG and images of Au(111) surfaces.

The third part of the thesis includes chapter 4 and 5 and details the experimental work carried out and the results achieved in the project. **Chapter 4** reviews some of the protein immobilisation methods and some of the results achieved in the characterization of metalloproteins adsorbed on metal electrodes by using SPM techniques. It provides a comprehensive characterization of the cyt b_{562} by using a multitechnique approach based on various SPM experiments (TM-AFM, STM, I-V_b and I-z) performed in air at room temperature. It presents information not only about morphological and electronic properties of the adsorbed molecules, but also about the quality and reliability of electrical coupling with the conductive electrodes. **Chapter 5** presents the electrochemical and EC-STM investigation of cyt b_{562} in buffer solution. It also contains relevant theoretical background of the two-step electron transfer model that has been used to explain the tunnelling mechanism via the redox center of cyt b_{562}.

Finally, **chapter 6** summarizes the main findings of the the project and suggests future research.

Chapter 2

Expression and characterization of cyt b_{562}

This chapter describes the techniques applied and the results obtained in the muta-
genesis and expression of cyt b_{562}. In the first part of the chapter the materials and
the methods for the genetic manipulation and the protein production of cyt b_{562} are
reported. Subsequently, the results concerning the site-directed mutagenesis of the
cyt b_{562} gene, the expression, the purification and the spectroscopic characterization
of the wild-type and the cysteine mutants cyt b_{562} are presented.

2.1 Introduction

Cyt b_{562} (Figure 2.1) is a small soluble electron transfer protein (12.3 kDa) of 106
amino acids isolated from the periplasm of *E.coli*. Figure 2.2 shows both the nu-
cleotide and amino acid sequences of the protein. Cyt b_{562} is an electron transfer
protein but despite being first identified back in 1963 [76], little is still known about
its biological function; it is believed that its function is to shuttle electrons be-
tween other membrane redox partners [112]. The redox active cofactor haem is
non-covalently attached to methionine 7 (helix 1) and histidine 102 (helix 4) and
it is aligned such that the histidine 102 side is solvent accessible and the methion-
ine 7 face is concealed in the protein hydrophobic core. Structural studies (NMR
and X-ray crystallography) have shown that upon haem binding the apo-cyt b_{562}
polypeptide chains (Figure 2.1(b)) undergoes substantial structural changes to a
four-helix bundle with the helices almost packed antiparallel to each other [49, 50]
(Figure 2.1(a)). Particularly the N- and C- termini partially unfolded regions form
helices 1 and 4 creating the hydrophobic haem pocket. Small loops connect the
helices 1 and 2, and the helices 3 and 4, while a longer loop links the helices 2 and 3

(a)   (b)
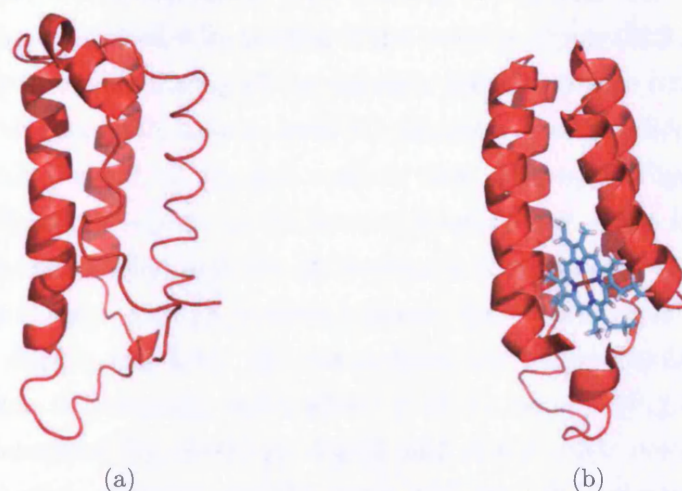
Figure 2.1: Structures of (a) apo-cyt b_{562} and (b) holo-cyt b_{562} (Protein Databank (PDB)). The cyt b_{562} ribbon structure is coloured red, the haem group is shown in light blue.

```
                    20                        40
gcagatcttgaagacaatatggaaaccctcaacgacaatttaaaagtgatcgaaaaagcg 60
 A  D  L  E  D  N  M  E  T  L  N  D  N  L  K  V  I  E  K  A  20
                 80                     100
gataacgcggcgcaagtcaaagacgcgttaacgaagatgcgcgccgcagcgctggatgcg 120
 D  N  A  A  Q  V  K  D  A  L  T  K  M  R  A  A  A  L  D  A  40
              140                     160
caaaaagcaacgccgccgaagctcgaagataaatcaccggacagcccggaaatgaaagat 180
 Q  K  A  T  P  P  K  L  E  D  K  S  P  D  S  P  E  M  K  D  60
                 200                     220
ttccgccacggtttcgacattctggtcggtcagattgacgacgcgctgaagctggcaaat 240
 F  R  H  G  F  D  I  L  V  G  Q  I  D  D  A  L  K  L  A  N  80
                    260                     280
gaaggtaaagtaaaagaagcgcaggctgctgcagagcaactgaaaacgacccgcaacgcc 300
 E  G  K  V  K  E  A  Q  A  A  A  E  Q  L  K  T  T  R  N  A  100
tatcaccagaagtatcgt                                          318
 Y  H  Q  K  Y  R                                           106
```

Figure 2.2: The nucleotide and amino acids sequences of cyt b_{562} are shown. The nucleotide sequence is black numbered, while the amino acid sequence is red numbered.

forming a pocket for the haem positioning [49]. The protein has an overall surface charge of -2 at pH 7 and its dimensions are around 5.1 nm x 2.6 nm [103]. The apo-form of the cyt b_{562} has a very low extinction coefficient ($\varepsilon_{280nm} = 2980$ M^{-1}cm^{-1}) related to the absence of any tryptophan and cysteine residue and to the fact that it contains only two tyrosine amino acids [49, 76].

Cyt b_{562} simple and robust structure and haem-redox properties make it an ideal candidate to investigate and exploit the electronic properties of a protein for nanoelectronics. Furthermore, cyt b_{562} does not contain any naturally occurring cysteine residues (Figure 2.2), thus enabling the introduction of thiols at positions that will allow defined and orientated binding to metal surfaces. In this research two cysteine residues are introduced into cyt b_{562} at defined sequence positions to investigate if good electronic coupling between a redox metalloprotein and noble

metals electrodes can be achieved. The absence of any cysteine residue in the cyt b_{562} amino acid sequence enables control of the position of any thiol group introduced in the protein structure. Among all the possible double cysteine mutations proposed by analysis of the protein's atomic level 3D structure, two possible configuration of the protein with respect to tip and surface were proposed (Figure 1.1). In the first design (SH-SA), the plane of the protein-bound haem group lies parallel to the surface and the distance between tip and surface is at its shortest (Figure 1.1(a)). To implement this design, cysteine residues replaced Asp5 (D5C) and Lys104 (K104C). In the second design (SH-LA), the haem plane lies perpendicular to the surface and the distance between tip and surface is at its longest (Figure 1.1(b)). This design is implemented by replacing Asp21 and Asp50 with cysteines (D21C and D50C, respectively). Control proteins with only one thiol (single cysteine mutant D50C) were also prepared and studied. To shed light on the role of the haem (iron protoporphyrin IX) in molecular conduction, the apo-cyt b_{562} wild-type and D50C single cysteine mutant were also reconstituted with copper protoporphyrin IX (Cu-PP) and the redox-inactive zinc protoporphyrin IX (Zn-PP).

2.1.1   Site-directed mutagenesis outline

To generate the cyt b_{562} cysteine variants site-directed mutagenesis was performed. Site-directed mutagenesis is a molecular biology method that permits the induction of a mutation in a defined site in a DNA molecule. The technique essentially involves the exponential amplification of the original starting gene by polymerase chain reaction (PCR) using the mutageneic synthetic oligonucleotide primers.

With regards to this project, the primers reported in Table 2.1 were used to change the following codons of the cyt b_{562} sequence into cysteine codons:

1. aspartate codon at position 50 GAT→TGT (D50C);

2. aspartate codon at position 5 GAC→TGC and lysine codon at position 104 AAG→TGT (SH-SA);

3. aspartate codon at position 21 GAT→TGT and aspartate codon at position 50 GAT→TGT (SH-LA).

The double cysteine mutations were introduced into cyt b_{562} in a two step process. First, either the D5C mutation or D21C mutation was introduced followed by K104C or D50C, respectively. An outline of how each individual mutation was introduced by a site-directed mutagenesis procedure is detailed as follows.

The plasmids containing the double mutations were amplified by inverse-PCR (I-PCR) using Phusion® high fidelity DNA polymerase. For the first polymerase reaction the template pWRE9 plasmid and the primers DDJcytb001 and DDJcytb002 were used to introduce the mutation GAC→TGC (D5C) (Figure 2.3). Resultant PCR products were stained using ethidium bromide, separated by using agarose gel electrophoresis, visualized by using an UV-transilluminator, excised from the gel and purified. Then the DNA was phosphorylated, ligated, purified and used to transform *E.coli* DH5α. Some colonies were screened by PCR for the presence of the ligated DNA between the *Nde*I and *Xho*I restriction sites of pWRE-9 using the primers pET-F and pET-R (Table 2.2) and *TAQ* DNA polymerase enzyme. The resultant PCR products were separated by using agarose gel electrophoresis, visualized by UV light, and, if showing the expected size (~600 bp), excised from the gel, purified and sequenced. If the correct DNA mutations were confirmed by sequencing, the colony used for PCR screening was inoculated in 5 ml of LB-broth supplemented with ampicillin 100 μg/ml. After overnight growth, the DNA plasmid was extracted and purified by using QIAGEN Plasmid Midi Kit. The plasmid DNA was then used as template for a second polymerase reaction with the primers DDJcytb003 and DDJcytb004. In this way both the mutations (GAC→TGC (D5C) and AAG→TGT (K104C)) were introduced in the cyt b_{562} gene.

The same procedure, using the primers DDJcytb005 and DDJcytb006 in the first I-PCR and the primers DDJcytb007 and DDJcytb008 in the second I-PCR, was applied to amplify a plasmid containing the two mutation GAT→TGT (D21C) and GAT→TGT (D50C). The primers DDJcytb007 and DDJcytb008 were used in a I-PCR to amplify a plasmid containing the single mutation GAT→TGT (D50C).

Table 2.1: Oligonucleotide sequences (Operon Biotechnologies, Cologne, Germany) for generating the cyt b_{562} cysteine mutants.

Primer name	Mutation	Sequence (5' to 3')[a]	Primer pairs[b]
DDJcytb001	D5C	5'-CAGATCTTGAA<u>TGC</u>AATATGGAAACCCTCAACGACAAT-3'	D5C-Sen
DDJcytb002	D5C	3'-CGGCAAACGACGCAGAACTGAATAC-5'	D5C-As
DDJcytb003	K104C	5'-GCCTATCACCAG<u>TGT</u>TATCGTTAACTCG-3'	K104C-Sen
DDJcytb004	K104C	3'-GTTGCGGGTCGTTTTCAGT-5'	K104C-As
DDJcytb005	D21C	5'-GTGATCGAAAAGCG<u>TGT</u>AACGCGGCGCAAGTC-3'	D21C-Sen
DDJcytb006	D21C	3'-TTTTAAATTGTCGTTGAGGGTTTC-5'	D21C-As
DDJcytb007	D50C	5'-CCGCCGAAGCTCGAA<u>TGT</u>AAATCACCGGACAGCCCG-3'	D50C-Sen
DDJcytb008	D50C	3'-CGTTGCTTTTTGCGCATCCAGC-5'	D50C-As

[a]Nucleotides underlined encode the mutations to introduce the thiol pair.

[b]Sen and As refer to the sense and antisense primer, respectively, that comprise the pair

Table 2.2: Primer sequences for pET-F and pET-R.

Primer	Sequence
pET-F	5'-ATGCGTCCGGCGTAGAGGA-3'
pET-R	5'-GCTAGTTATTGCTCAGCGGTG-3'

pWRE-9

PCR

Phosphorylation
+
Plasmid circularization
by ligation

Mutated
(D5C)
pWRE-9
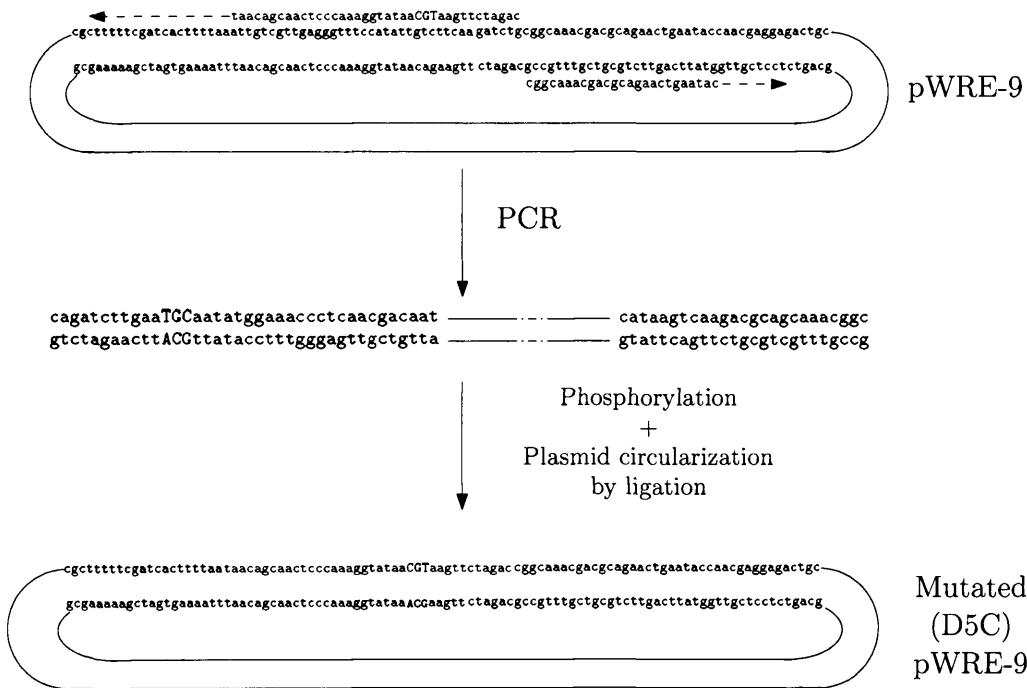
Figure 2.3: Flow chart of site-directed mutagenesis. The primers are designed to introduce the desired mutation (highlighted in capital letters) so that they anneal back to back to the plasmid. In the PCR reaction the Phusion^{TM} polymerase extends the primers and amplifies the plasmid with the mutation. In this particular example the DDJcytb001 (introducing the D5C mutation) and DDJcytb002 primers are used.

2.2   Materials

The materials used in this project and their sources are listed in Table 2.1.

Table 2.3: Chemical reagents materials with their suppliers.

Material	Supplier
100 bp and 1 kb DNA ladder	New England Biolabs, Hitchen, Hertfordshire, UK
Ascorbic acid	Sigma-Aldrich, Poole, Dorset, UK
Acrylamide / bis-Acrylamide (37.5:1)	Melford, Ipswich, Suffolk, UK
Agarose ultra pure	Sigma-Aldrich, Poole, Dorset, UK
Ammonium persulphate (APS)	Sigma-Aldrich, Poole, Dorset, UK
Ampicillin	Melford, Ipswich, Suffolk, UK
β-Mercaptoethanol	Sigma-Aldrich, Poole, Dorset, UK
bromophenol blue	Sigma-Aldrich, Poole, Dorset, UK
Copper(II) Protoporphyrin IX	Santa Cruz biotechnology, inc., US
Coomassie^{TM} brilliant blue	Sigma-Aldrich, Poole, Dorset, UK
Disodium phosphate (Na_2HPO_4)	Melford, Ipswich, Suffolk, UK
Dithiothreitol (DTT)	Melford, Ipswich, Suffolk, UK
dNTP	New England Biolabs, Hitchen, Hertfordshire, UK
Ethanol	Melford, Ipswich, Suffolk, UK
Ethidium bromide	Sigma-Aldrich, Poole, Dorset, UK
Ethylenediaminetetraacetic acid-disodium salt (EDTA)	Sigma-Aldrich, Poole, Dorset, UK
Glucose	Melford, Ipswich, Suffolk, UK
Glycerol	Sigma-Aldrich, Poole, Dorset, UK
Glycine	Melford, Ipswich, Suffolk, UK
Hemin	Sigma-Aldrich, Poole, Dorset, UK
Isopropyl-1-thio-β- D-galactopyranoside (IPTG)	Melford, Ipswich, Suffolk, UK
Isopropanol	Melford, Ipswich, Suffolk, UK
LB-Agar	Melford, Ipswich, Suffolk, UK
LB-Broth	Melford, Ipswich, Suffolk, UK
Magnesiumchloride	Melford, Ipswich, Suffolk, UK

Methanol	Melford, Ipswich, Suffolk, UK
Monosodium phosphate (NaH$_2$PO$_4$)	Melford, Ipswich, Suffolk, UK
Peptide marker (2512 Da-16949 Da)	GE Healthcare Hertfordshire, UK
Phenylmethylsulfonyl fluoride (PMSF)	Melford, Ipswich, Suffolk, UK
Phosphate buffered saline (PBS)	Melford, Ipswich, Suffolk, UK
Potassium chloride (KCl)	Melford, Ipswich, Suffolk, UK
Potassium hexacyanoferrate(III)	Sigma-Aldrich, Poole, Dorset, UK
Protein marker	New England Biolabs, Hitchen, Hertfordshire, UK
SDS ultra pure	Melford, Ipswich, Suffolk, UK
SOB media capsules	Melford, Ipswich, Suffolk, UK
Sodium chloride (NaCl)	Melford, Ipswich, Suffolk, UK
Sodium hydroxide (NaOH)	Melford, Ipswich, Suffolk, UK
Sucrose	Melford, Ipswich, Suffolk, UK
TEMED	Sigma-Aldrich, Poole, Dorset, UK
Tris(hydroxymethyl) aminomethane ultra pure (TRIS)	Melford, Ipswich, Suffolk, UK
Tyrosine	Melford, Ipswich, Suffolk, UK
YT media	Sigma-Aldrich, Poole, Dorset, UK
Zinc Protoporphyrin IX	Santa Cruz biotechnology, inc., US
Enzymes	
Gotaq®flexi DNA polymerase	Promega, Madison, WI, USA
Phusion®High fidelity DNA polymerase	New England Biolabs, Hitchen, Hertfordshire, UK
Quick T4 DNA ligase	New England Biolabs, Hitchen, Hertfordshire, UK
T4 Polynucleotide Kinase	New England Biolabs, Hitchen, Hertfordshire, UK
Kits	
Gel extraction kit	Qiagen, West Sussex, UK
MinElute Reaction Cleanup kit	Qiagen, West Sussex, UK
QIAGEN Plasmid Midi Kit	Qiagen, West Sussex, UK
QIAquick PCR Purification Kit	Qiagen, West Sussex, UK
Quick ligation kit	New England Biolabs, Hitchen, Hertfordshire, UK

2.2.1 Reagents and buffers

The buffers used in this project are listed in Table 2.4.

2.2.2 Media

All bacteria cell culture media and glassware were autoclaved at 121 °C for 20 minutes prior to use. Luria-Bertani (LB) broth, supplemented with 100 μg/ml ampicillin if required, was used for all the liquid bacteria cell cultures. LB agar plates supplemented with 100 μg/ml ampicillin when required were used for solid medium bacteria cultures. LB agar and broth were prepared by dissolving the appropriate component powders in distilled water according to manufacturer's protocol. SOC medium was prepared using SOB (Super Optimal Broth) media and 10 mM NaCl, 2.5 mM KCl, 10 mM $MgSO_4$, 10 mM $MgCl_2$ and 20 mM glucose.

2.2.3 Antibiotics

Ampicillin stock solution (100 mg/ml) was prepared in distilled water. After sterilisation by filtering through a 0.22 μm filter (Fisher scientific, Loughborough, Leicestershire, UK), the solution was stored at -20 °C in 1 ml aliquots.

2.2.4 DNA vector and oligonucleotide primers

The parent plasmid termed pWRE-9 that contains the wild-type gene encoding cyt b_{562} was used as template for introducing the required mutations (Figure 2.4). The cyt b_{562} gene was inserted into a pET-22b expression vector using *Nde*I and *Xho*I restriction sites. Expression of the gene is under the control of bacteriophage T7 promoter and can be induced by the use of sugar analogue Isopropyl-1-thio-β-D-galactopyranoside (IPTG). A signal sequence is also present that facilitates export of the protein to the periplasmic space of *E. coli*. The pET-22b plasmid contains the gene encoding β-lactamase which confers resistance to the antibiotic ampicillin.

The mutagenic synthetic oligonucleotides used to introduce the required mutations were designed by Dr. D. Dafydd Jones and have the sequence reported in Table 2.1. Table 2.2 shows the pET-F and pET-R sequences, designed to amplify DNA within the multiple cloning site of pET22-b vector.

2.2.5 Bacterial cell strain

Sub-cloning was performed with *E.coli* strain DH5α cells and protein expression was performed in *E.coli* strain BL21 (DE3) cells (Table 2.5).

Table 2.4: Composition of reagents and buffer.

Buffer	Composition
Buffer A	10 mM Sodium Phosphate pH 7, 50 mM NaCl
De-staining solution	20% (v/v) methanol, 10% (v/v) acetic acid in water
Phusion®polymerase buffer	10 μl 5 x Phusion®HF Buffer, 20 mM dNTPs, 2.5 μM primer A, 2.5 μM primer B, 29.5 μM H$_2$O, 1 μl pWRE9, 0.5 μl Phusion®hot start DNA polymerase
GoTaq®PCR buffer	2 μl 5x GoTaq®, 10 mM dNTPs, 0.5 μM pET-F , 0.5 μM pET-R, 1.25 mM MgCl$_2$ 0.25 μl H$_2$O, 0.25 μl GoTaq®DNA polymerase 5.0 μl of template DNA
TAE	40 mM Tris-acetate pH 9.5, 2 mM EDTA
Gel electrophoresis loading buffer	40% sucrose, 0.01% (w/v) bromophenol blue
Lysis buffer	10 mM Tris-HCl pH 8.0, 20% sucrose, 1 mM EDTA, 1mM PMSF, 1mM DTT, 100 μg/ml lysozyme)
Resolving gel for SDS-PAGE analysis	18% (w/v) Acrylamide/bis-Acrylamide, 0.375 mM Tris-HCl pH 8.8, 0.1% (w/v) SDS, 0.02% (w/v) TEMED, 0.05% (w/v) APS
SDS running buffer	28.8 g glycine, 8.0 g Tris Base in 2 L of distilled water, SDS added freshly to 0.1% (w/v)
SDS sample loading buffer	2% (w/v) SDS, 0.2M Tris-HCL pH 6.8, 0.04% (w/v) bromophenol blue, 8% (w/v) glycerol, β-mercaptoethanol added freshly to 10% (v/v).
Stacking gel for SDS-PAGE analysis	5% (w/v) Acrylamide/bis-Acrylamide, 0.65 mM Tris-HCl pH 6.8, 0.2% (w/v) SDS, 0.02% (w/v) TEMED, 0.1% (w/v) APS
Staining solution	50% (v/v) methanol, 10% (v/v) acetic acid in water, R250 coomassie blue (0.25g/l)
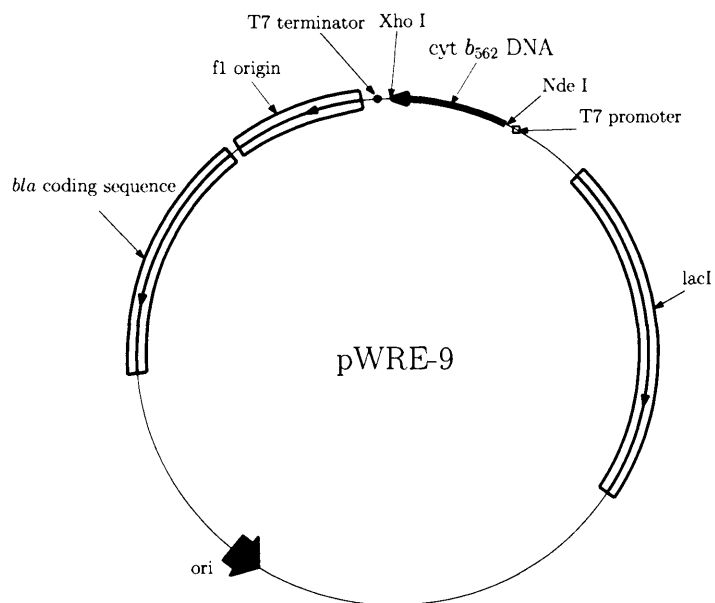
Figure 2.4: pWRE-9 plasmid circle map. Cyt b_{562} DNA (black thin arrow) was inserted in the *Nde*I and *Xho*I restriction sites of pET-22b plasmid. The arrow shows the orientation of cyt b_{562}.

Table 2.5: Genotype of *E.coli* strains DH5α and BL21 (DE3).

Strain	Genotype
DH5α	F⁻, *end*A1, glnV44, λthi-1, *rec*A1, *rel*A1, *gyr*A96, *deo*R, *nup*G, φ80d*lac*ZΔM15, Δ(*lac*ZYA-*arg*F)U169, hsdR17(r_K^- m_K^+), λ⁻
BL21 Gold (DE3)	F⁻, ompT, gal, dcm, lon, hsdS$_\beta$(r_β^- m_β^-), λ(DE3), pLysS(cm^R)

2.3 Molecular biology and recombinant DNA methods

2.3.1 DNA purification from bacteria cultures

A transformed bacteria colony was inoculated in 5 ml of LB-broth supplemented with ampicillin 100 μg/ml. After overnight growth (37 °C, 250 rpm), the cells were harvested by centrifugation (10 minutes at 4000 x g). DNA plasmids were purified from bacteria cells using the QIAfilter Plasmid Midi Kit and stored at -20 °C. 850 μl of the cells grown overnight in LB-broth were mixed with 150 μl of glycerol in aseptically conditions and stored at -80 °C.

2.3.2 Agarose gel electrophoresis

DNA analysis was performed using agarose gel electrophoresis. Agarose (1%-1.5% w/v) was dissolved in hot TAE buffer (Table 2.4). After cooling the solution, 0.5 μg/ml of ethidium bromide was added. To separate and visualise DNA samples, they were mixed with loading buffer (Table 2.4), fragmented by using electrophoresis in TAE buffer at 100 V for 30-45 minutes and visualized using an UV-transilluminator (GelDoc-It^{TM} Imaging System, UVP). Approximate molecular weight determination and quantification were carried out by comparing DNA bands with molecular size standards.

If required, DNA bands were excised from the agarose gel using a sharp scalpel and purified using QIAquick gel purification kit (Qiagen, West Sussex, UK).

2.3.3 Preparation of electro-competent *E.coli* cells

A method described by Sambrook et al. [105] and modified by Dr. W. Edwards was used for the preparation of electro-competent *E.coli* strains DH5α and BL-21 cells. A Beckman Coulter Avanti J-E centrifuge equipped with a JLA-16.250 rotor (J-life series rotor, Beckman, High Wycombe, Buckinghamshire, UK) was used for cells harvesting.

Cells from a glycerol stock were aseptically streaked onto a LB agar plate and incubated overnight at 37 °C. A single colony was used to inoculate 10 ml of LB-broth medium and the solution was grown overnight at 37 °C, 250 rpm. The starter culture was used to inoculate 2 x 500 ml of LB-broth medium in separate flasks and grown at 37 °C while shaking at 250 rpm until the cells reached an optical density measured at 600 nm (O.D.$_{600}$) of 0.6-0.8. The cultures were transferred to

pre-chilled centrifuge bottles (4 x 250 ml) and stored on wet ice for 15 minutes. The cells were then harvested by centrifugation (1500 x g for 20 minutes at 4 °C) and the supernatant carefully discarded. The bacterial cell pellet was resuspended in 1 l of ice-cold distilled water and centrifuged again (1500 x g for 20 minutes at 4 °C). To remove medium contamination from the bacteria cells the following steps were repeated three times: supernatant discarding, bacterial cell pellet resuspension in 0.5 l of ice-cold distilled water and centrifugation (1500 x g for 20 minutes at 4 °C). The cells were then resuspended in 100 ml of ice-cold 10% glycerol and harvested by centrifugation (1500 x g for 20 minutes at 4 °C). The supernatant was again discarded and the cells resuspended in 1 ml of ice-cold 10% glycerol. In order to ensure high transformation efficiency the cells were eventually diluted with ice-cold 10% glycerol to a concentration between 2-3 x 10^{10} cells/ml, frozen in liquid nitrogen in 40 μl aliquots and stored at -80 °C.

2.3.4   Transformation of *E.coli* cells using electroporation

Electroporation was used to transform *E.coli* with the required plasmids. Plasmid DNA (10 ng) was added to a 40 μl aliquot of relevant bacteria cells. After mixing, the solution was transferred to pre-chilled electroporation cuvettes. The bacteria cells/plasmid mixture was pulsed with 2.5 kV using a gene pulser (Bio-Rad, Hertordshire, UK) with a capacitance of 25 μF (capacitance extender by Bio-Rad) and a resistance of 200 Ω (pulse controller, Bio-Rad). A time constant of 4.5-4.6 ms was monitored for a successful pulse. 460 μl of room temperature SOC was quickly added and the solution was incubated at 37 °C for 1 hour. After incubation, 50 μl cells were aseptically plated on LB-agar (supplemented with ampicillin 100 μg/ml if required). The rest of the cells were harvested by centrifugation (4000 x g (Heraeus Biofuge Pico, DJB Labcare) for 120 s at room temperature), resuspended in 50 μl of SOC and aseptically plated on LB-agar. The colony plates were left overnight at 37 °C.

2.3.5   DNA amplification by PCR

DNA was amplified by PCR using GoTaq®flexi DNA polymerase in GoTaq®PCR buffer (Table 2.4). Amplification was performed using the parameters reported in Table 2.6.

Table 2.6: PCR cycling conditions using GoTaq®flexi DNA polymerase.

Cycle step	Temperature	Time	Number of cycles
Initial denaturation	95 °C	120 s	1
Denaturation	95 °C	60 s	
Annealing	52 °C	30 s	30
Extension	72 °C	180 s	
Final extension	72 °C	600 s	1
Holding	10 °C		

Table 2.7: PCR cycling conditions using Phusion®DNA polymerase.

Cycle step	Temperature	Time	Number of cycles
Initial denaturation	98 °C	60 s	1
Denaturation	98 °C	10 s	
Annealing	70 °C	30 s	30
Extension	72 °C	180 s	
Final extension	72 °C	600 s	1
Holding	10 °C		

2.3.6 DNA amplification by I-PCR

The I-PCR reactions were performed in Phusion®polymerase buffer (Table 2.4) with an amount of plasmid template titrated as down as possible (1-10 μM) to avoid background transformants after ligation and transformation. Amplification was performed using the parameters reported in Table 2.7.

2.3.7 DNA sequencing

The determination of DNA nucleotide sequences was carried out at the DNA sequencing core of the molecular biology unit at Cardiff University using an ABI Prism 3100 16 capillary genetic analyser with Big dye terminator version 3.1 cycle sequencing kit (ABI, Foster City, California, USA) and pellet paint (Novogen Ltd, Windsor, Berkhire, UK) for DNA coprecipitation.

2.3.8 DNA phosphorylation and ligation

DNA phosphorylation and ligation were carried out using T4 Polynucleotide Kinase and Quick T4 DNA ligase in Quick ligation reaction buffer (Table 3.1) according to manufacturer instructions. Vector DNA (50 ng) was mixed with 1 μl of T4 Polynucleotide Kinase (10 units), 10 μl of Quick ligation reaction buffer and the volume was adjusted to 20 μl with H_2O. Then the solution was centrifuged briefly and incubated at 37 °C for 30 minutes. Subsequently 1 μl of Quick T4 DNA ligase

(400 units) was added to the solution that, after brief centrifugation, was incubated at room temperature (25 °C) for 30 minutes. Control ligations without the ligase enzyme were also carried out, in order to determine the background level from the original plasmid.

The enzymes were removed from the plasmid DNA solution using MinElute reaction clean up kit.

2.4 Protein expression and analysis methods

2.4.1 Recombinant protein expression

The wild-type and the cysteine mutants cyt b_{562} were expressed in *E.coli* BL-21 (DE3) cells. These cells contain the T7 RNA polymerase under the control of the *lacUV*5 operon promoter, and expression can be induced by the addition of IPTG. A single colony from a freshly streaked plate was inoculated in 2 x 5 ml LB-Broth medium supplemented with 100 μg/ml ampicillin and cells were incubated with shaking (250 rpm) at 37 °C overnight. The overnight cell cultures were then used to inoculate 2 x 500 ml LB-Broth medium supplemented with 100 μg/ml ampicillin and grown at 37 °C in shaking flasks (250 rpm). Upon reaching an $OD_{600} = 0.6$-1.0, protein expression was induced by adding 1 mM IPTG. Growth was continued for 3 hours at 37 °C while shaking (250 rpm). Small aliquots (1 ml) were taken at interval of 1 hour and induction analysed by using SDS-PAGE analysis.

Cells were harvested by centrifugation at 2400 x g for 20 minutes at 4 °C. The reddish pellet was resuspended in cold 10 mM Tris-HCl pH 8.0, centrifuged at 2400 x g for 20 minutes at 4 °C, then resuspended again in cold lysis buffer (Table 2.4) and left on ice for 30 minutes. After centrifugation (15000 x g for 10 minutes at 4 °C) the supernatant contained the cells periplasmic fraction.

2.4.2 Protein purification

Standard techniques to purify the cyt b_{562} [15, 49] and its mutants were optimized. The apo- and holo-protein were purified and separated on a Q-Sepharose (GE health-care) ion exchange column developed with a linear gradient of 0-500 mM NaCl. Fractions containing apo- and holo-protein were concentrated separately through ammonium sulphate precipitation. The salt was added to the cytochrome solution to a final concentration of 90% saturation while stirring at 4 °C. The solution was left stirring overnight at 4 °C to ensure a proper mixing; it was then centrifuged for 30 minutes at 10000 x g, the supernatant discarded and the pellet resuspended in 2 ml

of buffer A (Table 2.4). The protein solution was further purified on a Superdex^{TM} 75 pg Hiload^{TM} 16/60 (GE healthcare) gel filtration column equilibrated in buffer A. The purity of the resulting samples was verified through SDS-PAGE analysis. To reduce the thiol groups and prevent oligomer formation 1 mM dithiothreitol (DTT) was used in all the mutant purification steps. The protein solutions were either used immediately or stored at -80 °C.

2.4.3 Sodium dodecyl sulphate polyacrylamide gel electrophoresis (SDS-PAGE)

SDS-PAGE analysis was performed using a mini-PROTEAN 3 electrophoresis system (Bio-RAD, Hertfordshire, UK). Resolving and stacking gels were made as shown in Table 2.4. Table 2.4 describes also sample and electrolyte buffers, staining and de-staining solutions. Gels were usually stained using coomassie blue for at least 1 hour, destained overnight and visualized.

2.4.4 Ultraviolet-visible spectroscopy and hemin spectrophotometric titration

Optical absorbance spectra were recorded at room temperature on a Hewlett--Packard 8452A ChemStation diode array spectrophotometer. All the experiments were recorded at room temperature in quartz cuvettes of 1 cm path length. The protein concentration was spectroscopically determined using an extinction coefficient at 280 nm (ε_{280}) of 2.98 mM^{-1}cm^{-1} for the apo-cyt b_{562}, an extinction coefficient at 428 nm (ε_{428}) of 180.1 mM^{-1}cm^{-1} for the reduced holo-cyt b_{562}, and an extinction coefficient at 418 nm (ε_{418}) of 117.4 mM^{-1}cm^{-1} for the oxidised holo-cyt b_{562} [78]. Protein samples were reduced by addition of fresh ascorbic acid and oxidised by addition of fresh potassium hexacyanoferrate(III) (potassium ferricyanide) both dissolved in deionized water.

Hemin, Cu-PP and Zn-PP spectrophotometric titration experiments were executed with the molecules freshly dissolved in 100 μl of 1 M NaOH and 900 μl of deionized water. The protoporphyrin concentration was quantified using an extinction coefficient of 58.4 mM^{-1} cm^{-1} at 385 nm for hemin [11], 210 mM^{-1} cm^{-1} at 386 nm for Cu-PP [4] and 161 mM^{-1} cm^{-1} at 398 nm for Zn-PP [82]. To avoid molecular aggregation and photodegradation, the oxidizing, reducing and protoporphyrin solutions were stored in dark, kept at 4 °C and the solutions were centrifuged prior experiments. For stoichiometric titration experiments two solutions were prepared. The first one (solution *A*) contained 20 μM apo-protein and 20 μM of oxidizing or

reducing agent in 10 mM phosphate buffer pH 6.2. The second one was made of 20 μM protoporphyrin, 10 μM oxidizing or reducing agent in 10 mM phosphate buffer (solution *B*). The experiments were performed by recording the spectrum of solution *A* in a quartz cuvette, then adding increasing aliquots of solution *B*. After each addition, the solution was left to equilibrate for 2 minutes, then the spectrum recorded. These steps were repeated for solutions containing increasing protoporphyrin concentration (from 0 μM to $\sim$ 30 μM). To determine the dissociation constant for the cyt b_{562}-protoporphyrin complex, titration curves were generated by measuring the Soret absorbance band as a function of increasing volumes of protoporphyrin stock solution. The holo-proteins absorbance at 418 nm, 428 nm, 414 nm and 430 nm was monitored for the oxidised hemin, reduced hemin, Cu-PP and Zn-PP titration, respectively. Considering a simple thermodynamic equilibrium between a protein and its ligand [127], the experimental data could be fitted to the equation:

$$\Delta F = \frac{C}{2}\left([P]_t + [L]_t + K_d\right) - \frac{C}{2}\sqrt{\left(([P]_t + [L]_t + K_d)\right)^2 - 4\,[P]_t\,[L]_t} \quad (2.1)$$

where C is a a measure of the absorption coefficient, $[P]_t$ and $[L]_t$ are the protein and protoporphyrin total concentrations and K_d is the dissociation constant. The total concentration of protein and its ligand can be then obtained considering the initial volume ($[V]_0$) and concentration ($[P]_0$) of the protein solution, the concentration of the protoporphyrin solution ($[L]_0$) and the total volume of the ligand ($[V]_L$) added during the experiment:

$$[P]_t = \frac{[P]_0\,[V]_0}{[V]_0 + [V]_L}, \quad [L]_t = \frac{[L]_0\,[V]_L}{[V]_0 + [V]_L} \quad (2.2)$$

All the experimental data were processed by using OriginPro 8.

2.5 Results and discussion

2.5.1 Site-directed mutagenesis

The pWRE9 plasmid, containing the cyt b_{562} gene, was manipulated using site-directed mutagenesis to create single and double cysteine variants of the cyt b_{562}.

The agarose gel electrophoresis analysis (Figure 2.5) of the I-PCR for the amplification of the two mutated pWRE9 plasmids showed products of the expected molecular size ($\sim$ 6000 bp).

The mutated plasmids were transformed into *E.coli* DH5α and grown overnight
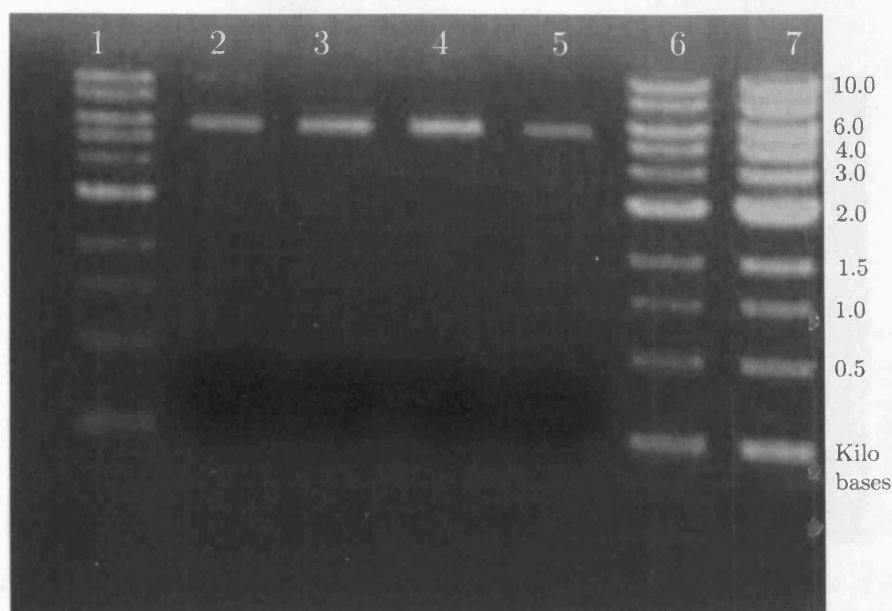
Figure 2.5: Agarose gel electrophoresis analysis of the I-PCR products with pWRE9 plasmid as template visualized by UV-transilluminator. Lane 1, 1 Kb marker (0.125 µg); lane 2, D5C mutant; lane 3, SH-SA mutant; lane 4, D50C mutant; lane 5, SH-LA mutant; lane 6, 1 Kb marker (0.25 µg); lane 7, 1 Kb marker (0.5 µg).

at 37 °C. Some colonies were screened by PCR for the presence of the ligated DNA using the primers pET-F and pET-R and Gotaq®DNA polymerase. The agarose gel electrophoresis analysis (Figure 2.6) of these PCR experiments showed products of the expected molecular size ($\sim$ 600 bp). Correct nucleotide sequences of the two double mutants were proved by DNA sequencing.

2.5.2 Protein expression and purification

Plasmids containing both wild-type and single and double cysteine mutants cyt b_{562} genes were used to individually transform *E.coli* cells. After cell grown to a concentration of 8-10 x 10^6 cells/ml (corresponding to an O.D.$_{600}$ of 0.6-0.8), protein overexpression was successfully achieved by the addition of 1 mM IPTG to the cells cultures. SDS-PAGE analysis (Figure 2.7, 2.8) of cell aliquots showed that proteins of approximately 12 kDa size (corresponding to the cyt b_{562} size) were produced after IPTG induction. The cells were harvested and a combination of two protocols based on osmotic shock (20 % sucrose) and lysozyme was used to isolate the proteins. After removal of insoluble cell debris by centrifugation, SDS-PAGE analysis of the resulting supernatant (Figure 2.7, 2.8) revealed that a large fraction of the overexpressed proteins was present in the supernatant. It was consequently deduced that both the wild-type and the cysteine mutants cyt b_{562} are soluble.
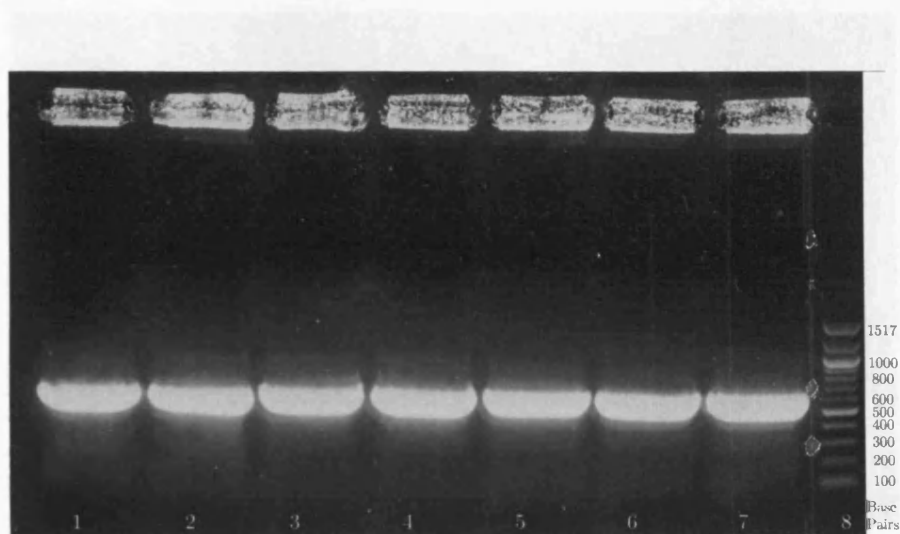
Figure 2.6: Agarose gel electrophoresis analysis of colony PCR products for each of the cyt b_{562} cysteine mutants visualized by UV-transilluminator. Lane 1, pWRE9 plasmid; lane 2, D5C mutant pWRE9 plasmid; lane 3, K104C mutant pWRE9 plasmid; lane 4, SH-SA mutant pWRE9 plasmid; lane 5, D21C mutant pWRE9 plasmid; lane 6, D50C mutant pWRE9 plasmid; lane 7, SH-LA mutant pWRE9 plasmid; lane 8, 100 bp marker (0.5 μg).
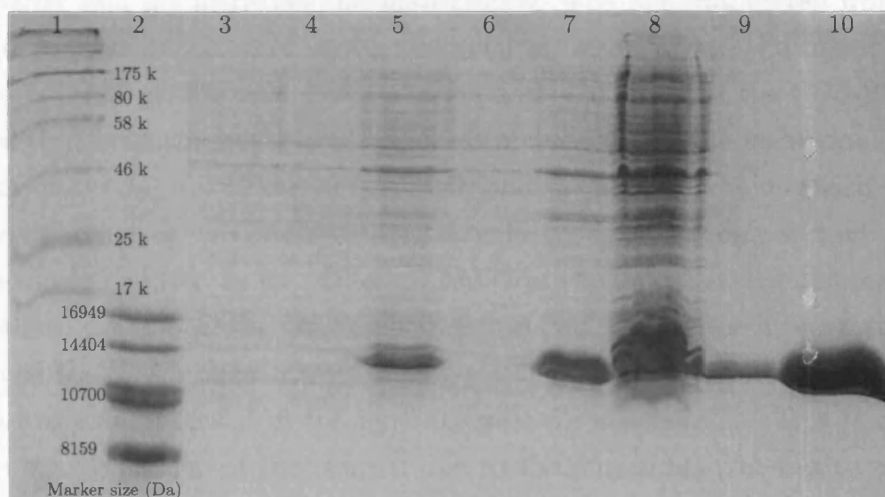
Figure 2.7: SDS/PAGE analysis of the expression and purification procedures for the SH-SA cyt b_{562}. Lane 1, protein marker; lane 2, peptide marker; lane 3, lysed cells transformed with pWRE9 before IPTG induction; lane 4, lysed cells uninduced transformed with pET22-b; lane 5, lysed cells transformed with pWRE9 after 3 hours of IPTG induction; lane 6, lysed cells transformed with pET22-b after 3 hours of IPTG induction (control); lane 7, supernatant following lysis and centrifugation; lane 8, insoluble fraction following lysis and centrifugation; lane 9, elution fraction at 120 mM NaCl fraction from the Q-Sepharose column; lane 10, fraction from the gel filtration column.
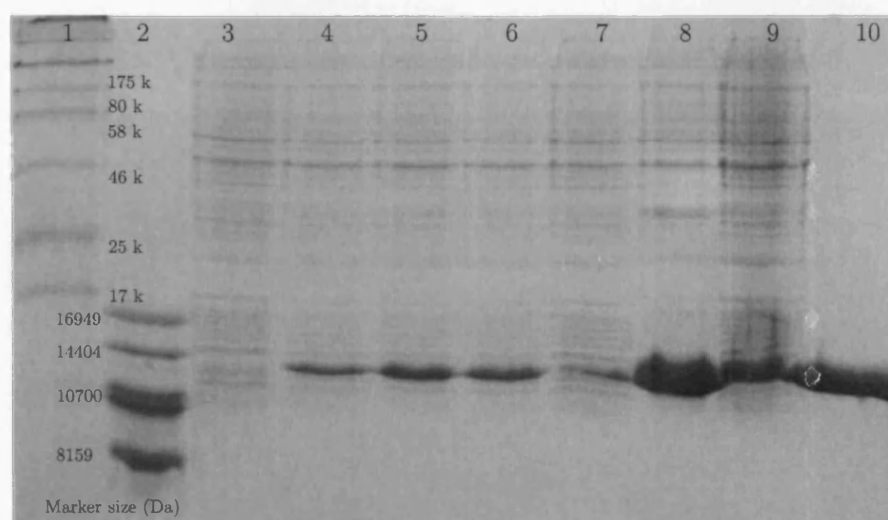
Figure 2.8: SDS/PAGE analysis of the expression and purification procedures for the SH-LA cyt b_{562}. Lane 1, protein marker; lane 2, peptide marker; lane 3, lysed cells before IPTG induction; lane 4, lysed cells after 1 hour of IPTG induction; lane 5, lysed cells after 2 hours of IPTG induction; lane 6, lysed cells after 3 hours of IPTG induction; lane 7, lysed cells uninduced; lane 8, supernatant following lysis and centrifugation; lane 9, insoluble fraction following lysis and centrifugation; lane 10, fraction from the gel filtration column.

The wild-type and cysteine variants cyt b_{562} were successfully purified using ion exchange and gel filtration chromatography. The material eluted from the ion exchange column at 120 mM NaCl absorbed at 280 nm and the material eluted from the column at 200 mM NaCl absorbed at 420 nm. As the SDS-PAGE gels indicated that both the materials had an estimated molecular weight similar to that expected for cyt b_{562} ($\sim$ 12kDa, Figure 2.9) and the apo- and holo-cytochrome have a charge difference, it was inferred that the wild-type and cysteine variants apo- and holo-cytochrome eluted as two different peaks in the ion exchange chromatograms. In particular, the apo-protein eluted at 120 mM NaCl, while the holo-protein eluted at 200 mM NaCl. An elution shift among the SH-LA, D50C, wild-type and SH-SA proteins was also observed in the ion exchange chromatograms. This is consistent with the charge change of the protein due to the mutations (the evaluated pI are: SH-LA = 6.15, D50C = 5.69, wild-type = 5.38, SH-SA = 5.36).

The separated apo- and holo-proteins solutions were concentrated by ammonium sulphate precipitation. SDS-PAGE gel analysis of the solutions obtained from the ammonium sulphate concentration (Figure 2.10), show that a small amount of contamination remains in the sample at molecular sizes corresponding approximatively to 30 kDa and 70 kDa. The origin of these bands is unknown.

The concentrated protein solutions ($\sim$ 5 ml) were finally applied to a gel filtration column. After this purification step all the different proteins were present as a single
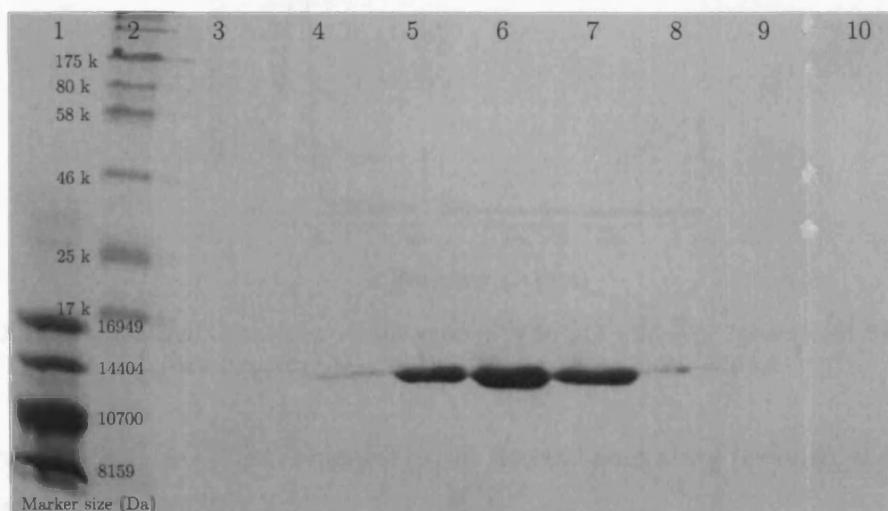
Figure 2.9: SDS/PAGE analysis of the different elution fractions from the Q-Sepharose column of the periplasmic extracts of the wild-type cyt b_{562} culture. Lane 1, peptide marker; lane 2, protein marker; lane 3, elution fraction at 80 mM NaCl; lane 4, 100 mM NaCl; lane 5, 110 mM NaCl; lane 6, 120 mM NaCl; lane 7, 130 mM NaCl; lane 8, 140 mM NaCl; lane 9, 160 mM NaCl; lane 10, 180 mM NaCl.
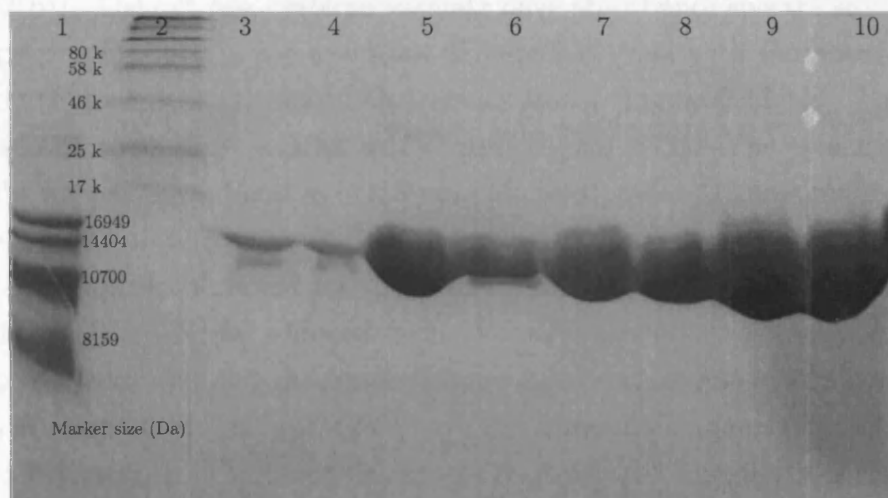
Figure 2.10: SDS/PAGE analysis of the apo- and holo-proteins from the ammonium sulphate precipitation. Lane 1, peptide marker; lane 2, protein marker; lane 5, apo-cyt b_{562} wild-type; lane 6, apo-cyt b_{562} SH-SA; lane 7, apo-cyt b_{562} SH-LA mutant; lane 8, holo-cyt b_{562} wild-type; lane 9, holo-cyt b_{562} SH-SA; lane 10 holo-cyt b_{562} SH-LA.
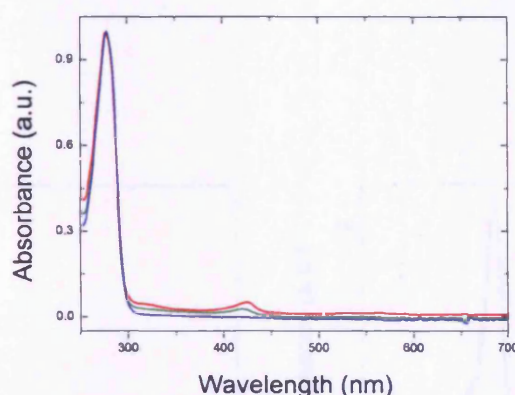
Figure 2.11: Normalized ultraviolet-visible spectra of 20 μM wild-type (green), SH-SA (red) and SH-LA (blue) apo-cyt b_{562} in 10 mM phosphate buffer pH 6.2.

band on the SDS PAGE gel indicating that no contaminating proteins were present in the sample (Figure 2.7, 2.8).

2.5.3   Ultraviolet-visible spectroscopy and hemin spectrophotometric titration

To examine if the introduced cysteine residues changed the cyt b_{562} structure and its affinity for haem, the wild-type and the mutants cyt b_{562} were spectroscopically characterised. The absorption properties of the apo- and holo-wild-type cyt b_{562} are in agreement with previous results by Itagaki et al. [49, 76] (Figures 2.11, 2.12(a) and 2.12(b)). The cyt b_{562} cysteine variants have absorbance spectra similar to the wild-type protein both in the apo-form (Figure 2.11) and with the haem bound in the ferric (Figure 2.12(a)) and in the ferrous states (Figure 2.12(b)). The spectra of the apo-proteins show a peak at 278 nm (Figure 2.11). The cysteine variants retain the intense Soret band at $\sim$418 nm (oxidised) and $\sim$427 nm (reduced) in the holo-protein form. Furthermore, like the wild-type protein, the broad absorbance peak at 530-540 nm observed for the oxidised form converts to two distinct peaks at 530 and 560 nm in the reduced form. Preservation of the holo-protein spectra between the wild-type and the single (Figure 2.13) and double cysteine variants of cyt b_{562} confirms that the mutations have not altered the manner by which haem binds to the protein. The result is especially important for the SH-SA variant as the introduced thiol groups (that have the potential to coordinate the metal centre) lie close to the residues that normally bind the iron center of haem.

Figure 2.14 shows the UV-visible spectra of Zn-PP, Cu-PP, and wild-type cyt b_{562} and D50C single cysteine mutant reconstructed with the zinc and copper protoporphyrins in 10 mM phosphate buffer. Upon complex formation (Zn-PP/apo-cyt

(a)   (b)
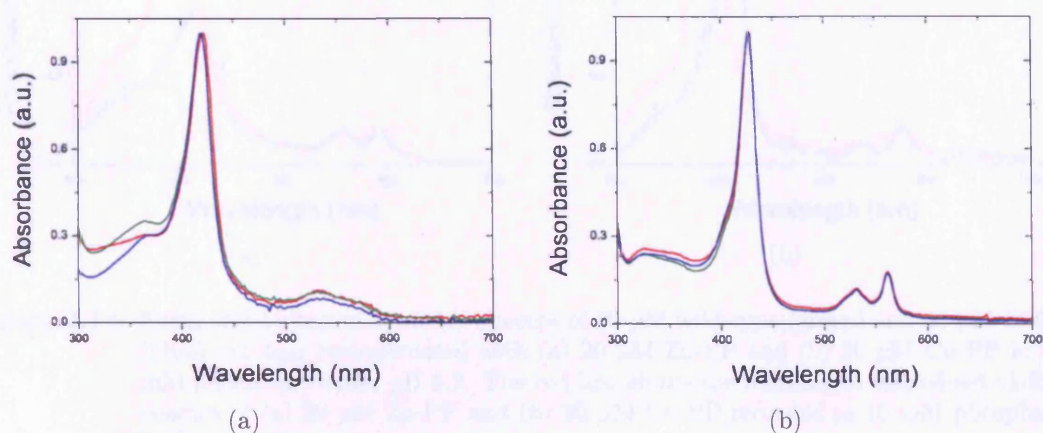
Figure 2.12: Normalized ultraviolet visible spectra of 20 μM (a) oxidized and (b) reduced wild-type (green), SH-SA (red) and SH-LA (blue) holo-cyt b_{562} in 10 mM phosphate buffer pH 6.2.

(a)   (b)
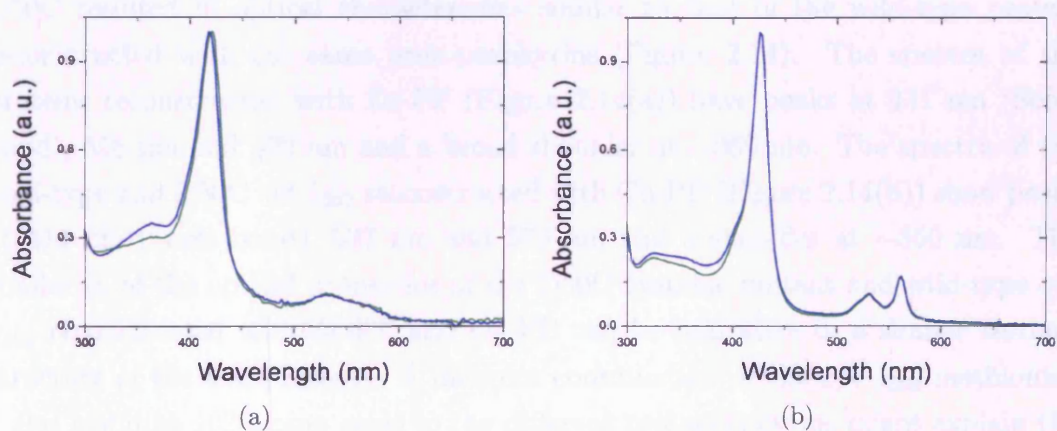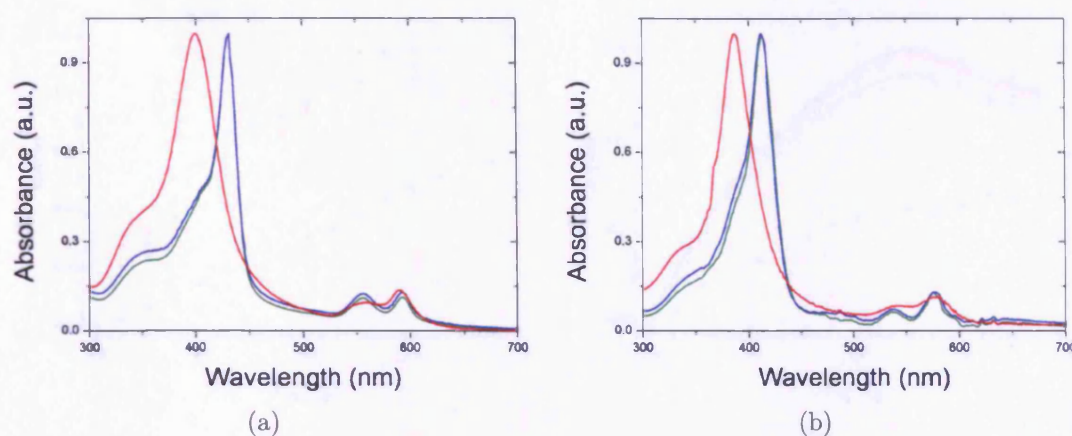
Figure 2.13: Normalized ultraviolet visible spectra of 20 μM (a) oxidised and (b) reduced wild-type (green) and D50C (blue) holo-cyt b_{562} in 10 mM phosphate buffer pH 6.2.

(a)   (b)

Figure 2.14: Normalized ultraviolet visible spectra of 20 μM wild-type (green) and 20 μM D50C (blue) cyt b_{562} reconstructed with (a) 20 μM Zn-PP and (b) 20 μM Cu-PP in 10 mM phosphate buffer pH 6.2. The red line shows the normalized ultraviolet visible spectra of (a) 20 μM Zn-PP and (b) 20 μM Cu-PP recorded in 10 mM phosphate buffer pH 6.2.

b_{562} and Cu-PP/apo-cyt b_{562}) a red shift occurs in the Soret band along with minor changes in the position of the smaller peaks at ~550 nm and ~600 nm. The shifts in the Soret bands recorded for both Zn-PP cyt b_{562} and Cu-PP cyt b_{562} are very similar to those reported for myoglobin [4, 57] or cytochrome c [52] and could indicate that the metal center (Cu or Zn) changes its coordination sphere and the metalloporphyins are specifically coordinated to the polypeptide chain as the haem in the native proteins.

Addition of Zn-PP and Cu-PP to the apo-form of the single cysteine variant D50C resulted in optical characteristics similar to that of the wild-type protein reconstructed with the same protoporphyrins (Figure 2.14). The spectra of the proteins reconstructed with Zn-PP (Figure 2.14(a)) have peaks at 431 nm (Soret band), 558 nm and 592 nm and a broad shoulder at ~360 nm. The spectra of the wild-type and D50C cyt b_{562} reconstructed with Cu-PP (Figure 2.14(b)) show peaks at 414 nm (Soret band), 537 nm and 579 nm and a shoulder at ~350 nm. The similarity of the optical properties of the D50C cysteine mutant and wild-type cyt b_{562} reconstructed with Zn-PP and Cu-PP can be indicative of a similar tertiary structure of the two proteins. A different coordination of the cyt b_{562} methionine 7 and histidine 102 amino acids to the different protoporphyrins might explain the shift in the Soret band observed for the haem-cyt b_{562}, the Zn-PP cyt b_{562} and the Cu-PP cyt b_{562}.

To investigate if the mutations altered the affinity of oxidised haem for the protein, a spectroscopic approach was taken to monitor haem binding on titration into protein (Figure 2.15(a) and (b)). Reduced haem binds with a very high affinity

(a)   (b)
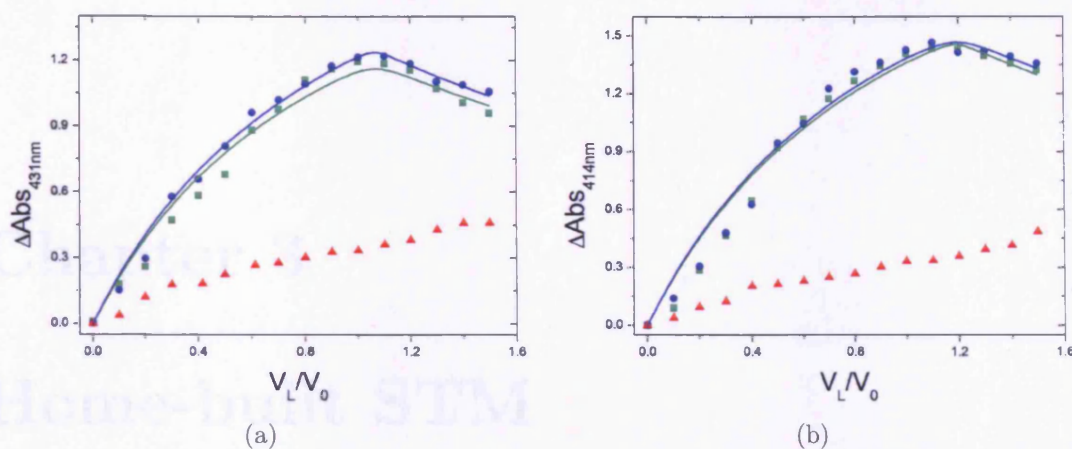
Figure 2.16: Spectrophotometric titration of wild-type (green), D50C (blue) apo-cyt b_{562} with (a) Zn-PP and (b) Cu-PP. The titration experiments were performed using 20 μM of apo-cyt b_{562} in 1 ml of 10 mM phosphate buffer pH 6.2 (V_0) with increasing aliquots of a 20 μM porphyrin solution (V_L) (only the solution containing the porphyrin was used for the blank experiments, data showed in red). The solid curves are the best fit of the experimental data according to 2.2. Error bars are not shown to improve the clarity of the figure.

On the other hand, a small excess of metalloporphyrins was necessary to complete the formation of the Cu-PP-protein complex (Figure 2.16(b)) suggesting a less tight coordination of the copper axial ligands to the polypeptide chain. The K_d values for apo-cyt b_{562} found from the best fit of the experimental data to equation (2.2) were 500 $\pm$ 80 nM and 100 $\pm$ 30 nM for Zn-PP and Cu-PP, respectively. They are at least one order of magnitude higher than the K_d values calculated for the haem-apo-cyt b_{562} complex, indicating that the cytochrome affinity for Cu-PP and Zn-PP is lower than for hemin perhaps related to a different coordination geometry of the metal centres to the protein.

2.6 Conclusions

In this chapter the introduction of cysteine residues by site-directed mutagenesis on opposite ends/faces of the cyt b_{562}, along its long and short axes respectively was described (Figure 1.1). Analysis of the UV-visible absorption spectra and hemin spectrophotometric titration showed that the introduced cysteine mutations do not affect the protein's tertiary structure and its haem binding properties. Wild-type and D50C apo-cyt b_{562} were reconstructed with Zn-PP and Cu-PP. The absorption characteristics of the porphyrin-protein complex indicated a good coordination of the zinc and copper axial ligands to the polypetide chain.

Chapter 3

Home-built STM

The scanning tunnelling microscope (STM) was invented in the beginning of 1982 by Binnig and Rohrer at the IBM Research Laboratory in Rüschlikon, Switzerland [19]. Its importance in explaining the theories of electron transport was soon recognized and the two inventors were awarded the 1986 Noble Prize in Physics. In this chapter I first describe the basic theory of tunnelling and the principle of operation of the STM. In the second part of the chapter I describe the mechanical setup and electronics of a low-drift STM that I constructed and show HOPG and Au(111) STM images I acquired for the system calibration.

3.1   Theory of tunnelling and STM operating principles

According to classical physics, two conductive electrodes separated by an insulator form an impenetrable barrier for electrons. However, if the barrier is very thin (~1 nm), electrons can tunnel through it and the transmission probability of this event can be described by the Schrödinger's equation [63]. In an STM setup a sharp metallic probe (tip) is brought in close proximity (0.5-2.0 nm) to a conductive surface (substrate). At such a small distance electrons can tunnel the barrier existing between the two electrodes due to overlap of the electron wave functions of the tip and substrate. Assuming that the tip and the substrate are ideal conductors, the probability Ψ of an electron transmission across a square potential barrier is given by the solution of the Schrödinger's equation in 1-D [63]:

$$\Psi \propto e^{-\kappa z} \tag{3.1}$$
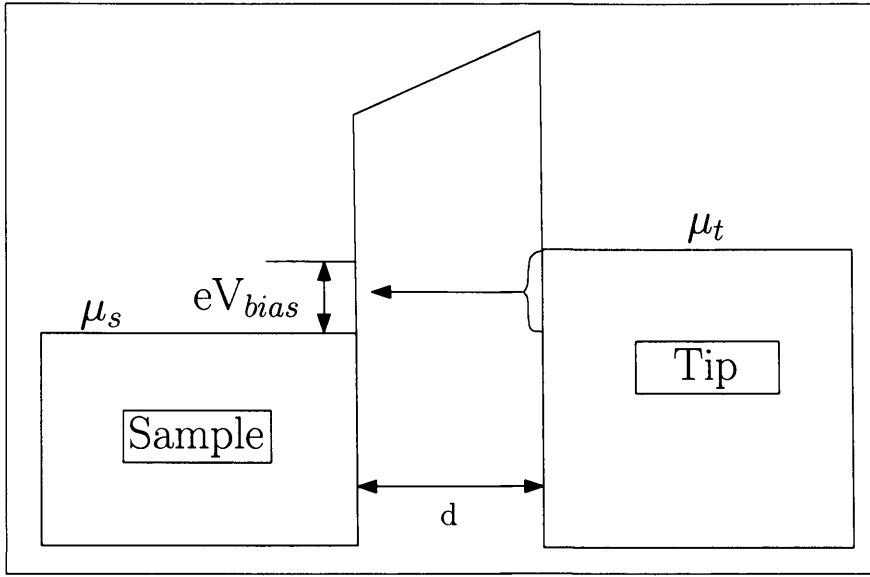
Figure 3.1: Schematic diagram of the energy diagram for quantum tunnelling between two metal-lic electrodes (sample and tip) placed at a distance d. μ_s and μ_t are the Fermi energy of the sample and the tip, respectively. When the two electrodes are few Å apart and a bias voltage V_b is applied to one electrode in respect to the other, electrons can tunnel the barrier.

where the wave number κ is related to the energy of the electron and z is the length of the barrier. If a voltage V_b is applied to the tunnelling junction, electrons with energy between the Fermi energies of the substrate and the tip are free to tunnel into the conduction band of the positive electrode (3.1). At small applied voltages, the tunnelling current is proportional to:

$$I \propto C_1 V_b \sqrt{\phi} e^{-C_2 z \sqrt{\phi}} \tag{3.2}$$

where $C_1 = 4.74$ μA V^{-1} eV$^{-1/2}$, $C_2 = 1.025$ Å^{-1} eV$^{-1/2}$ and ϕ is the work function [110, 122]. The exponential dependence of the tunnelling current with distance gives the STM a high vertical resolution (0.1 Å). In fact, considering that most metals have a work function of ~ 5 eV, for a change in tip-substrate separation of 1 Å, the current changes by an order of magnitude ($\propto e^{C_2 \sqrt{\phi}}$).

As other types of scanning probe microscope (SPM), the STM tip scans the sample surface while maintaining a constant set-point value. In STM the tunnelling current is measured as function of the tip-sample position that is controlled by using piezoelectric elements and a feedback loop. When operating in constant current mode, the input signal of the STM feedback loop is the measured tunnelling current that is compared with a preset value (current set-point). The controller applies a voltage to the piezoelectric element in order to reduce or increase the distance between the tip and the sample depending on whether the measured current is

smaller or larger than the current set-point.

Since its invention, the STM technique has evolved and it is now a method of choice for the characterization of samples at the nanometric scale. STM has been used to analyze a variety of materials both conductive and semi-conductive in different environments such as ultra-high vacuum, inert atmosphere (N2, Ar), air or liquid [128]. Many dynamic processes have been investigated and biomolecules such as DNA and proteins have been studied in their natural environment by operating STM in liquid. Further improvement to the technique has been achieved thanks to the introduction of the substrate potentiostatic control in electrochemical solution. The possibility to independently control the bias voltage and the surface electrode has allowed new experiments in which classical electrochemical studies are performed simultaneously to single molecule STM imaging [107].

Thanks to the dependence of the tunnelling current on the electronic properties of the sample and to the high lateral resolution of STM, much more information than the simple morphology of the studied surface can be obtained. As an example, the density of states or the conductivity of single atoms or molecules have been studied by using the I-V scanning tunnelling spectroscopy (STS) technique [120]. This field has been deeply investigated and I-V characteristics have been acquired in a variety of modes [128]. In simple I-V measurements, after an image is recorded, the tip is positioned at a location of interest, the feedback loop turned off and the voltage scanned while the tunnelling current is recorded. Another method of performing I-V experiments is Current Imaging Tunnelling Spectroscopy (CITS). In this mode an image is recorded at a preset voltage and at the same time I-V characteristics are measured at every pixel of the image. In this way a 4-D map of I-V data as function of position is obtained. The I-V plots obtained in both methods can be analysed according to various models and can provide detailed information about the electronic features of the sample (band gap, conductivity, DOS). However, measurements of a statistically significant number of I-V spectra and their correlation with morphological features of the sample can suffer some limitations due to the STM lateral and vertical thermal drift. Change in the tip-sample distance and/or in their relative position can lead to misinterpretation of the data [62]. Reduction of the drift can be achieved by an appropriate choice of the mechanical units of the device or by using active compensation [83]. I decided to design and build a home-built STM with piezoelectric tubes having a coaxial geometry in order to minimize the STM system thermal drift and the problems related to it during I-V experiments.

(a)   (b)
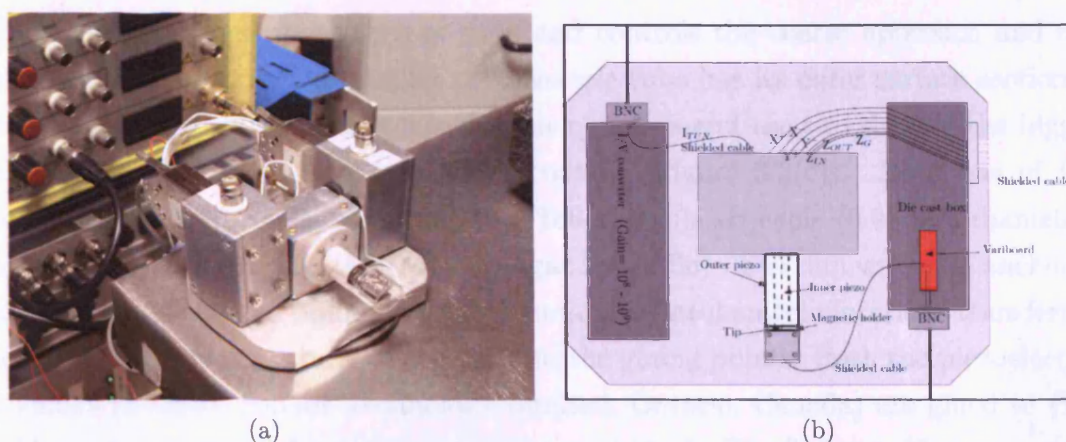
Figure 3.2: (a) Picture and (b) schematic design of the STM head and the current to voltage converter placed on a stainless steel block. Part of the cables and the STM control electronics can be observed in (a).

3.2 Home-built STM: design

Figure 3.2 shows a picture and a schematic diagram of the home-built STM. Its basic components include a sharp metallic tip, two piezoelectric scanning tubes that control the relative lateral and vertical movement of the tip in respect to the sample, a glass tube housing the sample holder, a vibration isolation stage and the electronics that drives the coarse approach, controls the voltage applied to the piezoelectric elements and measures the tunnelling current. Because of its small dimension and rigidity, the system has a high resonance frequency and can be operated in a small chamber to control the operating humidity and temperature conditions.

3.2.1 STM head

The home-built STM follows a design reported by Jayadevaiah [77]. The STM scan unit head (Figure 3.3(a) and (b)) consists of (1) a sample holder made of two stainless steel half cylinders with (2) 8 ball bearings (1 mm diameter) held together by (3) a stainless steel spring whose elastic constant can be controlled by screwing in or unscrewing (4) a stainless steel screw. (5) a magnet (5 mm diameter) glued to the sample holder holds the sample stage allowing a coarse lateral adjustment of the scanned area. The sample holder moves horizontally inside (6) a pyrex tube of 13.5 mm diameter and 31 mm length. (7) the tip holder (a stainless steel syringe needle) is glued to the inner wall of (8) a piezoelectric tube (length = 17.0 ± 0.1 mm, outer diameter = 7.0 ± 0.1 mm, inner diameter = 5.0 ± 0.1 mm) that controls the lateral movement of the tip. (9) a larger piezoelectric tube (length = 17.0 ± 0.1 mm; outer diameter = 13.0 ± 0.1 mm, inner diameter = 11.0

± 0.1 mm) is glued to the pyrex tube and controls the coarse approach and the z-scanning direction. The smaller piezoelectric tube has its outer surface sectioned into 4 metallized quadrants, while the inner surface and the two sides of the bigger piezo tube have a uniform metallized coating (Figure 3.3(c)). Each one of the equipotential surfaces is connected to a Teflon insulated cable (0.25 mm diameter) by using Acheson Silver DAG 1415M (Agar Scientific). The thin wires are anchored to the scanners at two points in order to minimize mechanical vibrations transferred to the STM head and the stress applied to the gluing points. Both the piezoelectric scanners (BM500, Sensor Technology Limited, Ontario, Canada) are glued to (10) a Macor insert screwed to (11) a stainless steel block. The Teflon cables are routed to pin connectors housed near the current to voltage amplifier and into a shielded box through small holes in the block (Figure 3.2(b)). Flexible coaxial cables, more robust and easy to handle, are used to connect the microscope head to the control electronics. By using pin connectors the wires can be easily changed and their accidental pulling away from the scanners is avoided by their mechanical clamping. When required, cyano acrylate glue was used to attach together the STM parts. The overall dimensions of the STM head are about 50 mm x 30 mm x 25 mm.

The substrate holder is usually manually placed within ~1 mm from the tip and a "stick-slip" mechanism is employed to bring the sample within few angstroms from the tip [102]. To move the sample holder towards the tip, a sharp high voltage sawtooth waveform is applied to the bigger piezoelectric tube (Figure 3.4). The two hemicilinders move relative to their starting position because during the slow rising part of the waveform, the sample holder and the glass tube follow the piezoelectric contraction. During the fast portion of the sawtooth waveform the sample stage does not follow the piezo and the Pyrex holder motion as the inertial force due to the large acceleration exceeds the static friction. The size of each step depends on the mass of the sample holder, on the elastic constant of the spring, on the voltage applied to the piezotube, on the period of the sawtooth, on the operating temperature and on the surface materials (the contact area is cleaned by using ethanol). A coarse step of ~2 nm (or less depending on the spring elastic constant) can be obtained at room temperature by applying a sawtooth signal with amplitude of 120 V and a period of 5 μs (Figure 3.4(b)). As the maximum z-elongation of the outer tube is ~100 nm (tube sensitivity = 1.49 nm/V), at least 40 coarse steps can be made without crashing the tip into the surface. In between two coarse steps, the sample is moved towards the tip by applying a slow sawtooth signal (~100 μs, Figure 3.4(a)) and, if the tunnelling current set-point value is recorded, the approach stopped and the feedback turned on. In case the tip-sample distance is too large and no tunnelling

(a)

(b)

(c)
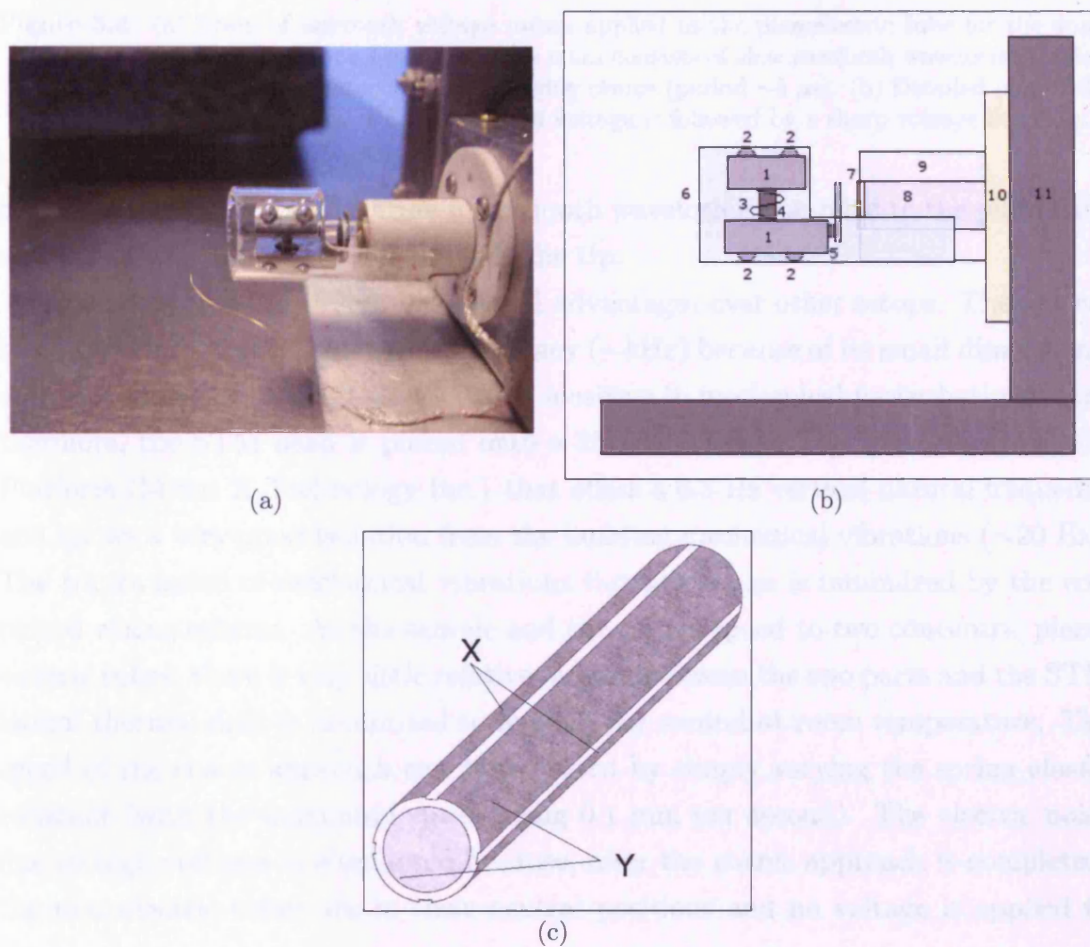
Figure 3.3: (a) Picture and (b) schematic diagram of the STM head. (c) Schematic diagram of the inner piezoelectric scanner showing its outer wall sectioned into four electrodes parallel to the tube axis that are used for driving the tip in the X and in the Y direction.
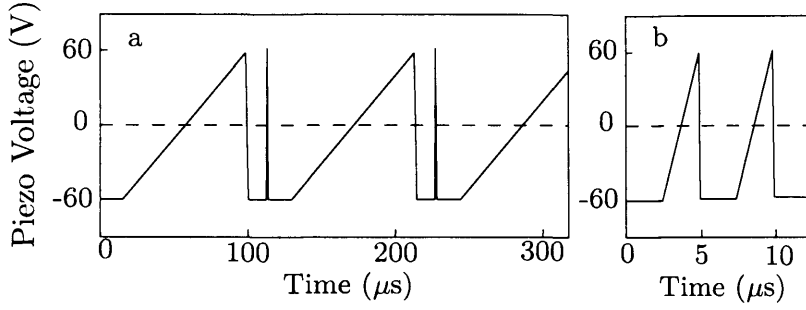
Figure 3.4: (a) Train of sawtooth voltage pulses applied to the piezoelectric tube for the automatic coarse approach. The pulse train consists of slow sawtooth waveforms (period ~100 μs) alternated with fast driving ramps (period ~5 μs). (b) Detailed plot of the driving sawtooth: a linear raise in voltage is followed by a sharp voltage decrease.

current is recorded, another train of sawtooth waveforms is applied to the piezo tube and the sample moves further towards the tip.

The adopted STM design has several advantages over other setups. The system has a very high natural resonance frequency (~kHz) because of its small dimensions, and the rigidity of its head makes it less sensitive to mechanical perturbations. Furthermore, the STM head is placed onto a 25-BM-8 Bench Top Vibration Isolation Platform (Minus K Technology Inc.) that offers a 0.5 Hz vertical natural frequency and allows a very good isolation from the building mechanical vibrations (~20 Hz). The transmission of mechanical vibrations through cables is minimized by the employed wiring scheme. As the sample and the tip are glued to two concentric piezoelectric tubes, there is very little relative motion between the two parts and the STM lateral thermal drift is minimized to few pm per second at room temperature. The speed of the coarse approach can be adjusted by simply varying the spring elastic constant (with the maximum speed being 0.1 mm per second). The electric noise due to high voltages is eliminated because, after the coarse approach is completed, the piezoelectric tubes are in their neutral positions and no voltage is applied to them.

3.2.2 STM Electronics

A schematic diagram of the home-built STM control and data acquisition electronics is shown in Figure 3.5. It consists of a computer running the open source DSP software GXSM-2 [132], a DAC/ADC Signal Ranger STD board (Soft dB), three low-voltage operational amplifiers (AD820) used in a summing-amplifier configuration, five high-voltage amplifiers (OPA445AP) that control the piezoelectric scanners and a low-noise current to voltage operational amplifier (OPA111) with a variable gain (10^8-10^9 V/A). The arrows in Figure 3.5 indicate the direction of the electronic
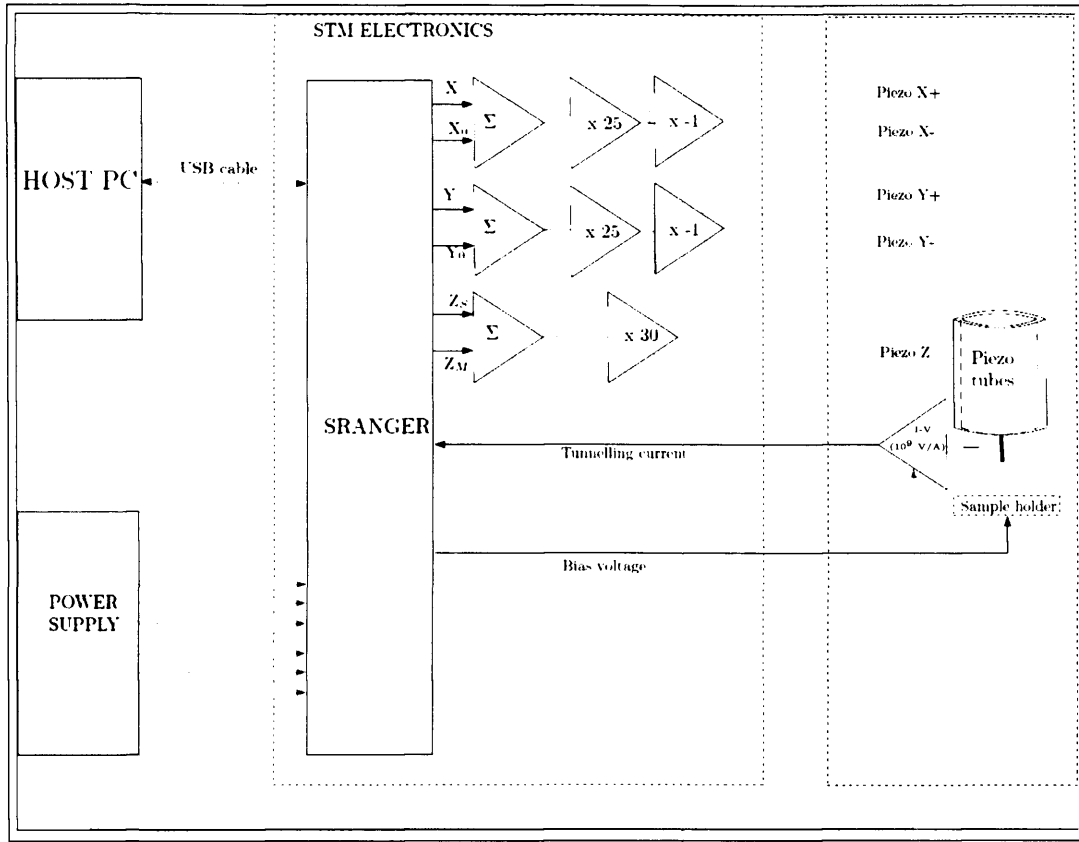
Figure 3.5: Schematic diagram of the STM electronics.

signals. For instance, the DSP board converts the analogue voltage from the current-voltage amplifier into a digital signal and sends it to the control software. A C++ program compares the input signal with a preset value of the tunnelling current and calculates the control signal according to the feedback parameters defined by the user (i.e. gain of the proportional and integral (P-I) controllers). The feedback voltage is fed through a DAC board into the summing amplifiers and then into the high-gain amplifiers that drive the piezoelectric tubes. The experimental settings, such as the tunnelling current set-point, the bias voltage, the P-I controllers gain, the scanning speed and range can be changed by using the software GXSM-2 that also generates the topographic images and the I-V characteristics.

The low-noise current-voltage operational amplifier is housed in a shielded box next to the STM head in order to minimize the noise due to capacitive coupling (Figure 3.2). In order to reduce the vibrational noise, the sample holder is connected to the amplifier through a 2 cm long, 50 μm diameter gold wire soldered to a flexible 0.25 μm diameter coaxial cable. The total length of the wires is kept as small as possible in order to prevent loss in the circuit bandwidth due to a large RC time constant (i.e. the longer the wire, the higher the capacitance of the line). The
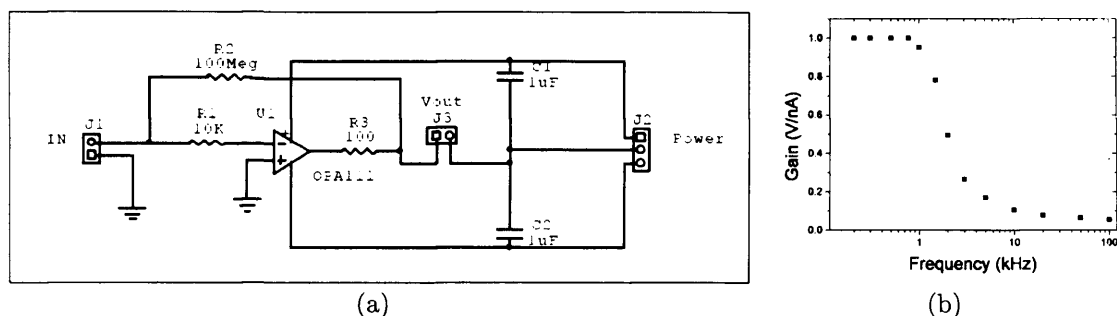
**Figure 3.6:** (a) I-V converter circuit schematics and (b) its Bode diagram (amplifier gain against logarithm of frequency).

current to voltage amplifier (Figure 3.6(a)) has a gain that can be varied up to 10^9 V/A and it was operated mostly at the maximum gain as currents as small as few pA are measured in the I-V experiments. When operating at a gain of 10^9 V/A, the bandwidth of the amplifier is $\sim$1 kHz (Figure 3.6(b)) and the output voltage noise is $\sim$5 mV (a 1 GΩ resistance was used for testing purposes).

The Signal Ranger STD board is built around a 100 MHz/100 MIPS TMS320C5402 digital signal processor and it interfaces with the host PC via USB cable (Figure 3.7). The eight 16 bit sigma-delta analog outputs are used to drive the piezoelectric voltages and to apply the bias voltage to the sample. On the other hand, only one of the eight 16 bit sigma-delta analog inputs is used in the experimental setup to input the signal from the current to voltage amplifier to the PC. The STD board has an output range of $\pm$2.06 V and a maximum input voltage of $\pm$10 V. As the performed I-V experiments did not require voltages higher than 1 V or lower than -1 V, the bias voltage was not amplified helping to reduce the electronic noise applied to the tunnelling junction.

The four high-voltage amplifiers ($\pm$40 V) (Figure 3.7) drive the inner piezoelectric tube. By applying a voltage to the outer wall of one of the outside quadrants of the piezo tube relative to the grounded inner part of the tube and a voltage of the opposite sign to the opposite quadrant, the scanner bends perpendicularly to its axis (Figure 3.3(c)). By simultaneously controlling the voltage applied to the four electrodes the tip is laterally moved to raster the sample or to be placed on a specific location of the sample surface. As the sensitivity of the inner piezo to lateral motion is 7.5 nm/V and the DAC has a resolution of $\sim$61 μV, the STM maximum lateral scan range is $\sim$600 nm and its lateral resolution is $\sim$0.1 Å. While the high lateral resolution is fundamental for achieving atomic resolution and for performing single molecule measurements, a scan range larger than 600 nm was not required for the single-molecule experiments performed in this project. Furthermore, the STM lateral resolution can be improved by using a lower gain of the amplifier and using
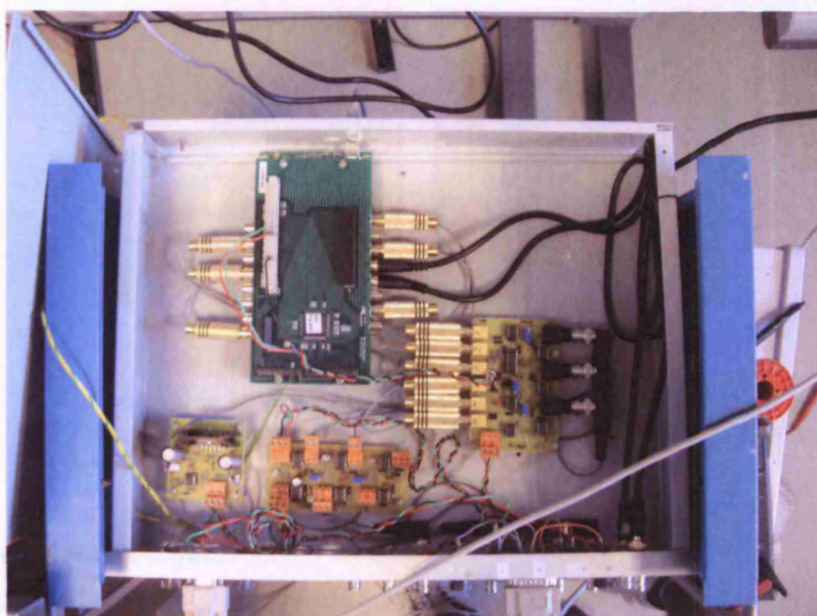
Figure 3.7: Picture of the opened box housing the STM electronics. The Signal Ranger is the green board; the other three circuit boards are from left to right the voltage amplifier that drives the piezo scanner in the z direction, the voltage amplifiers for driving the piezo tubes in the X and Y directions, the summing amplifiers used to offset the center of the scanning area.

the summing amplifiers to offset the voltage applied to the scanning tubes. In fact, the high-voltage amplifiers have a variable gain (x 0.25, x 2.5, x 25) that is controlled by changing the trigger voltage of an integrated AD4111 amplifier. The STM system does not have the capacity to perform an x, y coarse motion. However, I found that the scan area can be changed by simply withdrawing the sample and approaching it again. In fact, while the sample holder slides over the glass tube it also rotates and, as its axis is not aligned with the axis of the smaller piezo, a different area of the sample is presented to the probing tip.

3.3 Piezoelectric tubes calibration and STM results

The sample holder-tip and the piezo coaxial arrangement of the home-built STM prevented calibration of the piezoelectric scanners by capacitive or interferometric measurements. Therefore, atomic resolution images of highly ordered pyrolytic graphite (HOPG) were taken by using mechanically cut platinum-iridium (90% Pt - 10% Ir) tips 0.25 mm in diameter and used for calibration purposes. STM tips were cleaned in ethanol to remove any impurity from the tip apex. Freshly, flat cleaved HOPG surfaces were obtained by pressing a piece of tape to the HOPG sample and
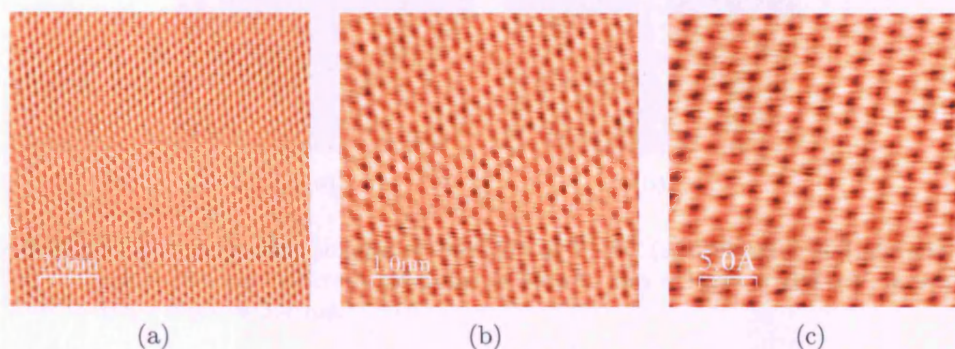
(a)   (b)
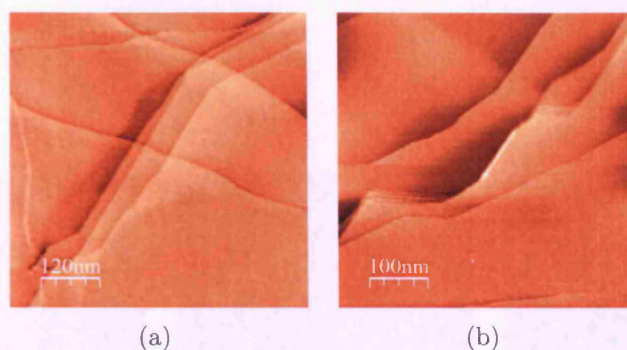
Figure 3.8: STM topographic images of HOPG at 21 °C (a) 600 nm x 600 nm and (b) 500 nm x 500 nm. Current set-point = 50 pA, bias voltage = 100 mV, scan rate = 7 Hz, z-scale=21 Å.

peeling away the top layer.

Sharp step edges and atomically flat surfaces can be observed in large area STM scans performed in constant-current mode (Figure 3.8). By comparing the distance between different graphite planes reported in literature (3.4 Å) [17, 18] with the one I measured, the piezoelectric tube sensitivity for vertical scanning was evaluated to be 14.9 Å/V. Atomic resolution of HOPG surface was routinely achieved (Figure 3.9). Figure 3.9(c) shows a high resolution STM image of HOPG (25 Å) and Figure 3.10 a schematic diagram of the HOPG hexagonal lattice; a good agreement between the HOPG lattice spacing and the STM image can be observed. In order to interpret the HOPG images, we have to remember that the electrical conductivity of the carbon atoms in a graphite crystal lattice changes because neighbor atoms lay in two different planes with the carbon atoms of the upper layer (black dots, Figure 3.10) being more conductive (closer to the tip) than the ones of the lower layer (grey dots, Figure 3.10). The piezoelectric sensitivity was calculated to be 75 Å/V in the x and y directions by comparing the accepted carbon-carbon distance in HOPG (2.46 Å) [20] with its measured values. The calculated calibration values of the piezoelectric tubes sensitivity well agree with the theoretical sensitivity (16 Å/V in the z direction for the bigger piezo tube and 90 Å/V in the x and y direction for the smaller piezo tube). Atomic resolution achieved on large scale images (Figure 3.9(a) and (b)) showed uniform lattice spacing, suggesting that the piezo scanner deflection in the x and y direction is equal, and that the two piezo scanners are coaxial and thermally matched.

The stability of the STM was also tested on Au(111) surfaces (Figure 3.11). The images show large and flat gold terraces. With the control electronics switched on for more than an hour and the piezoelectric tubes in thermal equilibrium, the lateral thermal drift of the tip relative to the sample was measured to be ≤3 pm/second.

Figure 3.9: STM topographic images of HOPG at 21 °C (b) 10 nm x 10 nm, (b) 5 nm x 5 nm and (c) 2.5 nm x 2.5 nm. Current set-point = 50 pA, bias voltage = 100 mV, scan rate = 7 Hz, z-scale=5 Å. The lattice distance measured in Figure (a), (b) and (c) is 0.25 nm and well agrees with the values reported in literature for carbon-carbon distance [17].
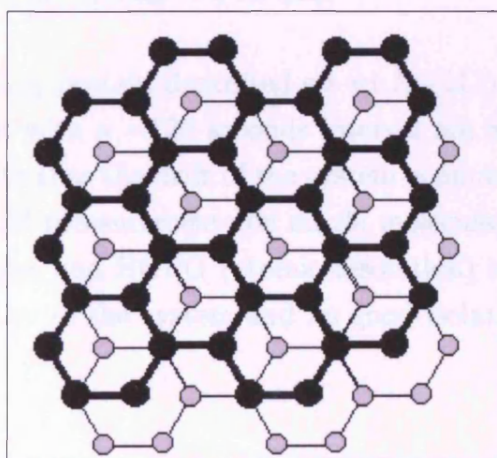
Figure 3.10: Schematic representation of the HOPG lattice showing two graphene planes (black and gray dots).
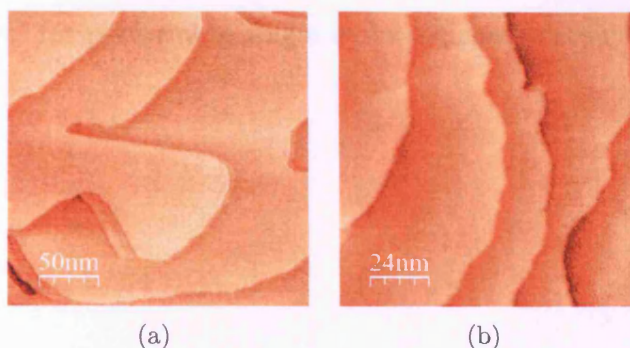
Figure 3.11: STM topographic images of Au(111) at 21 °C (a) 250 nm x 250 nm and (b) 120 nm x 120 nm. Current set-point = 50 pA, bias voltage = 100 mV, scan rate = 7 Hz, z-scale = 3.4 nm.
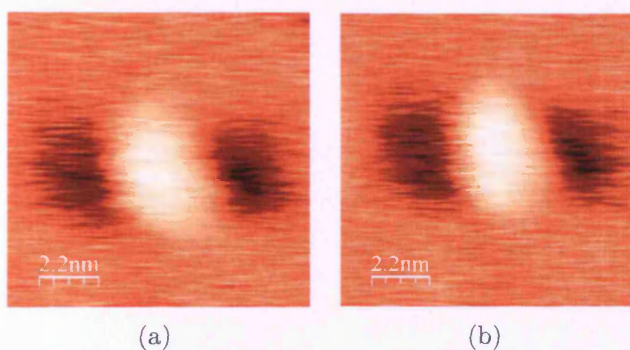
Figure 3.12: STM images of holo-SH-SA cyt b_{562} on Au(111) image acquired (a) before and (b) after I-z experiment with a ∼120 seconds interval (see chapter 4 for experimental details). The images show the STM system low drift in the x and y scanning directions (∼3 pm per second). The images were acquired at constant I_t = 50 pA and V_b = -20 mV (z-range = 0-0.6 nm).

STM images of a cyt b_{562} protein deposited on an Au(111) surface (see Chapter 4 for more details) taken with a ∼120 seconds interval are shown in Figure 3.12(a) and (b) and demonstrate that the drift of the system is minimum making it ideal for performing I-V and STS measurements on single molecules. The results achieved by scanning gold samples and HOPG (atomic resolution) in air at room temperature confirm the stability of the system and its good isolation from electronic and mechanical noise.

3.4 Conclusions

In this chapter I have described the design and the operating principles of an STM based on two concentric small piezoelectric tubes. Atomic resolution STM images of HOPG confirmed the stability of the system to mechanical vibrations. STM images of proteins deposited on Au(111) surfaces showed the low lateral drift of the system

that is fundamental for performing single molecule spectroscopy measurements.

Chapter 4

STM and AFM characterization of cyt b_{562} in air

The sulfur-gold bond is a widely used approach to realise metal-organic molecule contact. However, the possibility of using two thiol groups at opposite ends of a protein has never been investigated as a means to contact two separate electrodes. In this chapter I describe the SPM characterization of the wild-type cyt b_{562} and of the two cyt b_{562} variants SH-SA and SH-LA engineered with pairs of cysteine residues. The effect of the thiol group in anchoring the protein to a Au(111) surface is investigated by AFM and STM imaging and presented in the first part of the chapter. The electronic properties of the studied systems and results of the I-V_b and I-z experiments are reported and discussed further.

4.1 Introduction

The idea of using single molecules to realize future electronic devices has led to a growing interest over the past few years in the use of organic molecules in electronics [55, 125]. Redox active proteins have emerged as candidates for use in nanoelectronics as they are natural electron-transfer components utilised in different processes in nature, including energy production and catalysis [39]. Their small dimensions, mechanical flexibility, ability to self-assemble and electron transfer and tunable redox properties provide proteins with the significant potential to be incorporated in miniaturised organic electronic devices [47, 48, 78, 79]. Furthermore, high-sensitivity nano-biosensors, capable of detecting single molecular events by measuring electric signals, could be realized for clinical diagnostic applications [23]. It has already been demonstrated that the electronic properties and functionality of proteins can be tailored by engineering through defined mutagenesis without disrupting their re-

dox activity [7, 10]. Given their potential for nanotechnological applications, it is important that control can be exerted on binding to conductive surfaces and that understanding of the electron transfer properties on coupling to such surfaces is achieved [74, 118].

4.1.1 Protein deposition on gold substrate

The site-specific deposition of metalloproteins on bare gold surfaces has been achieved by chemisorption via:

1. an exposed cysteine residues of wild-type proteins;

2. an anchoring group introduced in the protein amino acid sequence by site-directed mutagenesis.

For example wild-type azurin containing a disulfide bridge [28, 29, 31, 33] and yeast cytochrome c bearing a free cysteine [21, 22, 42, 64, 71] have been directly immobilized on bare gold surfaces. In this case the protein orientation on the substrate can not be decided *a priori*, because it depends on the position of the cysteine residue in the wild-type protein. On the other hand, the selection of a pre-determined orientation can be achieved by the introduction of thiol group(s) or disulfide bridge(s) by site-directed mutagenesis. Several groups have successfully used this approach to immobilize plastocyanin [7, 9], putidaredoxin [97] and cytochrome P_{450} monooxygenases [36, 38] on gold electrodes.

As single organic molecule can be detected and studied only if the substrate roughness is at least one order of magnitude lower than the protein size (0.5-1 Å), the choice of the substrate is of primary importance. The Au(111) substrate has been the first choice for single molecule characterization as it completely fulfills this requirement. In fact if gold deposited on glass surface is exposed to a gas flame, or if it is evaporated on mica substrate, hundreds of nanometers atomically flat terraces may be obtained. Their roughness typically ranges among 0.05 nm and 0.1 nm. In metalloproteins studies the freshly prepared Au(111) surface is usually incubated with the protein solution (concentration in the range 5-100 μM) at 4° C for times ranging between 5 minutes and 12 hours depending on the desired coverage. After the incubation, the samples are rinsed with buffer solution in order to remove any unadsorbed material from the substrate [21, 24, 64].

4.1.2 Scanning probe microscopy imaging of metalloproteins

Proteins have been widely investigated by different approaches including ultraviolet, visible and infra-red absorption, Raman and fluorescence spectroscopy, EXAFS, NMR, XPS, X-Ray and electrons diffraction, electrochemistry, ellipsometry and surface plasmon resonance [3]. Even if this great scientific effort has brought a deep understanding of the structure and function of metalloproteins, most of these techniques relay on the average signal of a large number of molecules. SPM techniques have overcome this limit by permitting the detection and characterization of single proteins in real time and even in physiological conditions. Several groups have described the successful imaging of proteins by SPM. As reported by Davis [38], these studies have included cytochrome c, cytochrome c_{551}, phosphorylase b, phosphorylase kinase, glucose oxidase, catalase, azurin, haemoglobin, rubredoxin, putidaredoxin, metallothionein and cytochrome $P_{450}cam$.

Azurin is the most extensively [3, 23, 27, 36, 53, 137] metalloprotein studied by SPM methods at a single molecule level. This protein contains an exposed disulfide bridge that is suitable for gold anchoring. In the first study of this kind [53], after incubation in the protein solution, the Au(111) substrate was found to be covered of a globular molecule monolayer of regular size (Figure 4.1(a)). Since these features were not observed when the substrate was rinsed in deionised water and imaged with the same method (Figure 4.1(b)), the deposited material was deduced to be the metalloproteins. At high magnification the azurin monolayer could be well resolved with a resolution of 0.1 nm showing 3.5-4 nm diameter in accordance with crystallographic values (3.5 nm). These data, as pointed out by the authors, were consistent with a non-denaturing immobilization process and SPM imaging.

Successive studies investigated the immobilization of azurin proteins on gold surfaces through the introduction of a surface cysteine residue via site-directed mutagenesis [38]. After the incubation of Au(111) in the protein solution, well defined and stable protein monolayers were observed by both TM-AFM and STM imaging (Figure 4.1(c)).

Cytochrome c has also been extensively investigated by SPM methods and it has been found that the protein deposits uniformly on gold and stably binds to the surface only if a cysteine residue is present in the protein's aminoacid sequence [10]. In fact, while yeast iso-1-cytochrome c adsorbs on Au(111) surface through its exposed cysteine 102 (Figure 4.2(a)), equine cytochrome c, that does not have any surface cysteine, adsorbs on gold surfaces aggregates in clusters [22]. However, if the protein sequence is mutated by using site-directed mutagenesis (T102C mutation), the protein stably adsorbs on bare Au(111) (Figure 4.2(b)) [10].

(a)   (b)   (c)
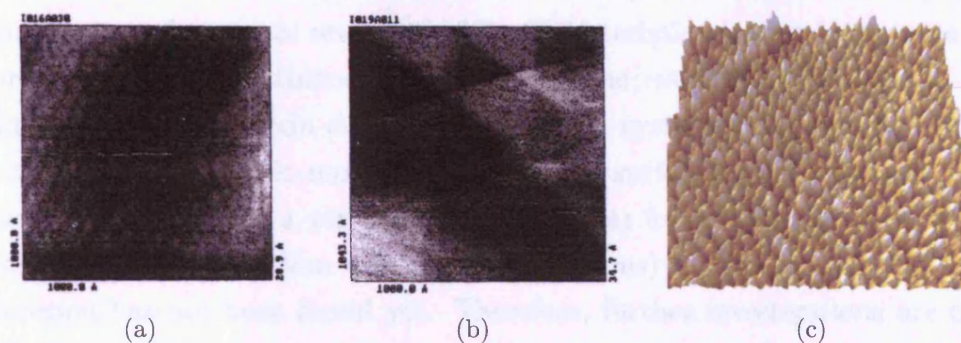
Figure 4.1: STM images (a) of azurin molecules immobilised on Au(111) and (b) of a Au(111) surface in 50 mM ammonium acetate buffer, pH 4.65. Current set point 2 nA, bias voltage 240 mV, substrate potential 240 mV vs NHE [53]. (c) STM image of engineered azurin molecules immobilised on Au(111) in 15 mM potassium phosphate buffer, pH 7. Image size is 140 nm x 140 nm [38].

(a)   (b)
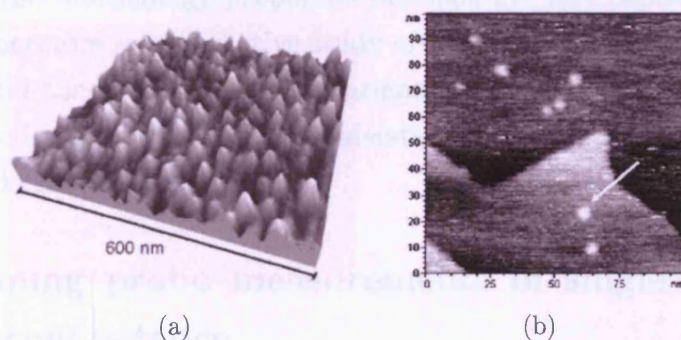
Figure 4.2: STM images of (a) yeast iso-1-cytochrome *c* molecules [22] and (b) T102C equine cytochrome *c* [10] immobilised on Au(111). Current set point 50 pA, bias voltage 0.6 V.

It is worth to note that the affinity for gold is not the same for all the metal-loproteins. For example, while the thiol moiety seems to be fundamental for the cytochrome c adsorption on Au(111), other proteins like the zinc metallothionein from rabbit [37] and the rubredoxin from *Clostridium pasteurianum* [36] can be deposited on a gold surface and imaged by SPM techniques even in absence of an anchoring group (metallothionein bears 20 cysteine residues all involved in metal coordination and rubredoxin does not contain any cysteine). As the absorption of proteins and other organic molecules on metallic surfaces is very difficult to pre-dict as it is influenced by a variety of intermolecular forces (covalent and hydrogen bonds, dipole-dipole and Van der Waals interactions) a clear explanation for this phenomenon has not been found yet. Therefore, further investigations are critical to understand the fundamental features of the protein-metal electrode interactions.

Although the large perspectives offered by the SPM methods, until recently only few research group focused their attention on the combination of SPM analysis for protein characterization [40]. Most of the research has instead used only one kind of analysis that can bring to misinterpret the proteins properties. TM-AFM experiments can in fact provide a deep understanding of the proteins height and orientation onto the substrate, but are limited by the relatively large size of the tip that can broaden the proteins' lateral dimension. On the other hand, STM imaging can depress the proteins changing their height and a high current tunnelling signal can be related to metal rich zones. Nevertheless, STM imaging allows a deep insight into the proteins lateral dimensions thanks to the small tip size and the related low tip convolution. In this study both TM-AFM and STM analysis have been used to characterise the morphology properties of single cyt b_{562} deposited on Au(111) substrate. Furthermore a comparative study of wild-type proteins lacking any gold-linking group and the cyt b_{562} cysteine variants bearing the thiol groups has been carried out in order to allow a deeper understanding of the thiol role in anchoring proteins to Au(111) surfaces.

4.1.3 Scanning probe measurements of single metalloprotein conductance

Electronic properties at the single molecule level can be probed in a variety of ways, with conductivity measurements via two electrical contacts being of particular tech-nological importance [25, 116]. In the last few years techniques have emerged that generate two metallic contacts separated by a gap of few nanometers [98]. These include electron beam lithography [114], mechanical break junctions [93] and Au nanoparticles sandwiches [34, 66]. Among these techniques, STM based experiments

have allowed current-voltage (I-V$_b$) [16] and current-distance (I-z) [67, 68] measurements on single molecules and have been widely used for investigating molecular conductance in a variety of systems [98]. In I-V$_b$ experiments the STM tip is held over the top of a molecule which is immobilized on a metallic surface while the voltage is ramped and the current is measured. In the I-z method the STM tip is driven towards the molecule then slowly retracted while keeping the voltage constant and measuring the current flowing between the two electrodes. To date this approach has been successfully applied to small organic molecules (alkanedithiols [73], conjugated aryl-dithiols [130], porphyrins [108], viologen [88]), but never to molecules as large and complex as proteins.

The conductive properties of single proteins have been mainly characterized by I-V$_b$ measurements. The studies by Andolfi *et al.* on two different poplar plastocyanin mutants provide an extensive investigation concerning the conductance of a metalloprotein [5, 6, 7, 8, 9]. In one of the two protein variants a disulfide bridge (PCSS) was inserted in the protein sequence, while in the other (PCSH) a residues tail (Thr-Cys-Gly) was added as C-terminal extension [6]. The I-V$_b$ experiments performed in air and under nitrogen atmosphere showed a good coupling between the mutant proteins and the Au(111) surface. The diode-like I-V$_b$ curves appeared markedly asymmetric for PCSS mutants, almost symmetric for PCSH, whereas the tunnelling curves for the bare Au substrate were highly symmetric (Figure 4.3). The authors ascribed the rectifying behaviour of the Au/protein/tip junction to the presence of the copper redox site involved in the tunnelling mechanism [7]. It was also speculated that the different conductivity properties of the two mutants were related to the different adsorption modes of the molecules on the gold surface with the disulfide group allowing a better contact to the electrode.

The work by Andofi *et al.* provides the first evidence of good electronic coupling between a redox protein and a metallic electrode. However, a more efficient and effective coupling of the protein with both the metallic electrodes could be achieved by insertion of thiol groups at opposite ends of the molecule. In Chapter 2 I described the synthesis and purification of the two cyt b_{562} variants SH-SA and SH-LA with double cysteine residues inserted at opposite ends/faces of the cytochrome, along its long and short axes respectively (section 2.1). The introduction of thiol-pairs should allow the proteins to bind the metallic surface in defined orientations utilising one thiol group while retaining desired functions and leaving the second thiol group available for potential coupling to the STM tip. UV-Visible absorption and hemin titration experiments have demonstrated that the introduced cysteine mutations do not affect the protein's haem binding properties. In this chapter the electronic

(a)   (b)
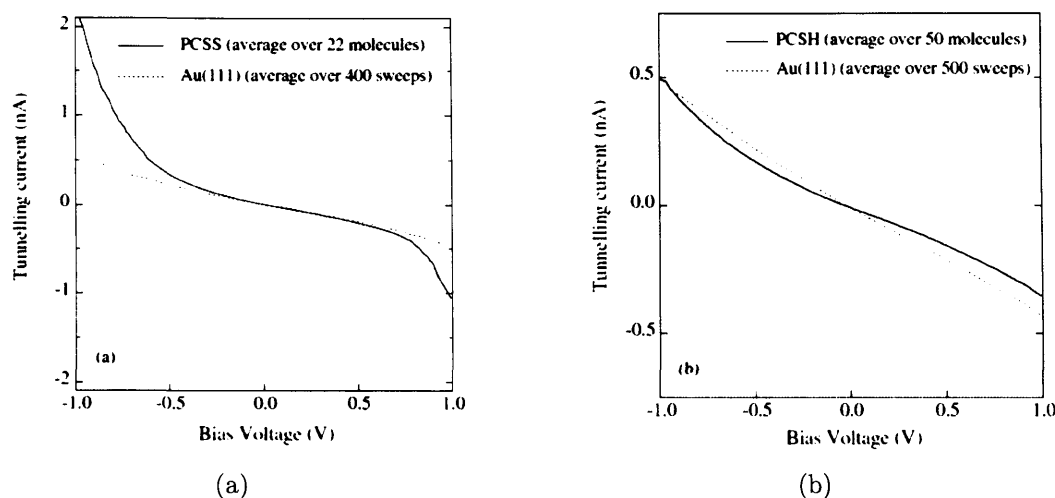
Figure 4.3: I-V_b curves recorded in ambient conditions (a) 22 PCSS molecules (data for each molecule are averaged over 10 I-V_b sweeps) and Au(111); (b) 50 different PCSH molecules (10 sweeps are averaged for each molecule) and Au(111). The tunnelling current and bias voltage set point are 50 pA and 0.180 V (tip positive), respectively [6].

properties of the wild-type, SH-SA and SH-LA cyt b_{562} adsorbed on Au(111) surface investigated in air by a combination of AFM, STM, current-voltage (I-V_b) and current-distance (I-z) techniques are reported and discussed.

4.2 Experimental

4.2.1 Sample preparation

Wild-type, SH-SA and SH-LA cyt b_{562} proteins used in the experiments were expressed, purified and analyzed by UV-Visible spectroscopy as described in Chapter 2.

Au(111) bead single crystals electrodes were used to perform AFM and STM experiments. The Au substrate showed reconstructions of 111 orientation and high quality terraces (200 nm wide) when imaged using STM in absence of protein sample (see figure 3.11). The Au(111) electrodes were cleaned by electropolishing in 1 M H_2SO_4 and washed with 0.1 M HCl and water. The samples were annealed for 8 hours at 880 °C in order to obtain recrystallized terraces [32]. Prior to the protein deposition, the electrodes were annealed and the Au(111) single crystal surface was protected with deionized water. The electrodes were subsequently incubated in protein solution for times varying from a few minutes to hours with protein concentrations determined measuring the absorbance at 280 nm of the apoprotein and at 418 nm of the oxidised holoform, using molar absorption coefficients of 3 mM^{-1}

cm^{-1} and 117 mM^{-1} cm^{-1}, respectively [103]. For the I-V$_b$ and I-z measurements the samples were incubated with 5 μM protein solution (10 mM phosphate buffer pH 6.2 and 50 mM NaCl) at room temperature for 5 minutes. Samples were rinsed with ultra pure water by Millipore (resistivity 18.2 MΩ cm) in order to remove the weakly bound proteins and the buffer excess, gently dried with a flow of nitrogen and then imaged.

4.2.2   SPM experiments

AFM and STM studies were conducted in air under ambient conditions. All AFM measurements were carried out using a Multimode microscope equipped with a Nanoscope III controller (DI Veeco, Santa Barbara, USA) operating in non-contact mode with polysilicon probes. Triangular cantilevers were purchased from NT-MDT (Moscow, Russia) with a nominal spring constant $k = 5.8$ N/m and a resonant frequency $f = 120$ kHz.

STM, I-V$_b$ and I-z experiments were performed in air at room temperature using the home-built STM described in Chapter 3. The system is equipped with an I-V$_b$ converter with a sensitivity of 1 nA/V. STM tips used throughout the experiments were mechanically cut from Au(99.9%) 0.25 mm diameter wires (Goodfellow, UK). STM images were recorded in constant-current mode with scan rates 5-11 times the scan size.

The AFM and STM images were post-processed (flattening) and analysed using WSxM Scanning Probe Microscopy Software [75].

I-V$_b$ and I-z measurements were performed after scanning the substrate and checking for tip integrity. Once single protein resolution was achieved and thermal drift had stabilized (few pm/s), the Au tip was placed above a protein at a tunnelling resistance of 2 GΩ (50 pA, 0.1 V with the sample held at a negative potential). In the I-V$_b$ experiments the feedback loop was then disengaged and the current was recorded with the voltage ramping between -0.75 V and +0.75 V for typically 20 seconds (10 curves measured per second). In the I-z experiments the tip was moved towards the sample by 2 nm. After disengaging the feedback loop, the tip was moved away from the sample at a rate of 20 nm/s and the current recorded as function of tip distance. In order to be able to perform a meaningful statistical analysis, the measurements were performed on a large number of proteins deposited on different Au(111) surfaces with various Au tips.

4.3 Results and discussion

4.3.1 AFM and STM imaging

To confirm that the engineered SH-SA and SH-LA variants adsorbed on Au(111) surface in the desired orientations, single molecule analysis by AFM and STM were performed. Self-assembled cyt b_{562} proteins were observed all over the surface indicating that good binding between the molecules and the substrate was achieved (Figure 4.4).

As a control, STM imaging of fresh Au(111) substrates incubated with 10 mM phosphate buffer alone and washed with deionised water was performed over a wide range of tunnelling current set-points and bias voltages (figure 3.11). None of the features observed when the Au(111) surface was incubated with the proteins were observed in the absence of proteins (i.e. bright spots onto the substrate, surface roughening). The density of protein displayed on the surface could be tuned from a few molecules per hundreds of square nanometer up to full monolayer coverage by varying the incubation time (from minutes to several hours) and the protein concentration (2 μM-50 μM). When the Au(111) substrates were incubated for 5 min with 5 μM of holo-SH-LA cyt b_{562}, AFM scans (Figure 4.4(a)) revealed proteins with a low surface density homogeneously assembled and robustly bound to the metallic surface. When the protein concentration was increased to 20 μM and incubated for an hour, the whole gold surface was covered with a dense and uniform protein monolayer (Figure 4.4(b)). Both the SH-LA and SH-SA cyt b_{562} variants were imaged onto the metallic surface upon successive AFM scans, indicating that strong binding between the molecules and the gold surface was established. Analysis of high resolution AFM images showed that the SH-LA molecules have a circular shape with a diameter of about 15 nm (Figure 4.4(a)), while the SH-SA cyt b_{562} revealed an elliptical shape with a long axis of about 25 nm and a short axis of about 15 nm (Figure 4.4(b)). Due to the geometry and relatively large size of the probing tip, the proteins' lateral dimensions evaluated by AFM imaging were at least five times higher than the ones revealed by analysis of the atomic resolution 3D structure of cyt b_{562} determined by X-Ray diffraction. Nevertheless these results indicate different modes of adsorption of the two cyt b_{562} variants onto gold substrates.

To study the electronic properties of single cytochrome molecules, a low protein density is required. Therefore, low protein concentration solutions (2-5 μM) of the cyt b_{562} variants were incubated with Au(111) substrates for a short time (5 minutes). When imaged by STM under a constant current (50 pA), individual molecules of wild-type, SH-SA and SH-LA cyt b_{562} could be clearly seen as single bright spots

(a)   (b)
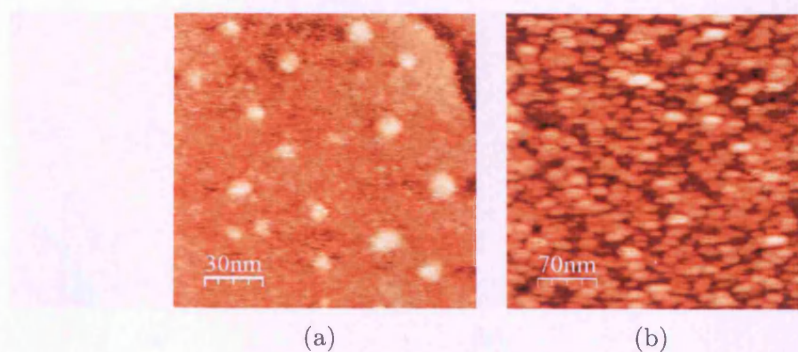
Figure 4.4: AFM images of (a) individual holo-SH-LA cyt b_{562} on Au(111) (z-range = 0-4.5 nm) and (b) a packed monolayer of holo-SH-SA cyt b_{562} on Au(111) (z-range = 0-5.2 nm).


(a)   (b)
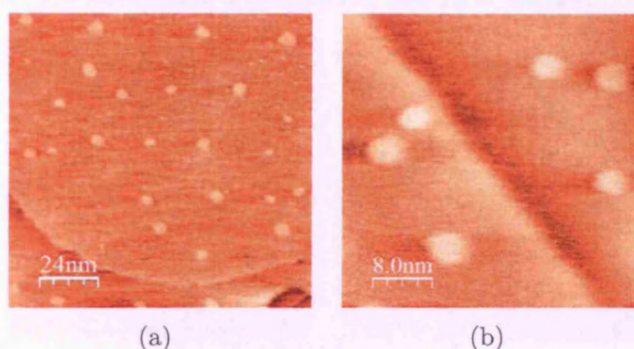
Figure 4.5: STM images of (a) holo-SH-LA and (b) holo-SH-SA cyt b_{562} on Au(111) (I_t = 50 pA; V_b = -20 mV; z-range = 0-1.35 nm).

on the flat gold surface (Figure 4.5(a) and 4.5(b)). High resolution STM images of isolated, self-assembled cyt b_{562} onto the gold substrate were reproducibly obtained. This result indicated that physico-chemical binding can be achieved between the molecules and the substrate.

Importance of the introduced thiol group is demonstrated as STM observations of the wild-type cyt b_{562} were not as robust as the ones of the cysteine variants and the thiol-free proteins were swept away after few scans of the same area (Figure 4.6). In the first STM scans of wild-type proteins adsorbed onto pristine Au(111) few proteins cover the Au surface (Figure 4.6(a)). Most of the proteins are then removed by the tip in successive scans due to tip/sample interactions (Figure 4.6(b) and (c)). As no protein agglomerates were found at the edges of the scanned areas, the proteins could be adsorbed on the water layer that surrounds the STM tip in ambient conditions. In the case of wild-type cyt b_{562}, none of its natural residues can act as a linker to the gold substrate and weak physical adsorption appears responsible for the protein self-assembly onto Au(111). Statistical analysis of the STM images showed a large variation of the protein's dimensions indicating that the wild-type proteins did not adsorb in a preferred and oriented manner onto the

<center>(a)   (b)   (c)</center>
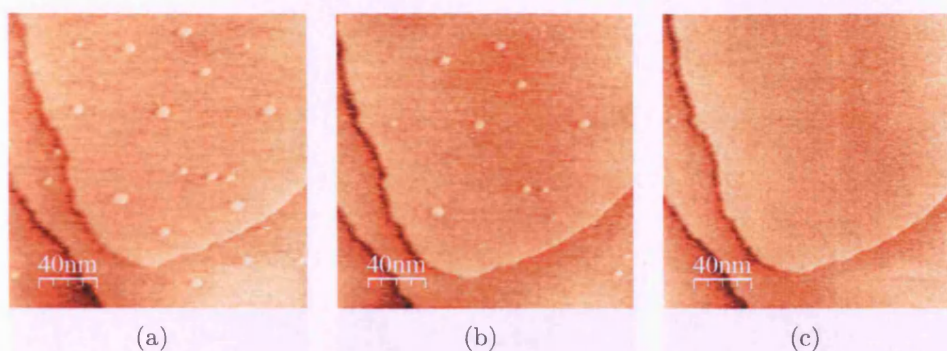
Figure 4.6: STM images of holo-wild-type cyt b_{562} on Au(111) (a) 1st scan (z-range = 0-2.7 nm), (b) 2nd scan (z-range = 0-2.0 nm), (c) 3rd scan (z-range = 0-1.6 nm). The images were acquired at constant I_t = 0.05 nA and V_b = -20 mV.

<center>(a)   (b)</center>
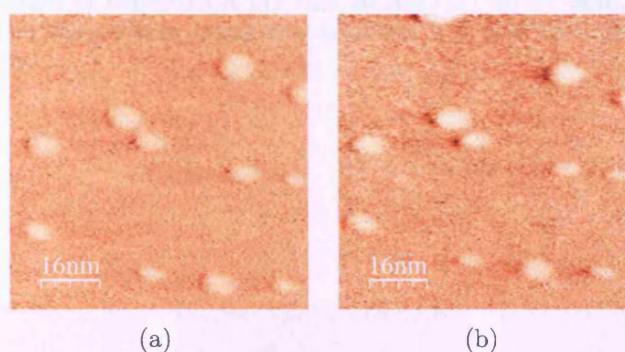
Figure 4.7: STM images of holo-SH-SA cyt b_{562} on Au(111) (a) 1st scan, (b) 7th scan. The images were acquired at constant I_t = 50 pA and V_b = -20 mV (z-range = 0-1 nm).

metal substrate (Table 4.1). On the other hand, when the cysteine mutant proteins self-assemble onto the gold surface, single molecules can be observed (Figure 4.7(a) and 4.8(a)) and the same area can be scanned continuously without removing the proteins or losing imaging resolution (Figure 4.7(b) and Figure 4.8(b) and (c)). The robust and reproducible STM imaging of SH-SA and SH-LA cyt b_{562} suggested that the presence of the thiol groups through the introduced cysteine residues allowed the molecules to be bound tightly to the gold surface (Figure 4.7 and 4.8).

Even though robust binding of the cyt b_{562} variants was achieved, care had to be taken when imaging the sample; proteins were swept away when the STM tip was too close to the surface, as is the case for high set point currents or very low bias potential. The tip then interacted sufficiently strongly with the proteins to disrupt them, as can be seen in Figure 4.9. This observation might explain why some proteins cannot be imaged using STM techniques [37, 96].

As high quality STM images were obtained for all the proteins adsorbed onto Au(111), statistical analysis of hundreds of molecule length and height with a resolution of 0.5 Å could be performed (section 3.3). The sizes were evaluated from

Figure 4.8: STM images of holo-SH-LA cyt b_{562} on Au(111) (a) 1st scan, (b) 5th scan, (c) 10th scan. The images were acquired at constant $I_t = 0.05$ nA and $V_b = -20$ mV (z-range = 0-1 nm).
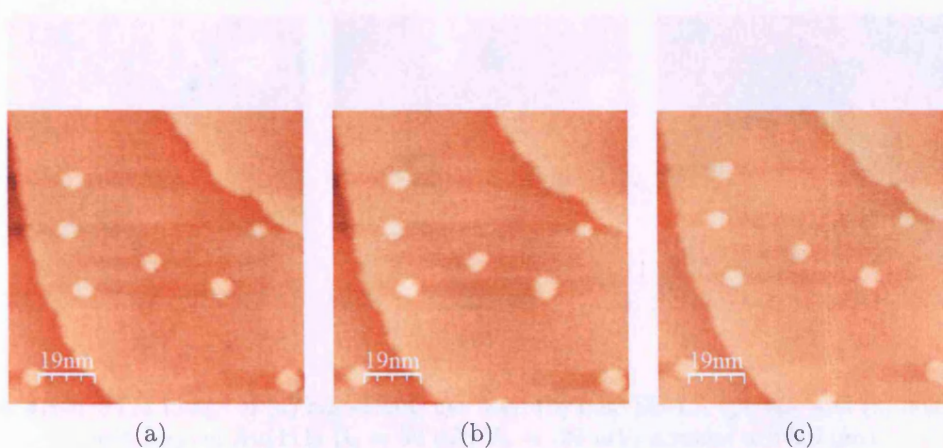

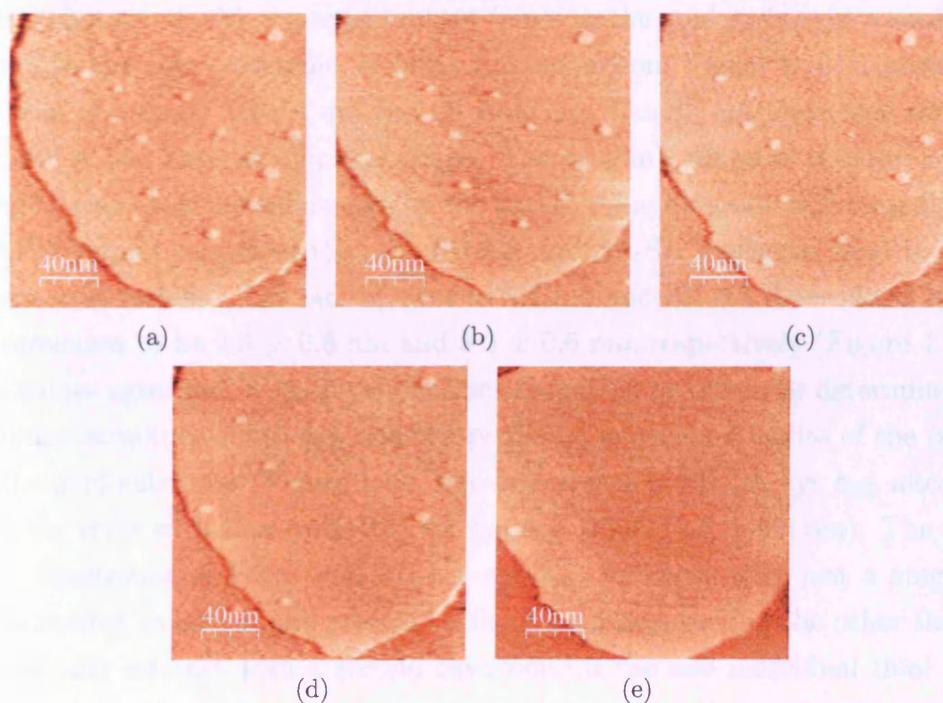**Figure 4.9:** STM images of holo-SH-SA cyt b_{562} on Au(111). The images were acquired at constant $I_t = 0.05$ nA and $V_b = -20$ mV (z-range = 0-2.5 nm) ((a) 1st scan, (b) 2nd scan); and at constant $I_t = 6$ nA and $V_b = -20$ mV ((c) 3rd scan (z-range = 0-1.9 nm), (d) 4th scan (z-range = 0-2.2 nm), (e) 7th scan (z-range = 0-1.2 nm).
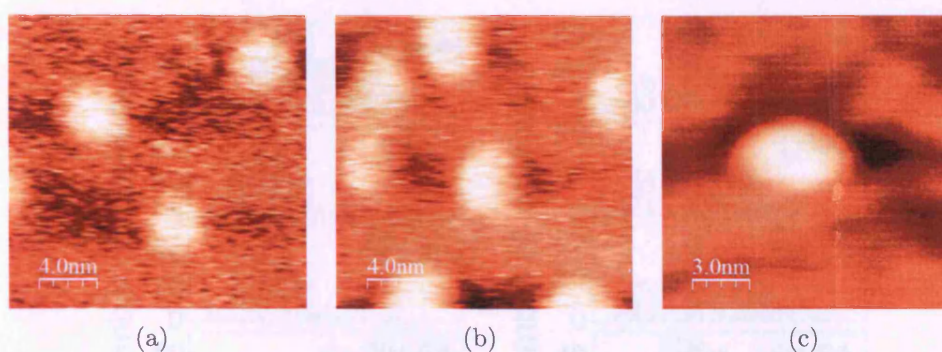
Figure 4.10: STM image of (a) holo-D50C cyt b_{562}, (b) holo-SH-LA cyt b_{562} and (c) holo-SH-SA cyt b_{562} on Au(111) (I_t = 50 pA; V_b = -20 mV; z-range = 0-0.6 nm).

cross sectional analysis of single molecules with lateral and vertical size being the dimensions at half height of the single profiles (Table 4.1). The cyt b_{562} crystallographic structure can be described as a cylinder 5.1 nm in height and 2.4 nm in diameter (Figure 2.1). The STM image of several SH-LA cyt b_{562} double cysteine variants (Figure 4.10(b)) is very similar to that observed for the cyt b_{562} variant in which only Asp50 is mutated to a cysteine (cyt b_{562} D50C, Figure 4.10(a)). This suggests that the double cysteine mutant binds to the gold surface in a similar orientation to the single cysteine variant. In comparison, Figure 4.10(c) presents an STM scan of a single SH-SA cyt b_{562} on Au(111). The SH-SA molecules are bigger than SH-LA and have an elliptical shape. The protein's shape as revealed by STM and AFM scans was not influenced by the tip scanning direction and both the STM and AFM results suggested that the SH-LA and SH-SA molecules bind to gold in different orientations. The lateral sizes of SH-LA and SH-SA determined by STM were measured to be 2.3 ± 0.6 nm and 5.0 ± 0.6 nm, respectively (Figure 4.11(a)). These values agree well with the dimensions suggested by distances determined from the atomic structure of cyt b_{562} and the predicted adsorption modes of the proteins onto the gold substrate (Figure 1.1). The lateral size of SH-LA cyt b_{562} also agrees within the error with that measured for cyt b_{562} D50C (2.6 ± 0.6 nm). The similar lateral dimensions of D50C and SH-LA cyt b_{562} indicates that just a single cysteine is needed to anchor the protein to the Au surface, leaving the other thiol free to potentially interact with a second electrode. If the two individual thiol groups bound to the surface, the protein would appear on the surface as bright spots with dimensions similar to that of the SH-SA molecule as the protein would be anchored to the gold surface at both ends. In comparison, the lateral size of the wild-type cyt b_{562} was less well defined with relatively high variation (3.8 ± 1.4 nm). This result suggests that the native protein does not bind into an oriented and stable manner due to the lack of a specific anchoring group in the protein sequence.
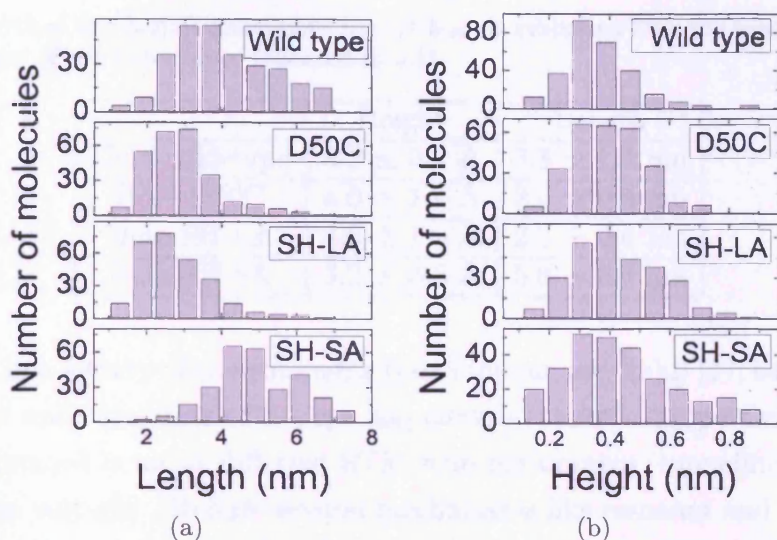
Figure 4.11: Statistical analysis of wild-type, D50C, holo-SH-LA and holo-SH-SA cyt b_{562} molecules (a) length and (b) height on the Au(111) surface measured in air in STM mode. The dimensions were evaluated from cross sectional analysis of 280 different proteins.

The apparent height of all the proteins onto the gold surface was about 3-4 Å (Figure 4.11(b), Table 4.1). These dimensions are much smaller than that anticipated from analysis of the atomic-level molecular structure of cyt b_{562}, but this feature is characteristic of STM imaging of biomolecules adsorbed onto metal surfaces [38]. In fact the protein's energy Fermi level and the one of the underlying surface are very different and, as the apparent height of molecules measured in STM imaging is a convolution of electronic and topographic properties, the proteins' vertical dimension deviates from the predicted value. The STM data can be complemented with the analysis of the AFM experiments. In fact, even though the lateral resolution achievable with an AFM probe depends on the tip size and it is appreciably poorer than that for STM, the protein height can be evaluated with a higher degree of precision. When operating in non-contact mode, the AFM probe tracks the surface without mechanically deforming the sample and the protein height observed in these experiments was about 2 nm for SH-SA and 4 nm for SH-LA (Figure 4.4), close to the crystallographic values.

4.3.2 STM imaging for the β decay factor

STM and its related methods can not just provide an insight into the structure of a protein assembled onto metal surfaces with resolution down to the angstrom scale, but these non-destructive techniques have now developed to the point where electronic properties of single organic molecules can be easily monitored over long

Table 4.1: Vertical and lateral dimensions for cyt b_{562} as evaluated from the mean and the variance of the histograms presented in 4.11.

	Height	Length
Holo-wild-type	3.2 ± 0.5 Å	3.8 ± 1.4 nm
Holo-D50C	4.0 ± 1.4 Å	2.6 ± 0.6 nm
Holo-SH-LA	4.0 ± 1.0 Å	2.3 ± 0.6 nm
Holo-SH-SA	3.2 ± 0.5 Å	5.0 ± 0.6 nm

time periods in a variety of environments (i.e. vacuum, air, fluid) [37, 64]. In order to gain a deeper understanding of the cyt b_{562} electron transfer properties, the mutant SH-LA was imaged in air at different STM scan parameters (tunnelling current setpoint and bias voltage). To date several mechanisms like resonant and non-resonant tunnelling, electron-hopping and ionic conduction have been proposed to explain the current tunnelling through a protein bridged between two contacts [137]. However, none of them can fully explain electron flow through organic macromolecules that have a very large band gap (5-7 eV) and are insulators from a "classical physical" point of view ($\rho = 10^{16}$-10^{17} Ωm). If we assume that in STM experiments only low voltages are applied, the junction conductance due to electrons tunnelling through a 1D-barrier can be described by a simple exponential equation [119, 124]:

$$I = I_0 e^{-\beta L} \tag{4.1}$$

where β is the tunnelling decay coefficient, L is the barrier width, I is the measured current and I_0 is a parameter that varies linearly with V_b. The β factor is a property of the barrier medium and the smaller its value, the smaller the decrease in current with distance through the gap. As cyt b_{562} is an electron carrier that transfers electrons between other redox centers [54, 100], the β decay constant describes its efficiency to promote electron tunnelling. Several theoretical studies have attempted to calculate this electronic parameter for proteins, but there are very few reports that have used an experimental approach to systematically investigate the protein β factor. The value for cyt b_{562} SH-LA was measured by imaging the sample at different tunnelling current set-points (range 0.05 nA-5 nA) and at a fixed sample bias (V_b = -20 mV). The apparent height of the protein is 4.5 ± 0.2 Å at 0.05 nA, 4.0 ± 0.15 Å at 0.5 nA and 2.5 ± 0.1 Å at 5 nA with the molecule looking "taller" at lower current set-points (Figure 4.12). As the single STM images were acquired in constant current mode, the change in contrast indicates that, in order to measure large tunnelling currents, the tip had to get close to the sample. The protein's apparent height can be plotted as a function of the current set-point (Figure
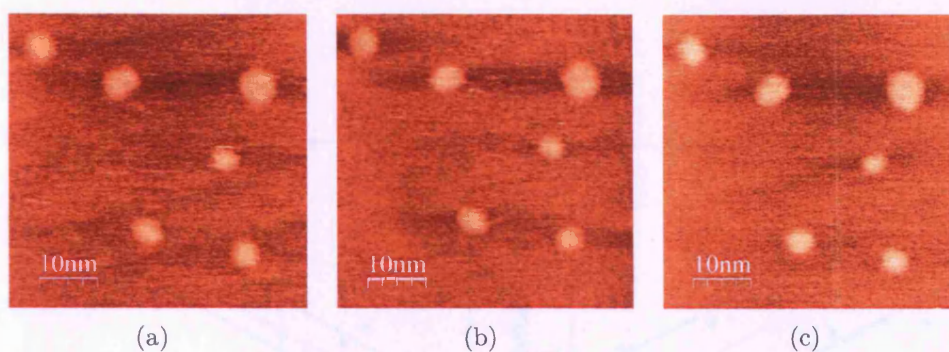
Figure 4.12: STM images of holo-SH-LA cyt b_{562} on Au(111) at (a) $I_t = 0.05$ nA (z-range = 0-1.2 nm), (b) $I_t = 0.5$ nA (z-range = 0-1.05 nm), (c) $I_t = 5$ nA (z-range = 0-0.7 nm). The images were acquired at constant $V_b = -20$ mV.

4.13(a)) and, assuming that the tip is in contact with the protein and that the tunnelling decay coefficient for vacuum is sufficiently large [89], the β decay constant for the protein estimated using equation (4.1). The proteins show similar variation in contrast as a function of set-point with an evaluated β factor of 1.57 ± 0.25 Å^{-1}. Further evidence of the tunnelling mechanism through the SH-LA was also revealed in the STM experiments performed at different V_b with a constant tunnelling current of 50 pA (Figure 4.14). An exponential variation of protein's height in relation to the applied potential was observed, with the protein's vertical dimension being higher at higher bias (Figure 4.13(b)), suggesting that a larger tunnelling probability through the molecule was achieved in this state.

The β factor determined for cyt b_{562} is lower than those reported for vacuum or air ($\beta \approx 3$ Å^{-1}) explaining why it appears as a zone of positive contrast on the gold surface. The protein has a decay factor consistent with others reported in literature for azurin and cytochrome c and evaluated by I-V_b STS techniques (1.4 Å [35]) and presents electron tunnelling characteristics similar to saturated hydrocarbon chains (1.2 Å [87]) and short peptide molecules (1.1 Å [129]), suggesting that the tunnelling mechanism through the protein in air is off resonance.

4.3.3 I-V_b measurements

In order to study the electron transfer properties of the wild-type and the two cyt b_{562} variants self-assembled on Au(111) surfaces in different respective orientations and the role of the free thiol in enhancing the contact with a second electrode, I-V_b measurements were performed. Before measuring the I-V_b curves, the molecules were imaged and checked for integrity comparing their lateral dimensions with that of the known molecular structure of cyt b_{562} (Figure 4.15(a)). When the system lateral drift was as little as a few pm per second, the tip was positioned on the center of the

(a)   (b)
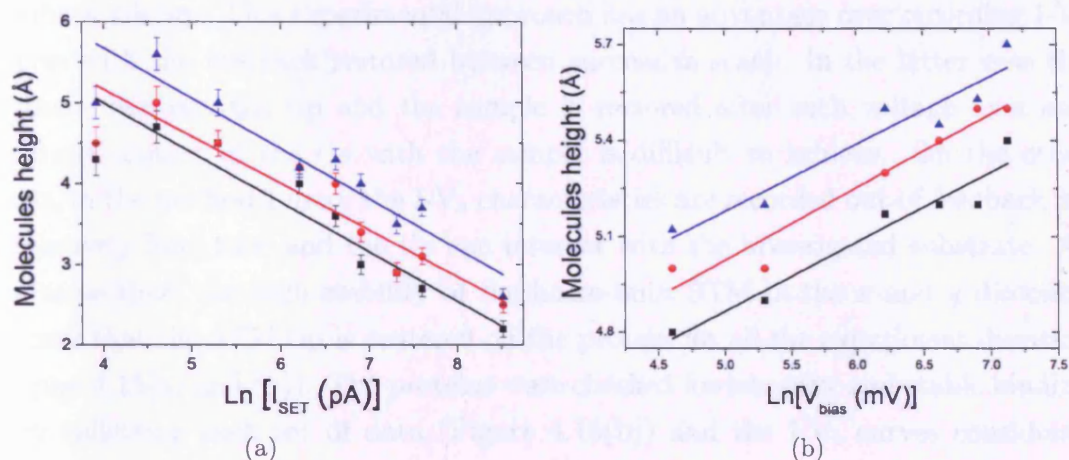
Figure 4.13: Cyt b_{562} STM imaging for β decay factor. (a) Semilogarithmic plot showing the change in apparent height as a function of the tunnelling current set-point for three different molecules (constant V_b of -20 mV). The solid curves are the best fit of the experimental data according to equation (4.1) with β equal to 1.56 ± 0.23 Å^{-1}, 1.61 ± 0.25 Å^{-1} and 1.53 ± 0.22 Å^{-1} for the black, red and blue curve, respectively. The error bars are the measured fluctuations in z-direction over the gold surface that decrease as the STM tip is closer to the sample. (b) Semilogarithmic plot showing the change in apparent height against the bias voltage for three different molecules at a constant I_t of 50 pA (error bars are not shown to improve the clarity of the figure). The solid curves are the best linear fit of the experimental data.

(a)   (b)   (c)
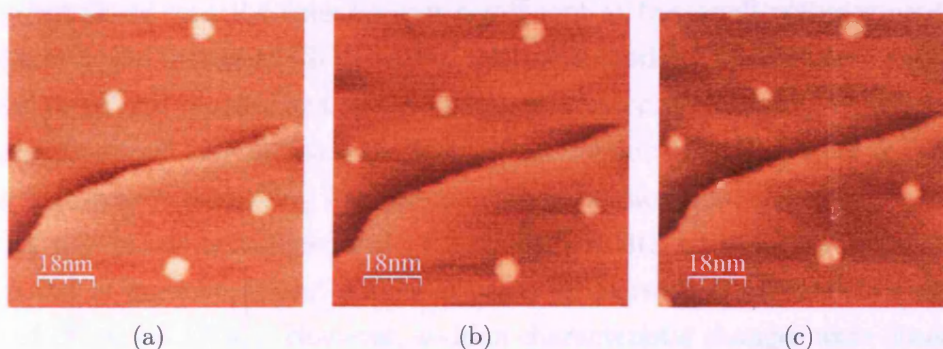
Figure 4.14: STM images of holo-SH-LA cyt b_{562} on Au(111) at (a) $V_b = 20$ mV (z-range = 0-1.4 nm), (b) $V_b = 1000$ mV (z-range = 0-1.55 nm), (c) $V_b = 2000$ mV (z-range = 0-1.7 nm). The images were acquired at constant $I_t = 50$ pA.

globular structure and the I-V$_b$ curves recorded. The home-built STM described in Chapter 3 allows to record several hundred curves without re-establishing the feedback system. This experimental approach has an advantage over recording I-V$_b$ curves with the feedback restored between successive scans. In the latter case the distance between the tip and the sample is restored after each voltage scan and intimate contact of the tip with the sample is difficult to achieve. On the other hand, in the method I used, the I-V$_b$ characteristics are recorded out of feedback for a relatively long time and the tip can interact with the investigated substrate. At the same time, the high stability of the home-built STM in the x and y direction ensures that the STM tip is centered on the protein for all the experiment duration (Figure 4.15(a) and (b)). The proteins were checked for integrity and stable binding after collecting each set of data (Figure 4.15(b)) and the I-V$_b$ curves considered for analysis (Figure 4.16) were only the ones where the proteins' dimensions were not modified by the tip during the experiments. Also from time to time the tip crashed onto the sample with the problem evidenced by formation of a large gold agglomerate ($\sim$400 nm^2) on the substrate (Figure 4.15(c)) and in these cases the I-V$_b$ curves were also disregarded. The I-V$_b$ curves were recorded in a low bias range (-0.75 V, +0.75 V) and fitted to a third order polynomial function:

$$I = AV_b + BV_b^3 \qquad (4.2)$$

where A is the low bias conductance $[S]$, (i.e. the first derivative of the current with respect to voltage near 0 $(dI/dV_{V \to 0})$) and B $[V^2]$ is a coefficient that describes the non-linearity of the I-V$_b$ curve. The I-V$_b$ experimental curves were also fitted using a second order polynomial term or a higher order polynomial function (5th order), but these contributions are not significant at the small voltages used in the experiments. By fitting the I-V$_b$ curves with this model, the low bias conductance was evaluated and plotted against the number of the corresponding recorded curve. Information about any increase or decrease in conductance due to change in tunnelling distance or tunnelling barrier could then be measured.

With the system out of feedback, the tip drifted either towards or away from the sample and in most cases just a slow increase or decrease in current over time was observed (Figure 4.17(a)). However, sudden characteristic changes were observed in 15-20% of the I-V$_b$ traces when probing SH-SA and SH-LA molecules (Figure 4.16(b) and (c)). These differences in the I-V$_b$ curves were revealed by jumps in $dI/dV_{V \to 0}$ against scan number and are attributed to the binding of the free thiol to the STM tip (Figure 4.17(c), (d) and (e)). The low bias conductance against scan number plots obtained for SH-SA (Figure 4.17(c)) and SH-LA (Figure 4.17(d), (e)) showed

(a)   (b)   (c)
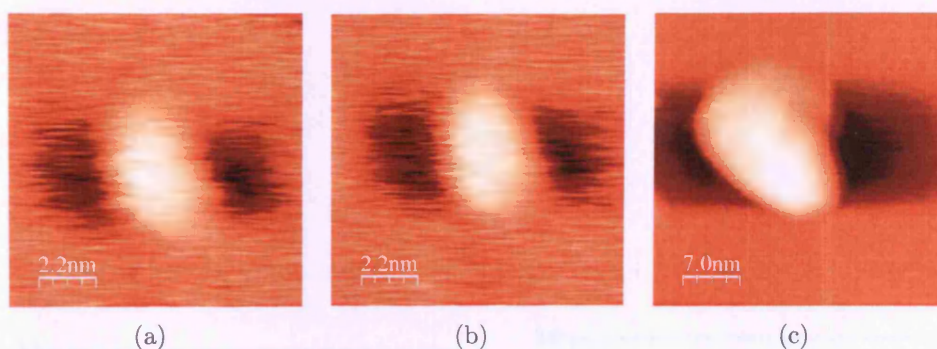
Figure 4.15: STM images of holo-SH-SA cyt b_{562} on Au(111) image acquired (a) before and (b) after the I-z experiments (z-range = 0-0.6 nm). The STM system has a very low drift ($\sim$3 pm per second) in the x and y scanning directions. (c) Au(111) surface after the tip has entered into contact with the substrate (z-range = 0-3.2 nm). The images were acquired at constant I_t = 50 pA and V_b = -20 mV.

jumps of $\sim$1-3 x 10^{-5} G_0 (G_0 = 77.4 μS). Similar events have been recorded in current measured as a function of time (I-t) experiments conducted with alkanedithiols [67] and short DNA molecules functionalised with two thiol groups [123]. I-V_b curves were also recorded for the wild-type protein (Figure 4.16(a)). Although jumps in conductance were revealed for the native protein (Figure 4.17(b)), they were always an order of magnitude lower ($\sim$2 x 10^{-6} G_0) than the ones found for the cysteine variants, indicating that the junction resistance was higher and a good contact between the protein and the electrodes could not be achieved.

The low bias conductance values measured for SH-SA (Figure 4.17(c)) were more stable over time than SH-LA with a possible reason being a more robust binding of the protein sulfur group to the tip in the former case. In addition, the experiments performed on SH-LA (4.17(d) and (e)) showed two values of jumps in conductance ((1.30 ± 0.05) x 10^{-6} G_0 and (2.91 ± 0.11) x 10^{-6} G_0). These two classes of values were reproducibly associated with *distinct* SH-LA proteins adsorbed on the Au(111) surface, providing strong evidence that the two conductance values are related to different orientation of the protein with respect to the gold surface resulting from immobilization via the thiol at position 21 or 50. The highest occupied molecular orbital (HOMO) and the lowest unoccupied molecular orbital (LUMO) electronic levels of the molecule broaden due to the interaction of the redox center with the electrodes [101]. Even if both the electrodes are made of gold, the broadening of the molecular energy levels at each electrode can differ as a result of the different geometry of the STM tip and the Au(111) substrate resulting in an asymmetric coupling of the molecule with the electrodes [26, 86]. This is supported by experiments performed with alkanedithiols molecules, where it has been shown that the electronic coupling between the molecules and a flat Au(111) surface is different to that with
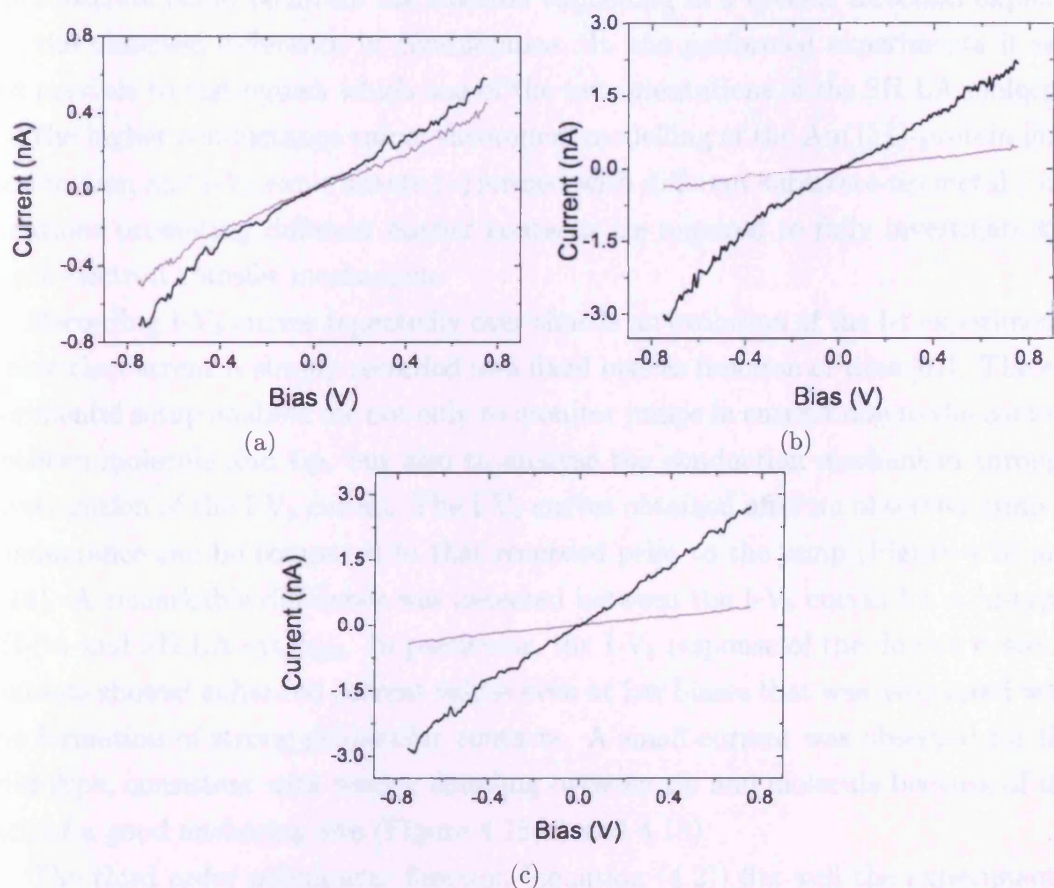
Figure 4.16: I-V_b curves observed when the gold tip is not and is in "contact" with the (a) wild-type, (b) SH-SA and (c) SH-LA protein. The STM feedback system was disengaged and the I-V_b characteristics recorded (starting engaging bias of -0.1 V and tunnelling current of 50 pA). Only one curve recorded before (grey) and one curve recorded after (black) observing a jump in the low bias conductance value are shown for clarity.

a rough gold surface [65, 87, 91]. Others have reported that the electron transfer mechanism in redox molecules involves the reduction of the metal center and its successive oxidation [101, 137]. The SH-LA protein binding the Au surface through the cysteine at position 21 has the metal center closer to the scanning tip (20 Å) than the protein binding through the cysteine at position 50 (32 Å). A closer and stronger interaction between the iron site and the tip or between the iron site and the substrate could facilitate the electron tunnelling in a specific direction explaining the observed difference in conductance. In the performed experiments it was not possible to distinguish which one of the two orientations of the SH-LA molecule has the higher conductance value; theoretical modelling of the Au(111)-protein-gold tip junction and I-V_b experiments performed with different substrate-tip metal combinations presenting different barrier contacts are required to fully investigate the exact electron transfer mechanism.

Recording I-V_b curves repeatedly over time is an evolution of the I-t experiments where the current is simply recorded at a fixed bias as function of time [67]. The experimental setup enabled me not only to monitor jumps in current due to the contact between molecule and tip, but also to analyse the conduction mechanism through investigation of the I-V_b curves. The I-V_b curves obtained after an observed jump in conductance can be compared to that recorded prior to the jump (Figure 4.16 and 4.18). A remarkable difference was detected between the I-V_b curves for wild-type, SH-SA and SH-LA cyt b_{562}. In particular, the I-V_b response of the double cysteine mutants showed enhanced current values even at low biases that was associated with the formation of strong gold-sulfur contacts. A small current was observed for the wild-type, consistent with weaker coupling between tip and molecule because of the lack of a good anchoring site (Figure 4.16(a) and 4.18).

The third order polynomial function (equation (4.2)) fits well the experimental I-V_b curves over the full bias range (inset Figure 4.18). The calculated low bias conductance values for SH-SA and for SH-LA ((3.48 ± 0.05) x $10^{-5}G_0$, (1.95 ± 0.03) x $10^{-5}G_0$ and (3.57 ± 0.11) x $10^{-5}G_0$, respectively) are higher than the one evaluated for the wild-type cyt b_{562} ((8.47 ± 0.07) x $10^{-6}G_0$). The fitting parameter B can be interpreted in a tunnelling barrier model in terms of the ratio between the width and the height of the tunnelling barrier (see reference [124] for details) and its analysis suggested that the effective barrier height (φ_0) for the wild-type protein is about two times larger than the one for the double cysteine mutants. This result is reasonable as the difference in barrier height can also be evidenced from a visual analysis of the I-V_b relation (almost linear I-V_b for the wild-type and steeper I-V_b for the cyt b_{562} variants) and confirms our hypothesis of a good thiol-Au contact for
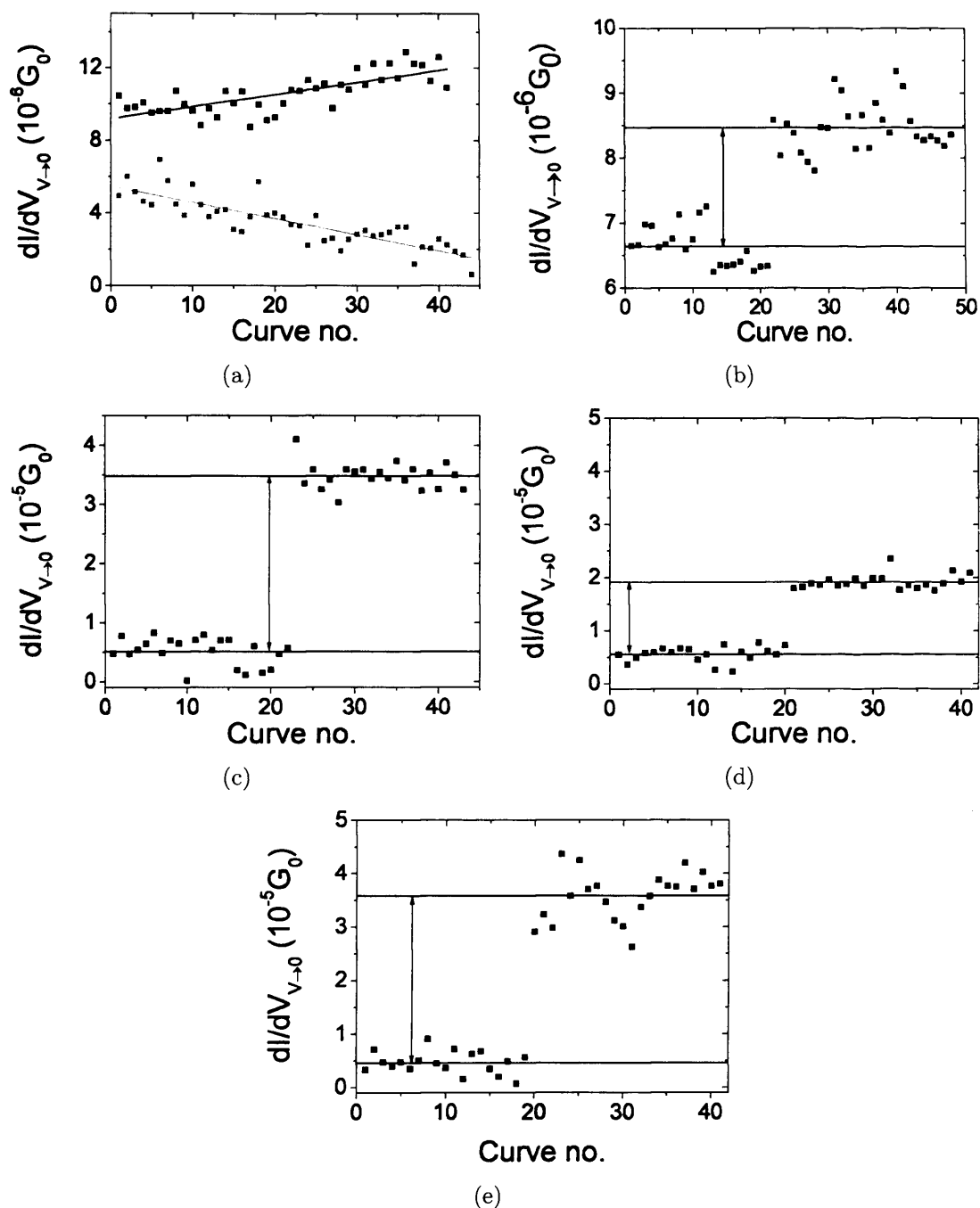
Figure 4.17: Plots showing the low bias conductance values against number of I-V$_b$ curve recorded. (a) The tip can drift towards or far from the substrate without recording any significant change in conductance. (b) Small jumps in conductance are measured when the STM gold tip approaches the wild-type protein. When the tip binds (c) the SH-SA variant or (d, e) the SH-LA molecules a relatively higher jump in conductance is recorded. See text for a detailed discussion.
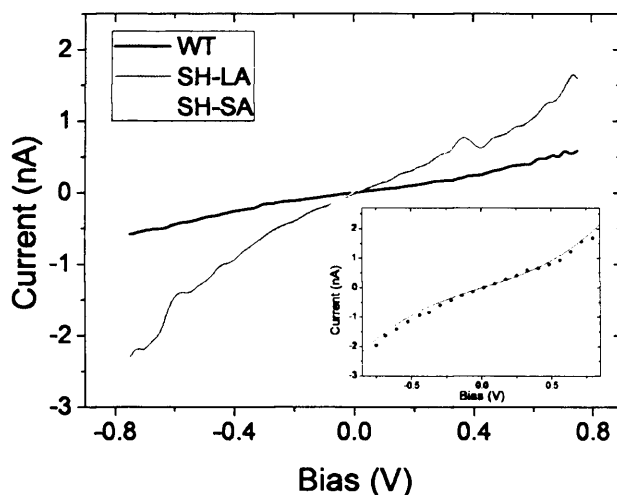
Figure 4.18: I-V_b curves observed after a jump in conductance value was observed. The STM feedback system was disengaged and the I-V_b characteristics recorded (starting engaging bias voltage of -0.1 V and tunnelling current of 50 pA). Only the average of the curves recorded after observing a jump in $dI/dV_{V=0}$ value are shown for clarity. Inset: fitting curve (line) of the experimental curve (circles) using 4.2. For clarity only one experimental sample of every 10 is plotted.

the proteins containing the thiol moieties. Lack of information about the contact area for electronic transport between the proteins and the electrodes (different from the nominal geometric contact area) does not allow to further analyse and extract absolute values for barrier height.

4.3.4 I-z measurements

In the I-z experiments the STM tip is brought into contact with the molecule and retracted while a constant voltage is applied and the current flow measured. As the tip is driven by the STM piezoelectric actuator, the tip-molecule tunnelling distance can be finely monitored and the current through the protein trapped in the junction measured as function of the probe traveled space.

In the current against distance traces recorded with the STM tip placed on top of SH-SA (Figure 4.19(b)) and SH-LA molecules (Figure 4.19(c) and (d)), an exponential decay of the current with distance was initially measured and then clear plateaus were observed. The measured current remains fairly constant as long as the Au-S bond is not broken, but as soon as the tip is driven too far and the contact is broken, the current suddenly drops [67, 68, 129, 130]. As a relatively rapid exponential decay of the current within the stretched distance without stepwise characteristics was measured for the wild-type protein (Figure 4.19(a)), the plateaus in the I-z traces of SH-SA and SH-LA molecules were interpreted as conduction through a good electronic contact between the tip and the free thiol of the protein.

The STM low lateral drift allowed stable and reliable measurements on top of single molecules. Having measured a large number of molecular junctions, robust statistical analysis could be performed and conductance histograms were calculated by dividing the raw current data by the bias voltage for the curves presenting current plateaus and converting them to histograms using 10 bins/nS (Figure 4.20 and 4.21). The histograms evaluated from I-z traces of wild-type (4.21(a)) did not show any significant peaks, while the conductance histograms for SH-SA and SH-LA (Figure 4.21(b), (c) and (d)) presented several distinct peaks. Small peaks were observed at low conductance ($\sim$2 x $10^{-5}G_0$), but they are not as pronounced as those at $\sim$5 x $10^{-5}G_0$ and that we used to evaluate the conductance of single proteins. The SH-SA variant was found to be more conductive ((6.5 ± 0.1) x $10^{-5}G_0$, Figure 4.21(b)) than the SH-LA proteins and this result could be due to the different distance between the electrodes and the haem redox center of the two molecules (Figure 1.1). In the histogram constructed for SH-LA (Figure 4.20) two clear distinct peaks were revealed and, as already noted for the I-V_b experiments, the two different conductance values are related to two separate classes of molecules (indicated with A and B in Figure 4.19(c) and (d)). The two classes of molecules did not show any significant difference in the height or lateral size of the STM scans, but current plateaus at distinct values were reproducibly observed. The conductance histograms constructed for the class of molecules A (Figure 4.21(c)) and B (Figure 4.21(d)) show well pronounced peaks at (3.45 ± 0.05) x $10^{-5}G_0$ and (5.20 ± 0.03) x $10^{-5}G_0$, respectively. The calculated conductance values are in good agreement with the low bias conductance found in the earlier I-V_b experiments involving a nominally static tip. Although they are slightly higher, the small difference can be explained considering the different biases used for their calculation (the low bias conductance was extrapolated from fitting of the I-V_b curves near zero bias, while the conductance of the I-z was calculated at a potential of -100 mV). From analysis of the I-V_b results we hypothesised that different immobilization of SH-LA onto the Au(111) surface via one of the two thiols of the cysteine residues 21 and 50 resulted in the different low bias conductance values detected for the SH-LA molecule. The larger conductivity of one of the two configurations could be due to enhanced electron transport through the molecule due to the iron center closer to the Au tip or the Au(111) substrate or to a more efficient electronic contact realised with one of the electrodes (smaller barrier to electron conduction). All the observations from the I-z experiments are consistent with the I-V_b measurements and support the contention that the surface-exposed cysteines represent an ideal way for contacting the protein with metal electrodes.
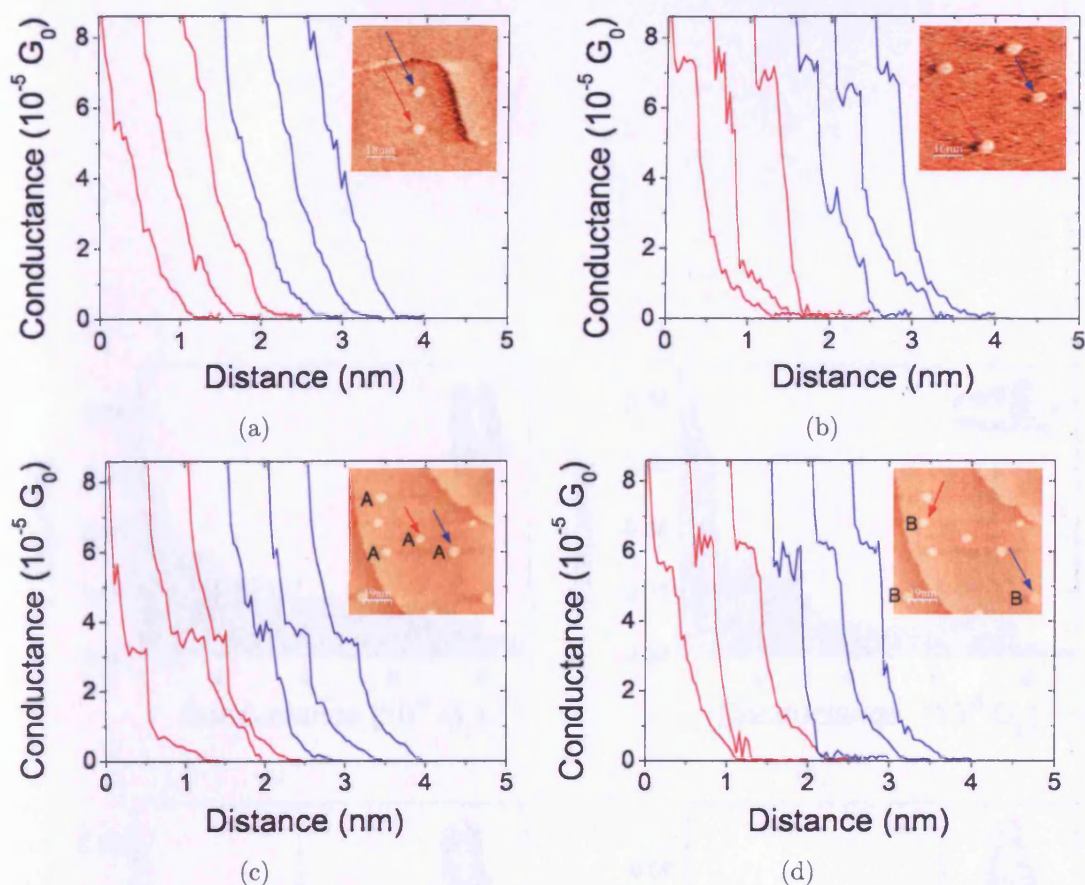
Figure 4.19: Conductance against distance curves of (a) wild-type, (b) SH-SA and SH-LA classified to (c) class A and (d) class B measured in air. Conductance was calculated as the ratio between the measured current and the applied voltage (-0.1 V). For clarity the conductance traces are displaced along the x axis. The I-z curves showed in Figure (c) and (d) were recorded on SH-LA molecules deposited onto the same region of the Au(111) surface (see inset).
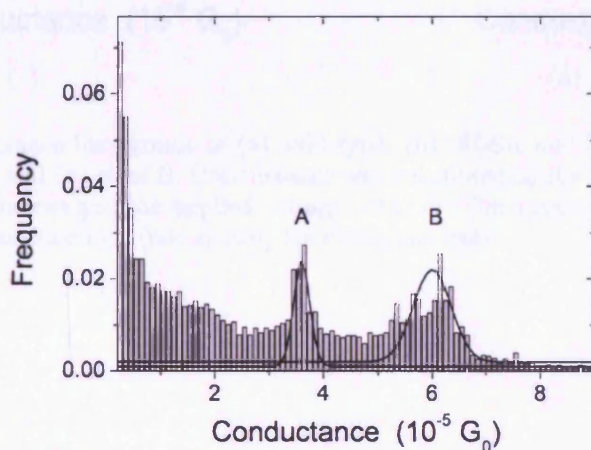
Figure 4.20: Conductance histograms of SH-LA. Conductance was calculated as the ratio between the measured current and the applied voltage (-0.1 V). The solid lines are Gaussian curves fitted to the peaks, and A and B refer to the two classes of molecules in the inset of Figure 6(c) and (d).

71
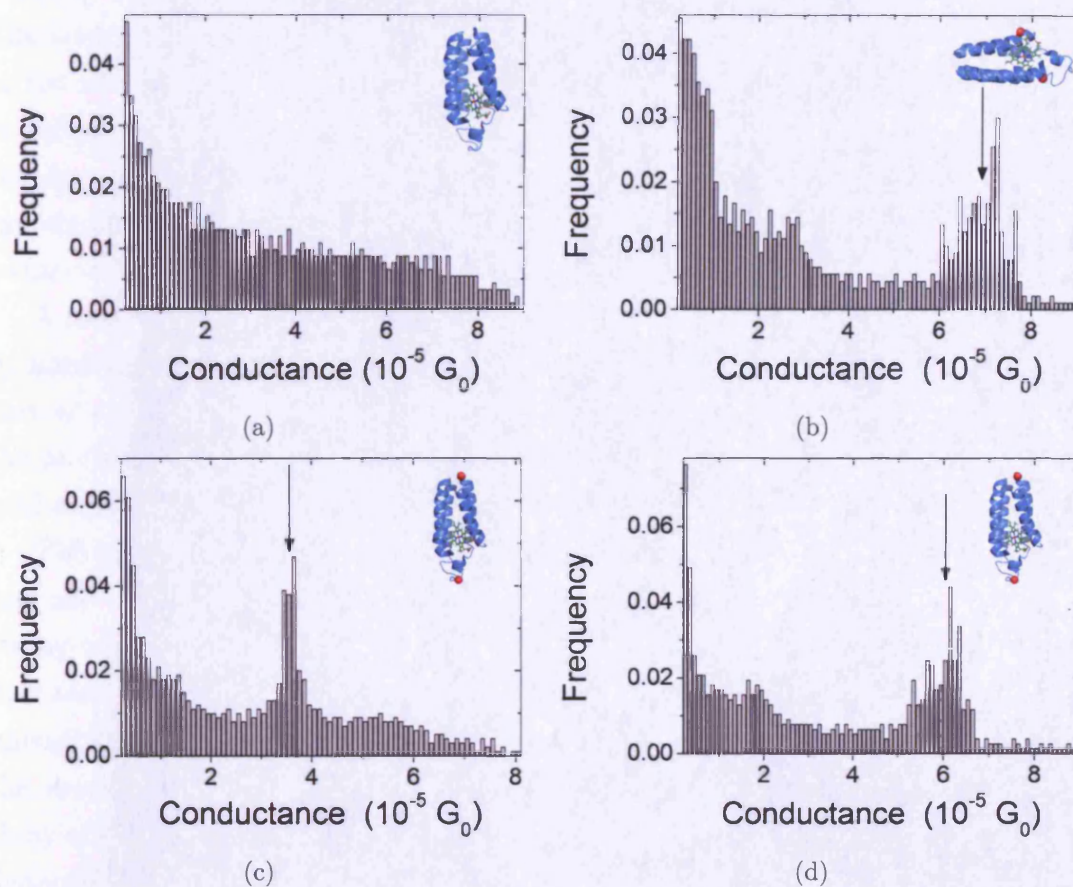
Figure 4.21: Conductance histograms of (a) wild-type, (b) SH-SA and SH-LA classified to (c) class A and (d) class B. Conductance was calculated as the ratio between the measured current and the applied voltage (-0.1 V). The arrows show the center of the Gaussian functions (not shown) for fitting the data.

4.4 Conclusions

In this chapter I have reported the AFM and STM studies of the electron transfer protein cyt b_{562} performed in air at room temperature. The poor stability of the wild-type cyt b_{562} to STM scans and the variation in lateral dimensions indicate a poor adsorption of the molecule onto the Au(111) surface. TM-AFM and STM imaging of the two cyt b_{562} variants bearing the thiol groups showed that their self-assembly was robust and upon immobilization their tertiary structure was retained. The proteins were also able to tolerate both electrical and mechanical stresses due to the probe scanning the sample. SH-SA and SH-LA mutated with two cysteines at different ends bound to Au(111) with different orientations. The similarity of the dimensions revealed by AFM and STM imaging to the size evaluated by X-ray structural analysis confirmed that the proteins were immobilized through the formation of a single thiol-Au bond.

A tunnelling decay factor β of (1.57 ± 0.25) $Å^{-1}$ was revealed for the cytochrome by investigating the relationship between the protein's height and the STM imaging current set-points. The measurement of a low beta-decay value demonstrates that the protein still retains good electron transfer capacity following adsorption onto a gold surface.

The single-molecule conductivity of cyt b_{562} engineered with pairs of thiol groups was also investigated using current-voltage and current-distance experiments. A strong and stable protein-gold interaction was achieved, and a single-molecule conductance of ~ 1 nS was measured for the double cysteine variants. In contrast, the unengineered wild-type cyt b_{562} bound much less robustly to the gold surface and the measured conductance was at least one order of magnitude less. The conductivity of the SH-SA variant was higher than the SH-LA probably due to the shorter distance between the Au electrodes and the iron center. Both the I-V_b and I-z experiments performed on the SH-LA molecules revealed two classes of conductance values. These results may be related to the different broadening of the molecular energy levels at each electrode due to the two possible orientations of the molecule in respect to the electrodes and to the different geometry of the STM tip and the Au(111) substrate.

Chapter 5

Electrochemical, EC-STM, I-V and I-z experiments of cyt b_{562} in buffer solution

The experiments described in Chapter 4 suggest that the tunnelling mechanism through the protein in air is off resonance. However, several reports have shown that redox protein's energy levels can be electrochemically aligned with the Fermi levels of the STM tip and the substrate [27, 137]. In this chapter a study of the electron transfer properties of the cyt b_{562} through a combination of electrochemistry, and STM, I-V_b and I-z methods in acqueous solution under electrochemical controls is reported.

5.1   Electrochemistry of metalloproteins

Since the late '70s, electrochemistry has emerged as the method of choice to study the relationship between the structure and the electron transfer properties of metalloproteins and enzymes. In fact, electrochemical methods can provide information about kinetics, stoichiometries and redox potential of the electron-transfer reaction between the adsorbate and the electrode [84, 85]. The central pathways for electron tunnelling within the protein structure can also be investigated by comparing the electron-transfer properties of proteins having mutations or deletions of their primary structure [56].

Electrochemical studies of metalloproteins have not just led to a deeper understanding of biological electron transfer processes as respiration, enzyme electrocatalysis and photosynthesis, but also to the development of biosensors and, in the last years, the birth of bio-nanoelectronics. Bare graphite, carbon glassy or metallic (platinum, gold) electrodes were used in the early electrochemical experiments and

proteins in solution were found to irreversibly adsorb on the solid surface in the electrochemical solution [46]. However, as most of the proteins denature during the chemisorption process due to interaction with a hard surface and do not retain their biological functions and redox activity, different immobilization techniques were soon developed.

One of the first routes to be explored was to generate biocompatible surfaces for protein adsorption [45]. Small organic molecules like alkanethiols and alkanedithiols [27], amino-terminated and carboxylate-terminated alkanethiols [99, 139], small peptides [14, 95], cysteine and its derivatives [71, 136] were and are still widely used to modify electrochemical electrodes by realizing self-assembled monolayers (SAMs). All these molecules have common features such as a group (*i.e.* thiolate) that interacts with the electrode surface and a second component that promotes the adsorption of the protein while preventing its denaturation and unstable binding to the metal electrode.

Even if much research has been directed towards tailoring noble metal surfaces for protein physical adsorption and very interesting results have been achieved, fast and direct electron transfer between the molecule and the substrate is the main challenge that has been addressed in the late electrochemical reports. The irreversible denaturation process that occurs when proteins are directly adsorbed onto bare metal surfaces can also be avoided by controlling the chemical interaction between the molecule and the electrode [56]. Particularly the thiol-gold interaction can be exploited to assemble organic molecules in a robust and well defined monolayer onto noble metal substrates. In recent years several research groups have used site-directed mutagenesis techniques to introduce thiol terminating cysteine groups at desired positions in the aminoacidic sequence of several proteins [9, 36, 37, 90]. Using this approach, the protein can be immobilized onto the gold surface in a controlled, well defined orientation.

The development of ultrasensitive tools such as *in-situ* EC-STM (Figure 5.1) and AFM has led to a dramatic improvement over the past decade in the spatial resolution for mapping molecules' structural and redox properties [107, 113]. For small model organic molecules and transition metal complexes, measurements of their charge transport have been achieved at the single-molecule level and several groups have shown that molecular conductance can be electrochemically gated [1, 2, 27, 101, 104, 117, 137]. The energy levels of a molecule located between two metallic substrates can be schematically represented as in Figure 5.2(a). The highest occupied molecular orbital (HOMO) and the lowest unoccupied molecular orbital (LUMO) localised electronic levels of the solvated molecule broaden due to

the interaction of the redox center with the electrodes and the electrolyte and, due to phonon-phonon coupling, the energy levels of the molecule fluctuate around their average position of a value equal to the reorganization energy λ. In an electrochemical environment, the Fermi levels of the two metallic electrodes E_s^F and E_t^F (*i.e.* STM substrate and tip) are separated by an energy equal to eV_b. The two Fermi energies can be shifted in parallel with respect to the reference electrode Fermi level by tuning the working (i.e. substrate) electrode potential (Figure 5.1).

Electrons tunnel from the tip to the substrate (or vice-versa depending on the applied V_b) independently on the relative position of the molecular levels with respect to the E_s^F and E_t^F (off-resonant current, Figure 5.2(a)). However the current through the junction can be enhanced if the energy levels of the molecule are aligned with the electrodes' Fermi level. When the Fermi level of one of the electrodes (*i.e.* tip in Figure 5.2(b)) is brought close to the LUMO energy and the molecular energy level decreases its energy due to reorganization energy fluctuations, electrons can transfer to the vacant orbitals of the molecule (I). At this stage three models have been proposed to explain the electron transfer mechanism across the second redox molecule-metal (*i.e.* substrate in in Figure 5.2(b)) junction [3]. (1) If the electron tunnels without molecular orbitals relaxations, the mechanism is referred to as resonant tunnelling [106]. (2) In case the molecule is weakly coupled to both the electrodes (diabatic limit), the reduced level has sufficient time to vibrationally relax to the E_s^F and cause the second electron transfer (complete vibrational relaxation [80]). The process is slower than the timescale of the LUMO energy fluctuations and the second electron transfer has no memory of the first process and there is no coherence between the two steps (noncoherent two-step electron transfer). (3) If the molecular redox center is strongly coupled with the electrodes (adiabatic limit), the electron can quickly transfer to the tip before the level relaxes completely (noncoherent two-step electron transfer with partial vibrational relaxation [134]). As the empty LUMO relaxes towards higher energies, another electron can tunnel from the negative electrode to the empty molecular orbitals. The electron transfer rate is much faster than in the diabatic limit and the cycle can be repeated several times before the LUMO relaxes to energy values higher than the electrode Fermi level. A number of electrons can tunnel between the two electrodes and the current can be strongly enhanced.

5.1.1 The coherent two-step electron transfer model

Considering a strong coupling between the metallic electrodes of the STM tip and the Au(111) substrate with the molecule, most of the experimental data presented
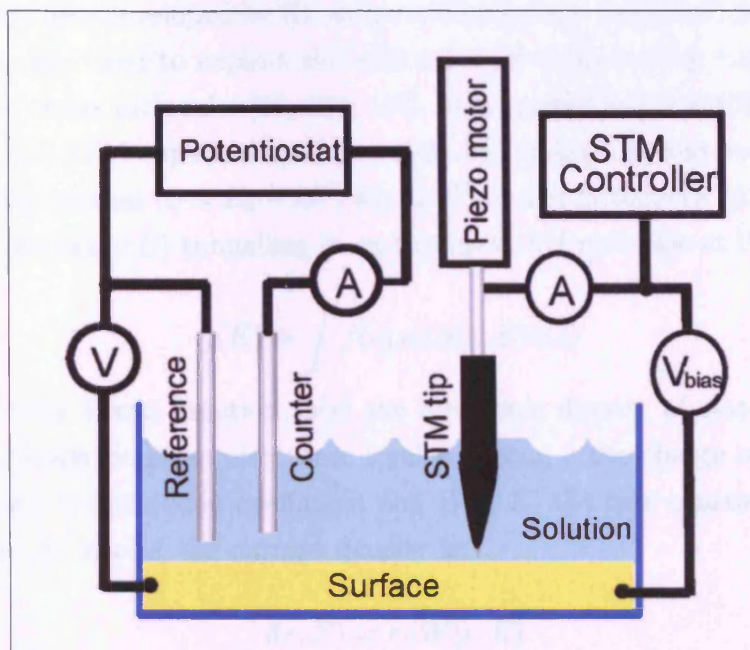
Figure 5.1: Schematic diagram of *in-situ* EC-STM showing (left) the potentiostat that controls the substrate working potential relative to a reference electrode and (right) the STM electronics that controls the bias applied between the tip and the substrate while measuring the tunnelling current (from [137]).
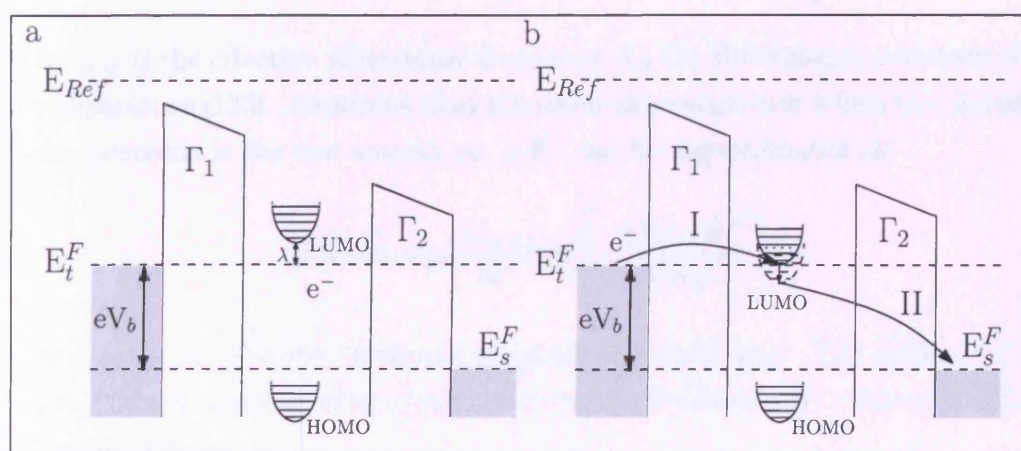
Figure 5.2: (a) Schematic electronic energy diagram of the two step electron transfer mechanism showing the reorganization energy λ needed for the LUMO to be aligned with the Fermi level of the left electrode. (b) An electron can tunnel from the left electrode to the LUMO when the molecular level is aligned with the Fermi energy level of the metal (I). After partial vibrational relaxation the electron can tunnel to the Fermi level of the right electrode (II).

in this thesis can be described by a coherent two-step electron transfer mechanism. The model was first developed by Kuznetsov, Ulstrup and collaborators (KU model) and is now widely used to explain the enhancement in tunnelling current observed in EC-STM of redox molecules [80, 134, 137]. It expresses the tunnelling current (I) measured in EC-STM experiments as function of the applied bias voltage (V_b) and substrate overpotential ($\eta = E_s - E^{0'}$, where $E^{0'}$ is the molecule's redox potential). The current density $j(E)$ tunnelling from the tip to the molecule at the potential E is:

$$j(E) = \int f(\epsilon)\rho(\epsilon)i(\epsilon, E)d(\epsilon) \tag{5.1}$$

where $f(\epsilon)$ is the Fermi function, $\rho(\epsilon)$ the electronic density of states, and $i(\epsilon, E)$ the current density from an electronic level ϵ. Being e the charge of the electron, κ the electronic transmission coefficient and $W(\epsilon, E)$ the rate constant for electron transfer from the level ϵ, the current density is:

$$i(\epsilon, E) = e\kappa W(\epsilon, E) \tag{5.2}$$

The function $W(\epsilon, E)$ depends on the energy of the electronic transition from the Fermi level of the metal to the molecule (or from the molecule to the metal) and can be written as:

$$W(\epsilon, E) = \frac{\omega_{eff}}{2\pi}exp\left\{-\frac{[\lambda + eE - (\epsilon - \epsilon_F)]^2}{4\lambda k_B T}\right\} \tag{5.3}$$

where ω_{eff} is the effective vibrational frequency, k_B the Boltzmann's constant and T the temperature [133]. Assuming that the electronic range over which the tunnelling process proceeds is the one around ϵ_F, $j(E)$ can be approximated as:

$$j(E) \approx e\kappa_{eff}\frac{\omega_{eff}}{2\pi}exp\left[-\frac{(\lambda + eE)^2}{4\lambda k_B T}\right] \tag{5.4}$$

where κ_{eff} is the effective electronic transmission coefficient. The number of electrons n, that are transferred in a single transfer process before the reduced or oxidised level is trapped, is:

$$n \approx \frac{eV_b}{\Delta\epsilon} \tag{5.5}$$

where eV_b is the bias applied between the tip and the substrate, and $\Delta\epsilon = 1/(\kappa\rho)$ with κ being the effective electronic transmission coefficient between the electrode and the molecule and ρ the density of states around the Fermi level of the tip or the substrate depending on the considered electron transfer [134]. Equation (5.4) can

be then rewritten in terms of current I:

$$I(E, V_b) = e\kappa\rho(eV_b)\frac{\omega_{eff}}{2\pi}exp\left[-\frac{(\lambda + eE)^2}{4\lambda k_B T}\right] \tag{5.6}$$

Considering the two step electron process described in Figure 5.2, the total current tunnelling between the substrate to the tip can be approximated in the low bias and overpotential regime by the following equation:

$$\frac{1}{I} = \frac{1}{I_S} + \frac{1}{I_T} \tag{5.7}$$

where I_T and I_S are the currents from the tip to the molecule and from the molecule to the substrate, respectively.

$$I_T(\eta, V_b) = e\kappa_S\rho_S(eV_b)\frac{\omega_{eff}}{2\pi}exp\left[-\frac{(\lambda + e\xi\eta + e\gamma\,|V_b|)^2}{4\lambda k_B T}\right] \tag{5.8}$$

$$I_S(\eta, V_b) = e\kappa_T\rho_T(eV_b)\frac{\omega_{eff}}{2\pi}exp\left[-\frac{(\lambda - e\xi\eta - e\gamma\,|V_b| + e\,|V_b|)^2}{4\lambda k_B T}\right] \tag{5.9}$$

Here $\xi\eta$ and γV_b indicate the effective electrode potentials applied to the molecular reactive center due to the overpotential η and the bias voltage V_b. Assuming that:

1. the second electron transfer proceeds in the fully adiabatic limit($\kappa = 1$);

2. the two electrodes have a similar density of states near the Fermi level ρ;

the expression for the current (5.7) can be transformed to:

$$I(\eta, V_b) = e\kappa\rho(eV_b)\frac{\omega_{eff}}{2\pi}\left\{exp\left[-\frac{(\lambda + e\xi\eta + e\gamma\,|V_b|)^2}{4\lambda k_B T}\right]\right.$$
$$\left. + exp\left[-\frac{(\lambda - e\xi\eta - e\gamma\,|V_b| + e\,|V_b|)^2}{4\lambda k_B T}\right]\right\}^{-1} \tag{5.10}$$

As it will be shown in section 5.3.2, the KU model describes quantitatively the STM and I-V_b experimental data recorded in liquid under electrostatic control. The other two models describing the two electron transfer process were also taken into account for interpreting my experimental results. However, the resonant tunnelling mechanism predicts a maximum in the enhanced tunnelling current at an overpotential corresponding to the reorganization energy (that has typical values ranging

between 0.1 eV and 0.5 eV [27]) and I measured the maximum values of tunnelling current both in the EC-STM imaging and in the I-V_b measurements of the cyt b_{562} at overpotential values close to 0 V (section 5.3.3.1). In the diabatic limit a very small enhancement of the current at $\eta = 0$ is predicted, while the data recorded for the double cysteine mutant proteins at $\eta = 0$ show a conductivity two orders of magnitude higher than the ones with the system off-resonance.

In order to fully characterize the electron transfer properties of the cyt b_{562}, the single and double cysteine mutants proteins were adsorbed on bare Au(111) substrates and their redox properties investigated by various electrochemical means. To compare the engineered proteins and the wild-type protein's redox properties, the non-mutated protein was adsorbed on Au(111) electrodes modified with amino-terminated alkanethiols and electrochemical measurements were performed. The D50C single cysteine mutants reconstructed with Zn-PP and Cu-PP was also adsorbed on pristine Au(111) electrodes and investigated by cyclic voltammetry to study how the iron center affects the electron transfer mechanism of cyt b_{562}. Electrochemical gating of the D50C, SH-SA and SH-LA cysteine mutants was investigated at a single molecule level by using three different STM techniques, namely imaging, I-V_b and I-z measurements.

5.2 Experimental section

5.2.1 Preparation of protein monolayers

Au(111) bead single crystals electrodes used in both electrochemical and STM experiments were home-made from polycrystalline gold wires (99.99% in purity, Goodfellow) by using a method described by Clavilier et al. [32]. The quality of the electrodes was checked by voltammetry and electrochemical STM imaging (Figure 5.3). The Au(111) electrodes were electropolished in 1 M H_2SO_4 and washed with 0.1 M HCl and water, then annealed for 8 hours at 880 °C [32, 70]. Prior the protein deposition the electrodes were annealed with a H_2 flame and the Au(111) single crystal surface was protected with hydrogen saturated water. The electrodes were subsequently incubated in 20-50 μM protein solution at 4 °C overnight. Prior the experiments the electrodes were rinsed with deionized water in order to remove the non-chemically adsorbed molecules. The proteins were checked for stability measuring the UV-Vis spectra before and after the incubation.

For the electrochemical studies of the wild-type protein deposited on modified electrode, the Au(111) crystals were fist incubated for 24 hours at room temperature in ethanol (99.99%, Sigma-Aldrich) containing 1 mM amino-terminated alkanethi-
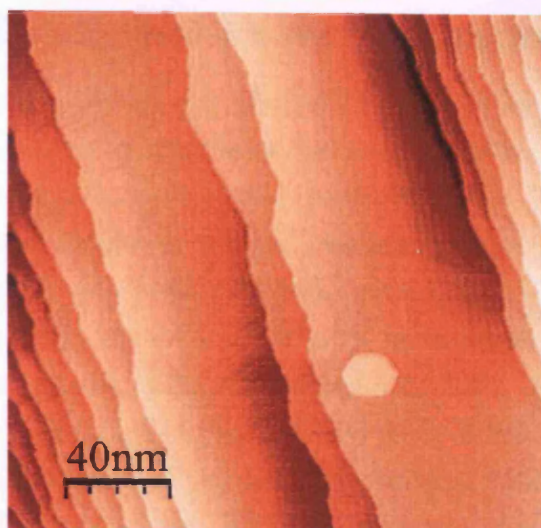
Figure 5.3: EC-STM image of Au(111) surfaces obtained under electrochemical environments (10 mM phosphate buffer, pH 6.2). Working electrode potential -0.10 V vs SCE, tunnelling current 35 pA, bias voltage -0.4 V.

ols ($NH_2(CH_2)_nSH$ with $n = 2, 6, 11$), then rinsed in ethanol to remove physically adsorbed molecules, washed in deionized water and incubated overnight in 50 μM protein solution at 4 °C. Cysteamine (NH_2-C2), 6-amino-1-hexanethiol hydrochloride (NH_2-C6) and 11-amino-1-undecanethiol hydrochloride (NH_2-C11) were all purchased from Dojindo Molecular Technologies and used without further purification.

5.2.2   Electrochemical measurements

All measurements were carried out using an Autolab system (Eco Chemie, Netherlands) controlled by a general purpose electrochemical system software at room temperature (23 ± 2 °C). A three-electrode system, consisting of a platinum coiled wire as counter electrode (CE), a freshly-prepared reversible hydrogen electrode (RHE) as reference electrode (RE) and a Au(111)-based working electrode (WE), was used with the WE in a hanging-meniscus configuration. The RHE was checked against a saturated calomel electrode (SCE) after each measurement. All electrode potentials are reported vs SCE. Purified argon (Chrompack, 5 N) was applied to purge dioxygen from electrolyte solutions before the measurements, and the gas stream maintained over the solution during the measurements. The sample was allowed to equilibrate in the phosphate buffer (PB) solution for 5 minutes. The buffer used was the same as the one to store the proteins (10 mM PB pH 6.2). Scanning rates were in the range 0.05 V/s - 100 V/s, depending on the analyzed protein monolayer, and the potential window was from -0.3 V to + 0.2 V vs SCE. All glassware was boiled in nitric acid solution (20%) and washed with deionized water prior the experiments.

5.2.3 EC-STM, I-V_b and I-z measurements

STM measurements were performed using a PicoSPM system (Molecular Imaging Co., USA) equipped with a bipotentiostat for potential control of both the substrate and the tip. Electrochemical control was conducted in a home-designed cell with a three-electrode system similar to normal electrochemical measurements. Counter and reference electrodes were both platinum wire gauze. The reference potential was measured versus SCE in the end of each experiment. All the experiments were carried out in a special designed Argon chamber. The tips were prepared from tungsten or/and Platinum/Iridium (90%-10%) wires (0.25 mm in diameter) by electrochemical etching and insulated with Apiezon wax to eliminate or reduce Faradaic currents to 5 pA or better. STM imaging was carried out in the constant-current mode under an Argon atmosphere. The STM scanner was calibrated by using the Au(111) reconstrution lines (Figure 5.3).

Before starting the I-V_b and I-z experiments, the substrate was imaged and the tip checked for integrity. After achieving molecular resolution and when the system lateral drift was as low as few pm/s, the STM tip was placed on top of a single molecule at a current set-point of 35 pA and a voltage bias of -100 mV. In the I-V_b experiments, the STM feedback loop was disengaged and the bias voltage ramped within the range ±0.2 V in 0.1 second (400 steps). After each measurement the feedback was turned on and the current voltage amplifier allowed to stabilize for 100 μs before recording another I-V_b characteristic. The substrate potential was changed over a range of 0.7 V in 50 mV steps and at least one hundred I-V_b characteristics were recorded for each potential. The sample was imaged after varying the working potential in order to check for protein stability and drift. In the I-z experiments the tip was linearly moved towards the sample in order to realize mechanical contact with the protein. The tip was then moved out of contact and the current measured as function of tip travelled distance (driving rate 40 nm/s). The working electrode potential was changed so that the proteins were in the fully reduced, at the equilibrium redox potential and in the fully oxidised state. Five hundred I-z traces were recorded at each overpotential and, before varying the working potential, the sample was imaged to check for protein stability and system lateral drift.

5.2.4 Data Analysis

Autolab software was used to analyze electrochemical data. In situ STM images were post-processed (flattening) and analyzed using WSxM software. I-V_b and I-z data were analyzed using OriginPro 8.0. In order to analyze the I-z curves and

obtain the conductance histograms, the raw selected data were divided by the bias voltage and converted to histograms using 1 bin/nS.

5.3 Results and discussion

5.3.1 Long-range interfacial ET revealed by electrochemistry

5.3.1.1 Apo- and holo-wild-type and cysteine mutants cyt b_{562} adsorbed on bare Au(111)

Reproducible and stable electrochemical signals were achieved for holo-D50C, holo-SH-SA and holo-SH-LA cysteine mutants deposited on single crystal Au(111). Figure 5.4 displays the cyclic staircase voltammetry response of the Au electrode in a buffer solution following apo- and holo-cyt b_{562} cysteine mutants adsorption. The voltammograms of the holo-proteins present almost symmetrical oxidation and reduction waves of similar magnitude pointing out that the redox molecules undergo a facile-chemically reversible electron transfer reaction at gold electrodes. The cathodic and anodic peaks are associated to the haem redox centre of cyt b_{562}, according to the relation:

$$Cyt\,b_{562}(Fe^{2+})_{ads} \rightleftharpoons Cyt\,b_{562}(Fe^{3+})_{ads} + e^- \tag{5.11}$$
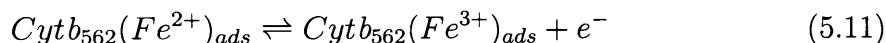
No Faradaic response was observed in any of the cyclic voltammetry control measurements performed with apo-D50C, apo-SH-SA and apo-SH-LA cyt b_{562} (Figure 5.4). It was noted that the capacitive background current of holo-protein monolayers was significantly larger than that for apo-protein monolayers. This is most likely attributed to structural differences between apo- and holo-cyt b_{562} (Figure 2.1). The apo-cyt b_{562} is partially folded and is much less ordered. The hydrophobic patches in the polypeptide could thus be exposed partially to the electrolyte solution to increase surface hydrophobicity of the apo-protein monolayers (i.e. decrease system capacitance). As already shown in previous reports [27, 31], hydrophobic molecules can cause a decrease in capacitance due to the low dielectric constant at the electrode/electrolyte interface.

Cyclic voltammetric experiments were also performed with the holo-wild-type cyt b_{562} adsorbed on bare Au(111) electrodes in order to examine the role of the introduced cysteine (Figure 5.5). No redox signal was observed for the protein even at very low scan rates (10 mVs^{-1}). This result can be explained considering the
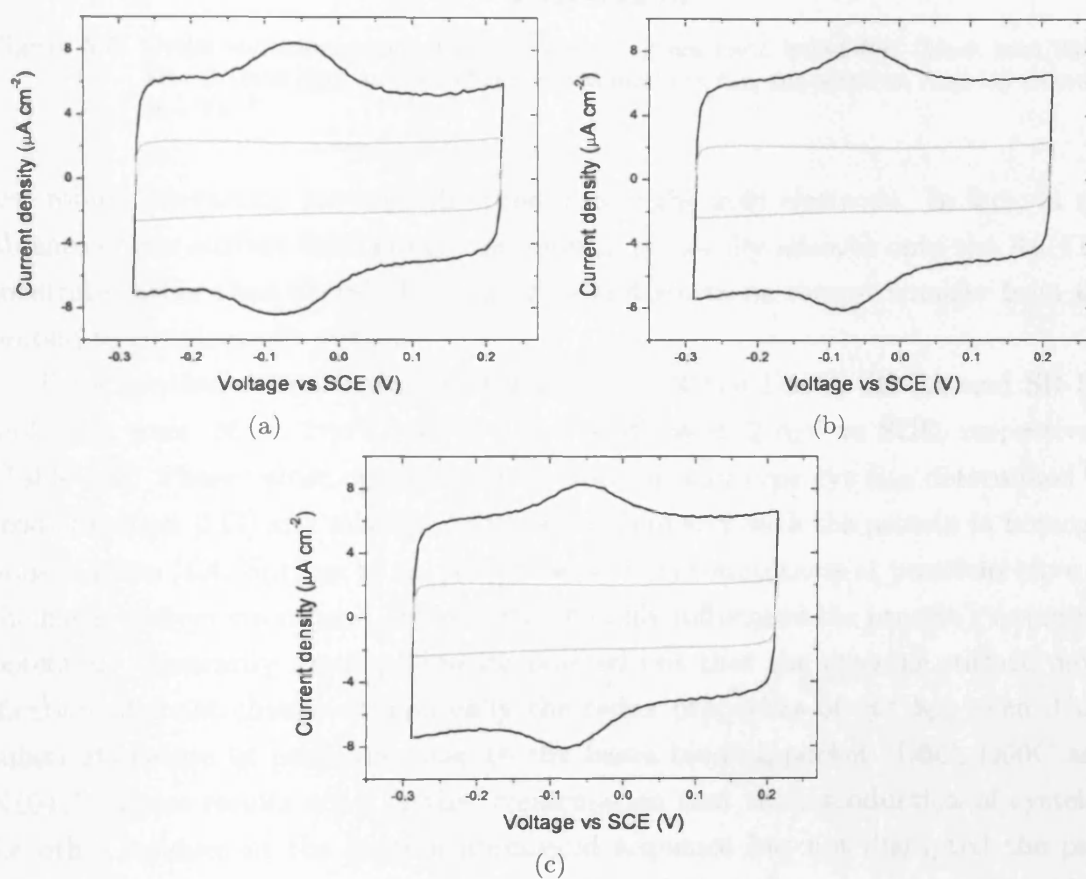
Figure 5.4: Cyclic voltammograms of apo- (gray line) and holo- (black line) (a) D50C, (b) SH-SA and (c) SH-LA molecules deposited on Au(111) recorded at 1 Vs^{-1}.
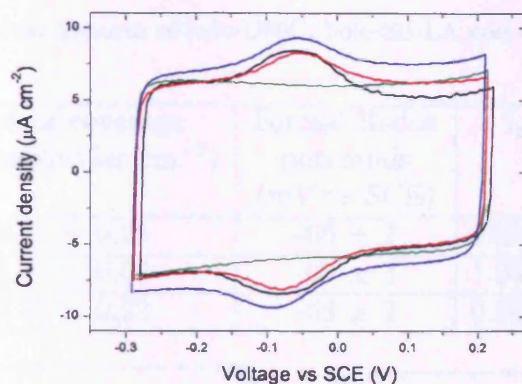
Figure 5.5: Cyclic voltammograms of holo-wild-type (green line), holo-D50C (black line), holo-SH-SA (blue line) and holo-SH-LA (red line) cyt b_{562} deposited on Au(111) recorded at 1 Vs^{-1}.

less robust interaction between the protein and the gold electrode. In fact, in the absence of any surface thiol group, the protein physically adsorbs onto the Au(111) substrate rather than chemically bind to it and electrons cannot transfer from the protein to the electrode surface.

The evaluated formal redox potentials ($E^{0'}$) of the D50C, SH-SA and SH-LA molecules were -66 ± 2 mV, -69 ± 3 mV and -68 ± 2 mV vs SCE, respectively (Table 5.1). These values agree well with that for wild-type cyt b_{562} determined by redox titration [111] and measured by electrochemistry with the protein in homogenous solution [13]. Springs et al. [112] observed that mutations at positions close to the haem microenvironment (R98, R106) strongly influenced the protein's reduction potential. Contrarily my experiments pointed out that the cysteine surface modifications did not change dramatically the redox properties of cyt b_{562} even if the substitutions are at positions close to the haem binding pocket (D5C, D50C and K104C). These results are a further confirmation that the introduction of cysteine for other residues in the protein aminoacid sequence has not disrupted the protein tertiary configuration and that the molecules adsorption onto bare gold surface occurs without functional perturbation of their natural structure.

The midpoint redox potential of the cyt b_{562} cysteine mutants was also investigated in buffers with different pH (pH range = 6.0-7.2). The results from the experiments reveal that the solution pH has little effect on the redox potential of the molecule in disagreement with Baker's results [13] that reported a change in the protein's redox potential from 220 mV vs SHE at pH = 6.0 to 180 mV vs SHE at pH = 7.0 for the wild-type cyt b_{562} adsorbed onto graphite surfaces modified with the hexapeptide KCTCCA. However, the different experimental conditions could explain the discrepancy in the results.

The observed linear relationship between the redox peak currents and scan rates

Table 5.1: Electron transfer features of holo-D50C, holo-SH-LA and holo-SH-SA monolayers on Au(111).

Protein monolayer	Surface coverage $(10^{12}$ molecules $cm^{-2})$	Formal Redox potentials (mV vs SCE)	I_{pa}/I_{pc}	Electron transfer rate constant (s^{-1})
Holo-D50C	6.43 ± 0.25	-66 ± 2	1.02 ± 0.06	44.0 ± 5.2
Holo-SH-SA	5.71 ± 0.06	-69 ± 3	1.05 ± 0.06	61.8 ± 2.2
Holo-SH-LA	6.26 ± 0.22	-68 ± 2	0.94 ± 0.08	40.8 ± 7.2
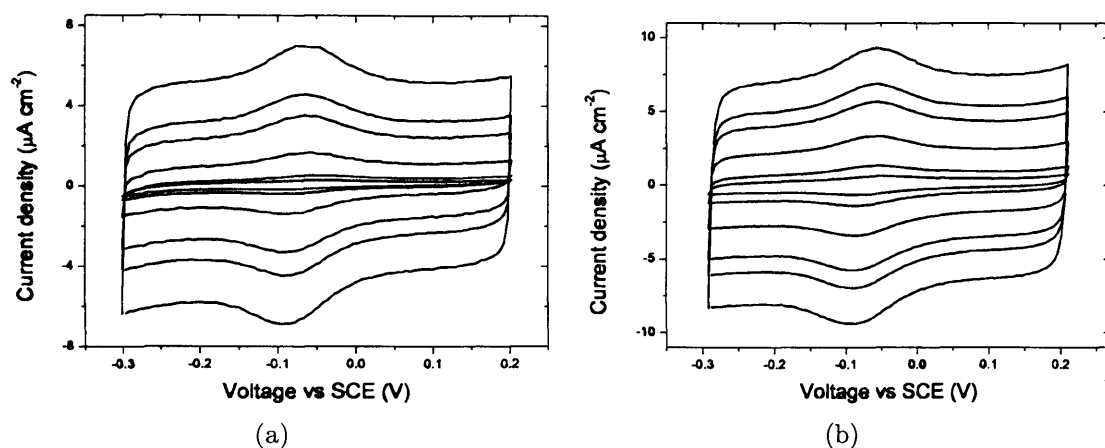
Figure 5.6: Cyclic voltammetry of (a) holo-SH-SA/Au(111) and (b) holo-SH-LA/Au(111) in 10 mM phosphate buffer (pH 6.2) at various scan rates $(0.2, 0.3, 0.5, 0.7, 0.8, 1.0 \text{ Vs}^{-1})$

(Figure 5.6 and 5.7) is a clear indication of a diffusionless electrochemical electron transfer reaction and supports the fact that the redox active proteins are confined to the electrode surface. Hypothesizing that the cyt b_{562} cysteine mutants adsorb on the gold surface through a single thiol bonding (section 4.3.1), the estimated surface coverage of electroactive protein on the gold surface was (6.43 ± 0.25) x 10^{12}, (5.71 ± 0.06) x 10^{12} and (6.26 ± 0.22) x 10^{12} molecules per cm^2 for D50C, SH-SA and SH-LA, respectively (Table 5.1). These values correspond to a submonolayer coverage ($\sim 10\%$ of the gold surface depending on the molecular dimensions of the proteins) and are in agreement with the STM images showing disperse proteins on the Au(111) electrodes (section 5.3.2). The low protein density was required in order to measure the electronic properties of single cytochrome molecules. However a higher surface coverage could be obtained by using a different method to adsorb proteins onto the electrode rather than simple electrode incubation with the proteins solution (i.e. electro mediated adsorption).

The well defined cyclic voltammograms are perfectly symmetric at low scan rate and they become more and more asymmetrical as the scan rate increases (Figure 5.8). In particular the separation of anodic and cathodic potentials observed for the
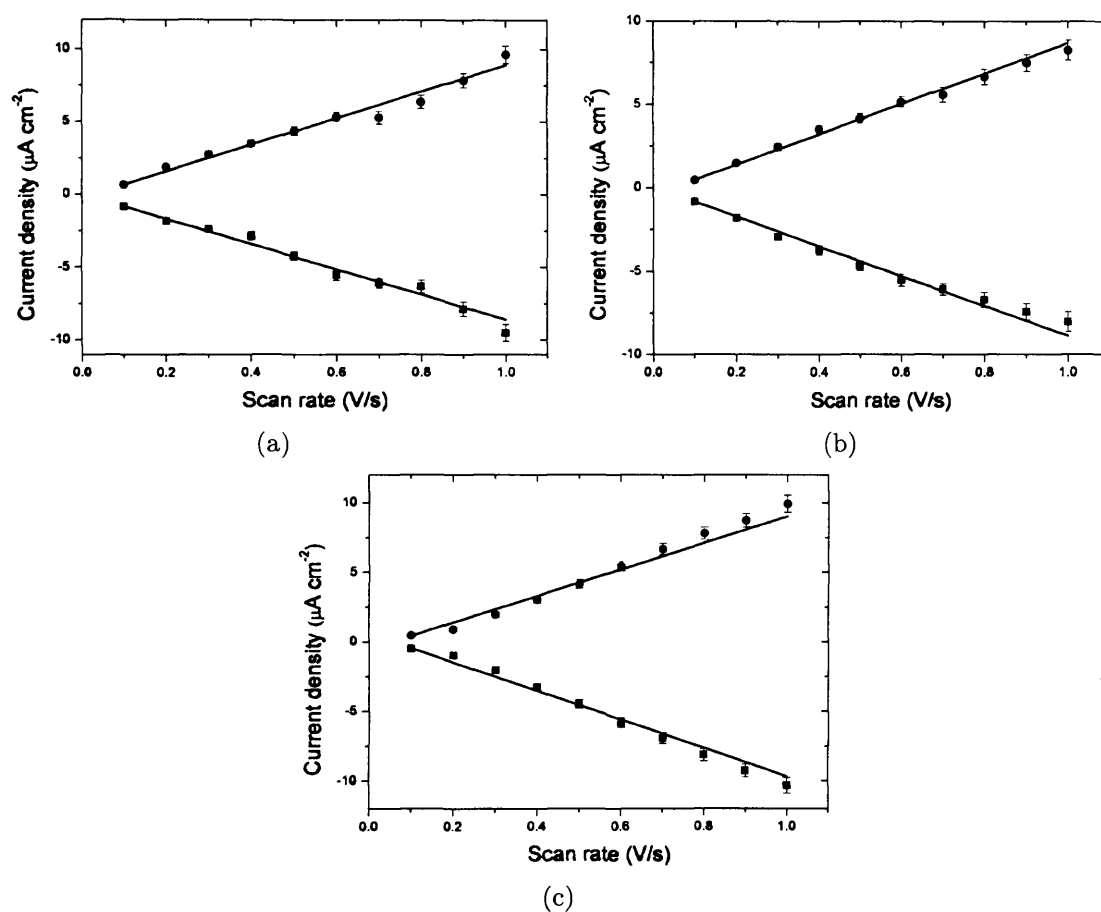
Figure 5.7: Relation between the the anodic (circle dots) and cathodic (square dots) peak currents and scan rates for (a) holo-D50C, (b) holo-SH-SA and (c) holo-SH-LA. The solid lines are linear fit of the experimental data.

cysteine mutant monolayers increases with the sweep rate indicating that the studied electrochemical system is quasi-reversible. If we hypothesize that the examined proteins strongly adsorb onto the electrode surface and that the electrochemical reaction is entirely confined to the adsorbed molecules, the electron transfer rate constant for the proteins can be obtained from the cyclic voltammetry measurements using a method developed by Laviron [84, 85].

According to Laviron, the rate transfer constant and the transfer coefficient of an electrochemical reaction involving molecules strongly adsorbed onto the electroactive surface can be determined studying the relation between the difference in peak potential and the scan rate. In particular if the oxidation reduction reaction concerns exclusively the adsorbed molecules (diffusionless system) the peak separation between anodic and cathodic potentials (ΔE_P) should increase with increasing sweep rate and electron transfer rate constant (k_s). If the ΔE_P values are smaller than $200/n$ mV (with n being the number of electrons transferred in the redox reaction) k_s can be evaluated using the equation:

$$m = (RT/F)(k_s/nv) \qquad (5.12)$$

where R is the gas constant (8.314 J mol^{-1} K^{-1}), T is the absolute temperature (K), F is the Faraday constant (96485 C mol^{-1}), v is the scan rate (Vs^{-1}) and m is a parameter related to the peak separation that can be evaluated from a plot shown in Laviron's paper [85].

Considering that only one electron is transferred in the redox reaction of cyt b_{562} (equation (5.11)), the proteins' electron transfer rate constant can be calculated precisely using the Laviron's equation (5.12) (Figure 5.9(a)) which gives a value of 44.0 ± 5.2 s^{-1}, 61.8 ± 2.2 s^{-1} and 40.8 ± 7.2 s^{-1} for D50C, SH-SA and SH-LA, respectively (Table 5.1). The figures are rather high considering the electron transfer distance and indicative of an efficient pathway between the redox center and the bare gold electrode surface. These results support the idea that a simple cysteine mutation onto the protein surface can well replace the need of biocompatible electrodes.

Reductive desorption of the cyt b_{562} cysteine mutants/Au(111) and of the wild-type cyt b_{562}/Au(111) in 10 mM PB pH 6.2 solutions was also performed (Figure 5.9(b)). The linear sweep voltammetry experiments showed two reductive desorption peaks for the cyt b_{562} cysteine mutants from the Au(111) surface and only one for the wild-type cyt b_{562} in the first scan. The peaks gradually disappeared in the following scans. The observed reductive desorption peaks are very close to the one reported for cysteine adsorbed on Au(111) (-0.700 ± 0.015 V vs SCE) [135],
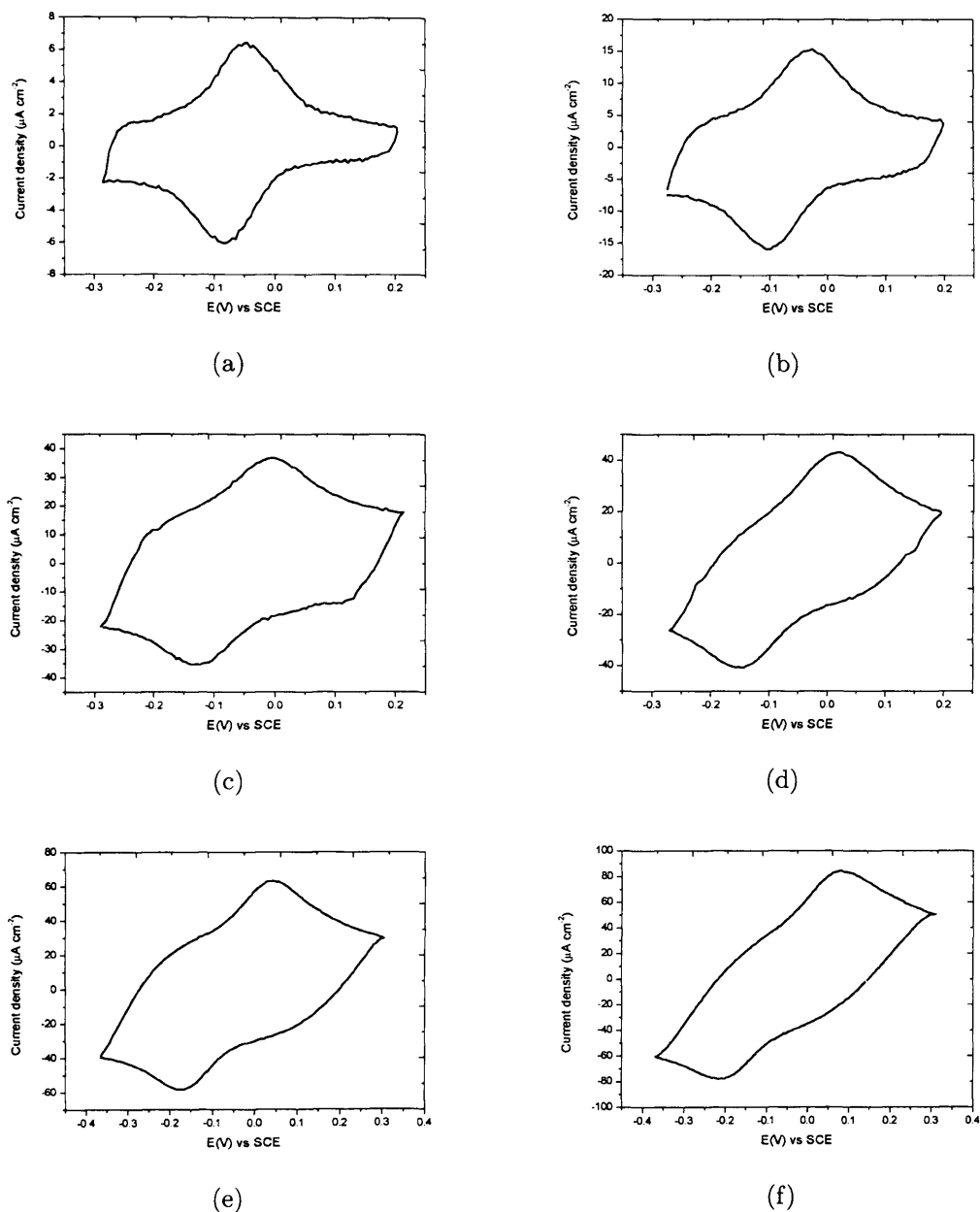
Figure 5.8: Cyclic voltammograms of cyt b_{562} SH-LA-Au(111) in 10 mM phosphate buffer (pH 6.2) at various scan rates (a) 2, (b) 5, (c) 10, (d) 15, (e) 20 and (f) 30 Vs^{-1}.
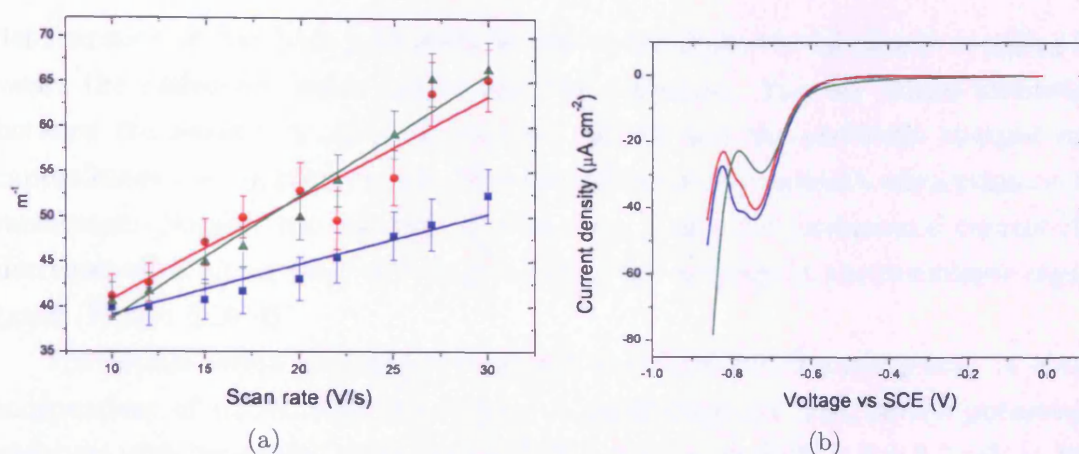
Figure 5.9: (a) Plot of m^{-1} versus scan rate for (green) holo-D50C, (blue) holo-SH-SA and (red) holo-SH-LA. The m values were obtained from the peak separations in the cyclic voltammograms. The electron transfer rate constants are estimated from the slope of the curves fitting the data according to equation (5.12) (solid lines). (b) Linear sweep voltammograms of reductive desorption of of holo-wild-type (green line), holo-SH-SA (blue line) and holo-SH-LA (red line) cyt b_{562} from Au(111) surfaces in 10 mM phosphate buffer (pH 6.2). Scan rate 10 mVs^{-1}.

suggesting that the S–Au bonding was disrupted in the experiments. As the energy required for breaking the sulphur-Au(111) bonding depends on the size of the linked molecule, the two reductive peaks observed for the cyt b_{562} cysteine mutants can be attributed to the DTT molecules desorption (peak at -0.72 ± 0.01 V vs SCE) and to the proteins desorption (peak at -0.79 ± 0.01 V vs SCE). The single reductive peak observed for the wild-type cyt b_{562} indicates that just one kind of molecule (DTT) is covalently bound to the Au(111) surface.

5.3.1.2   Wild-type cyt b_{562} deposited on amino-alkanethiols modified Au(111) crystals

In order to fully characterize the electron transfer properties of the cyt b_{562}, cyclic voltammetry experiments of the wild-type protein assembled on Au(111) substrates modified with amino-terminated alkanethiols monolayers were performed. The amino-terminated alkanethiols have a hydrophobic alkyl chain and a polar tail group and their monolayer can mimic the biological membrane, a natural interface for the cytochrome.

Figure 5.10 shows examples of cyclic voltammograms recorded for the holo-wild-type/NH$_2$(CH$_2$)$_n$SH Au(111) electrodes ($n = 2, 6, 11$). Well defined redox peaks indicate a fast and reversible electron transfer between the protein adsorbed on the SAM and the substrate. The amino-terminated mercaptoalkanes monolayers seem not only to be responsible for the proteins immobilization and for preventing their

denaturation at the bare gold surface, but to facilitate the electronic coupling between the molecules' redox center and the substrate. Van der Waals interaction between the negatively charged protein's surface and the positively charged mercaptoalkanes ending group might be responsible for the protein's adsorption on the membrane. Notably the voltammograms show a very low background current that decreases with increasing SAM length due to the decrease in the monolayer capacitance (Figure 5.10(d)).

The formal redox potential, estimated from cyclic voltammograms, is almost independent of the linking molecules. A small negative shift of the potential is observed with increasing chain length (2.8 ± 2.7 mV vs SCE, 1.8 ± 1.7 mV vs SCE and -16.4 ± 2.1 mV vs SCE for the holo-wild-type/NH$_2$-C2, holo-wild-type/NH$_2$-C6 and holo-wild-type/NH$_2$-C11, respectively). These values are very close to the ones recently reported for the wild-type cyt b_{562} deposited on silver electrodes modified with amino-terminated alkanethiols [139], on hydrophobic surfaces [13, 92] and on Au(111) surfaces modified with a cationic hexapeptide (KCTCCA) monolayer [95].

The linear increase of the redox peak current with the scan rate (Figure 5.11(a)) indicates that the electrochemical electron transfer reaction occurs at the electrode surface with an estimate electroactive protein surface coverage of $(3.7 \pm 0.2) \times 10^{12}$, $(3.5 \pm 0.2) \times 10^{12}$ and $(4.4 \pm 0.3) \times 10^{12}$ molecules per cm^2 on the NH$_2$-C2, NH$_2$-C6 and NH$_2$-C11 monolayers on Au(111), respectively.

The system is stable and robust enough to acquire cyclic voltammograms at high scan rates (≥ 50 Vs^{-1}). The peak divergence increases with the length of the mercaptoalkanes chain length in agreement with the data reported for the azurin molecule adsorbed on Au(111) electrodes modified with alkanethiols SAM [27]. The separation of the redox peaks increases with the sweep rates (Figure 5.11(b)) indicating that the studied systems are quasi-reversible and the values of the electron transfer rate constants calculated by using Laviron's equation (5.12) are 78 ± 8 s^{-1}, 63 ± 7 s^{-1} and 20 ± 3 s^{-1} for the wild-type protein adsorbed on Au(111) electrodes modified with NH$_2$-C2, NH$_2$-C6, NH$_2$-C11 SAMs, respectively. The evaluated electron rate constants are of the same order of magnitude than the ones calculated for the cysteine mutants proteins adsorbed on bare Au(111). The major implication of this result is that the thiol moieties inserted in the cysteine mutants are as efficient as a biomimetic surface in realizing electronic pathways between the protein's redox center and the bare gold electrode surface.
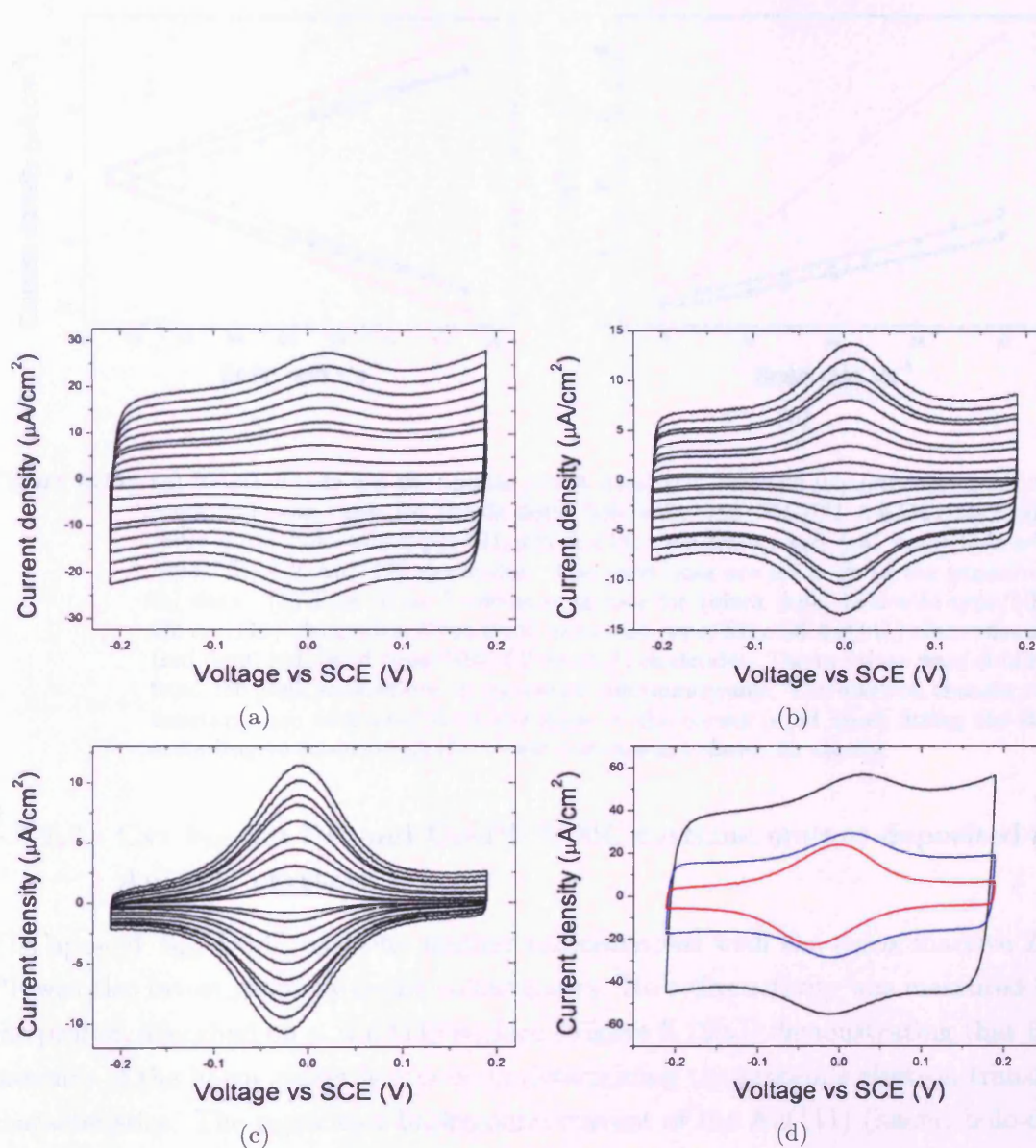
Figure 5.10: Cyclic voltammograms of (a) holo-wild-type/NH$_2$-C2 Au(111) electrodes, (b) holo-wild-type/NH$_2$-C6 Au(111) electrodes and (c) holo-wild-type/NH$_2$-C2 Au(111) electrodes recorded in 10 mM PB pH 6.2 at different scan rates (0.1 Vs^{-1} - 1.0 Vs^{-1}, the higher is the scan rate, the higher is the current density). (d) Cyclic voltammograms of holo-wild-type/NH$_2$(CH$_2$)$_n$SH Au(111) electrodes (n = (black curve) 2, (blue curve) 6, (red curve) 11) recorded at 1 Vs^{-1}.

(a)   (b)
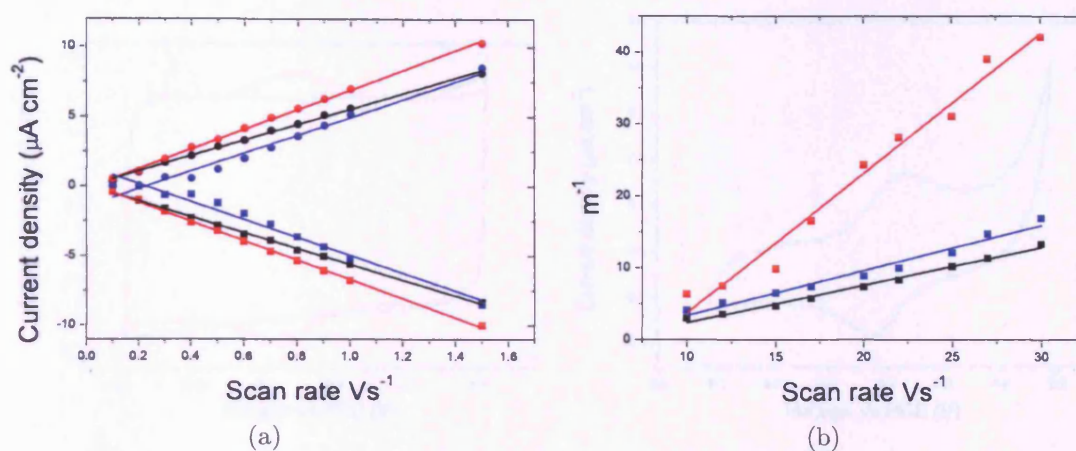
Figure 5.11: (a) Relation between the anodic (circle dots) and cathodic (square dots) peak currents and scan rates for (black dots) holo-wild-type/NH$_2$-C2 Au(111) electrodes, (blue dots) holo-wild-type/NH$_2$-C6 Au(111) electrodes and (red dots) holo-wild-type/NH$_2$-C2 Au(111) electrodes. The solid lines are linear fit of the experimental data. (b) Plot of m^{-1} versus scan rate for (black dots) holo-wild-type/NH$_2$-C2 Au(111) electrodes, (blue dots) holo-wild-type/NH$_2$-C6 Au(111) electrodes and (red dots) holo-wild-type/NH$_2$-C2 Au(111) electrodes. The m values were obtained from the peak separations in the cyclic voltammograms. The electron transfer rate constants are estimated from the slope of the curves (solid lines) fitting the data according to equation (5.12). Error bars are not shown for clarity.

5.3.1.3   Cyt b_{562} Zn-PP and Cu-PP D50C cysteine mutant deposited on Au(111) crystals

The apo-cyt b_{562} D50C cysteine mutant reconstructed with the redox inactive Zn-PP was also investigated by cyclic voltammetry. No redox activity was measured for the protein adsorbed on a Au(111) surface (Figure 5.12(a)) demonstrating that the presence of the haem center is crucial in determining the protein's electron transfer characteristics. The capacitive background current of the Au(111)-(haem)-holo-cyt b_{562} and the Au(111)-Zn-PP-cyt b_{562} systems are very similar indicating that the protein's hydrophobic residues are not exposed to the supporting electrolyte. This result, in conjunction with the measured UV-Vis spectra (section 2.5.3) supports the idea that the cytochrome maintains its folded tertiary structure when reconstructed with metal protoporphyrins different from the haem.

The Cu-PP-mutant D50C electrochemistry at gold surface was characterised by a stable and reversible response. Direct electron transfer was consistently detected by normal cyclic voltammetry, indicating that electronic coupling between the Cu-PP center and the electrode is quite effective. Figure 5.12(b) shows an example of the reversible cyclic voltammogram recorded for this system. A pair of well-defined redox peaks was observed with an equilibrium potential of 205 ± 5 mV vs SCE. Cathodic and anodic peaks are not symmetric, suggesting that the protein does not
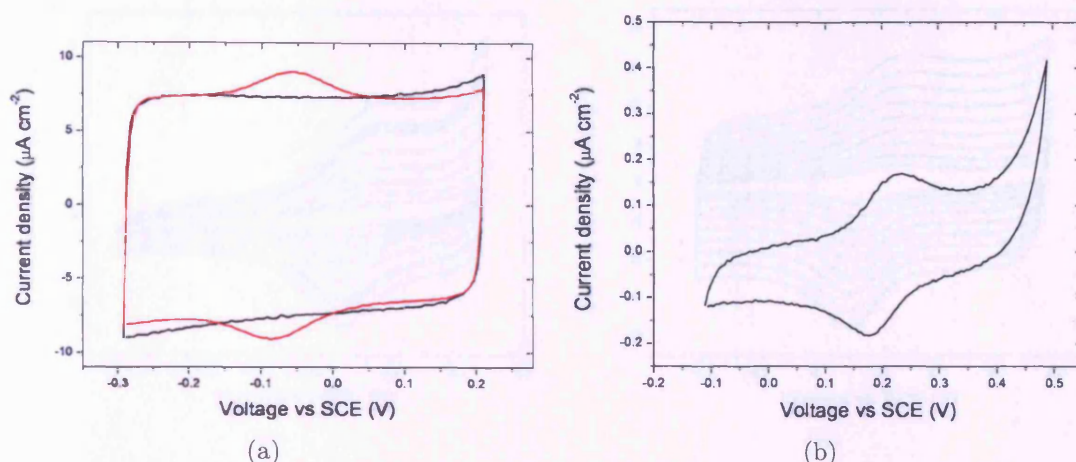
Figure 5.12: (a) Cyclic voltammograms recorded for cyt b_{562} D50C reconstructed with haem (black line) and Zn-PP (red line) adsorbed on Au(111) in 10 mM phosphate buffer pH 6.2. Scan rate is 1 Vs^{-1}. (b) Cyclic voltammetry of D50C cysteine mutants reconstructed with Cu-PP and deposited on Au(111) in 10 mM phosphate buffer pH 6.2 at 20 mVs^{-1}.

retain its original conformation upon copper oxidation or that the co-ordination of the Cu-PP with the protein's active site changes upon its oxidation.

The cathodic and anodic peaks are different from the ones determined for the Cu-PP in homogeneous solution (Figure 5.13). The calculated $E^{0\prime}$ value for the Cu-PP is -50 ± 2 mV vs SCE and the cytochrome might be then viewed as a facilitator of electron transfer between the redox center and the electrode. The difference of the redox potentials and the shift of the Cu-PP absorbance spectra peaks in presence of the cyt b_{562} (section 2.5.3) confirm that the Cu-PP co-ordinate to the D50C molecule.

The cathodic and anodic peak currents of the cyclic voltammetry measurements are linearly dependent on the scan rate up to 1.5 V/s (Figure 5.14(a)) suggesting that the electron transfer process is confined to the surface (i.e. diffusionless system). As the cyclic voltammograms look asymmetric, the angular coefficient calculated from the linear fitting of the peak current density against scan rate data is different for anodic and cathodic current and it is not possible to evaluate the electrode surface coverage ((11.4 ± 0.8) x 10^{12} molecules per cm^2) as accurately as for the haem-D50C proteins deposited on Au(111).

The electron transfer rate constant was evaluated from the redox peak current divergence observed with the sweep rates in the range 5 Vs^{-1}-22 Vs^{-1} according to the method developed by Laviron (equation (5.12)). The obtained rate of electron transfer (13.5 ± 2.2 s^{-1}) is quite similar to the one evaluated for the holo-D50C cyt b_{562}.
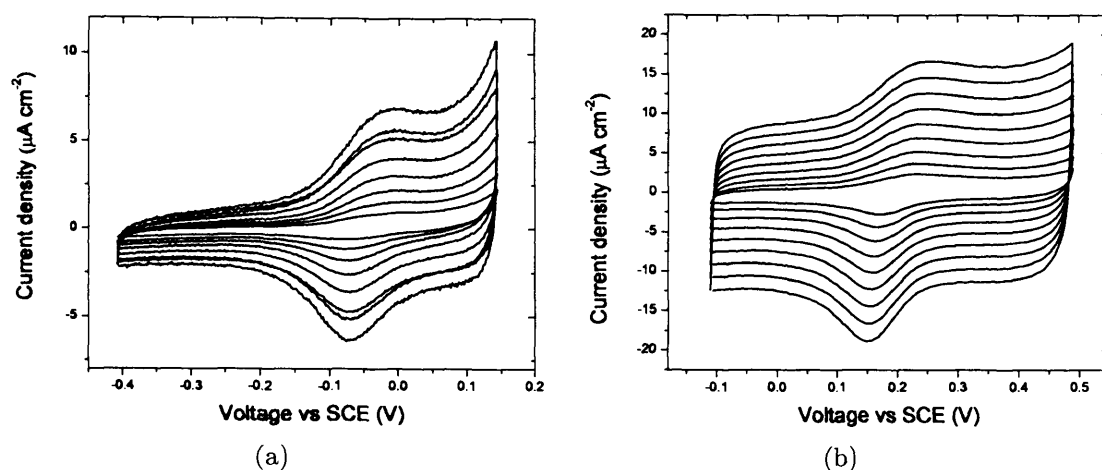
Figure 5.13: (a) Cyclic voltammetry of Cu-PP in 10 mM PB pH 6.2 at various scan rates (from 0.1 Vs^{-1} to 0.9 Vs^{-1}). For performing the experiment 1 ml of 100 μM Cu-PP in 0.1 M NaOH were dissolved in 5 ml of PB. (b) Cyclic voltammetry of D50C cysteine mutants reconstructed with Cu-PP and deposited on Au(111) in 10 mM phosphate buffer pH 6.2 at various scan rates (from 0.1 Vs^{-1} to 0.9 Vs^{-1}).

By simply changing the iron redox center to a copper one I have demonstrated that while the native haem pocket structure and the electron transfer properties of the haem protein are preserved, its redox potential can be positively shifted of $\sim$270 mV. This result confirms what is observed for natural cytochromes where the simple oxidation/reduction of the haem seems to be responsible for the electron transfer reaction, and different co-ordination to the metal site, modifications in the porphyrin side chains, solvation of the iron center and electrostatic interaction with amino acids and other molecules modulate the protein's redox potential in order to facilitate the protein's electron transfer function [109].

5.3.2 Direct visualization of single molecules using STM imaging

In-situ STM imaging supports the electrochemical analysis demonstrating that molecular sub-monolayer of holo-D50C, SH-SA and SH-LA cyt b_{562} were deposited onto freshly annealed Au(111) surfaces (Figure 5.15). Protein monolayers could be adsorbed on the Au(111) surface increasing the protein concentration ($\sim$ 100 μM) and the adsorption time ($\sim$ 24 hours). Due to the strong Au(111)-protein interaction, high resolution and robust single-protein STM imaging was achieved under solution conditions and electrochemical control in constant current mode. Even though atomic resolution of the biomolecules could not be achieved due to their flexibility and low relative conductance properties, tunnelling imaging provided an insight into the electronic properties of the cyt b_{562} variants.

95
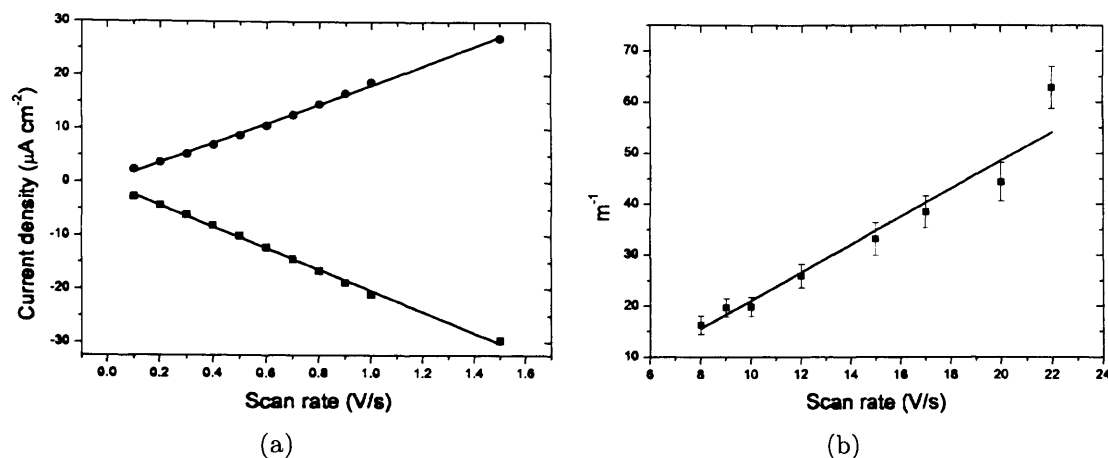
Figure 5.14: (a) Relation between the anodic (circle dots) and cathodic (square dots) peak currents and scan rates for D50C reconstructed with Cu-PP. (b) Plot of m^{-1} versus scan rate. The m values were obtained from the peak separations in the cyclic voltammograms. The electron transfer rate constant is estimated from the slope of the curve fitting the experimental data according to equation (5.12) (solid line).

EC-STM measurements of the Au(111)-wild-type cyt b_{562} system did not show any molecule binding to the electrode surface (Figure 5.16(a)). These results provided further evidence to the hypothesis that the cyt b_{562} cysteine mutants bind to the gold surface through their free thiol.

A low coverage was well suited for investigating the proteins electron transfer properties at single molecule level and the *in-situ* EC-STM images of D50C (Figure 5.16(b)), SH-SA (Figure 5.16(c)) and SH-LA (Figure 5.16(d)), respectively, adsorbed monolayers show that the proteins are uniformly distributed and cover only 5-10% of the gold surface. This result agrees with the surface coverage evaluated from analysis of the proteins cyclic voltammograms showing that the immobilized proteins retain their electron transfer properties after adsorption on the metallic surface (section 5.3.1).

Analysis of the cross sections of the two cyt b_{562} variants gives the height and the average lateral size (full width at half maximum) distributions (Figure 5.17). Due to the cysteine position and the approximately cylindrical shape of the protein (5.1 nm long, 2.6 nm diameter), the molecular orientation of the cyt b_{562} cysteine variants onto the gold surface is expected to be different. The SH-SA should bind to the Au(111) substrate on its long axis and resemble an oval shape when imaged whereas the D50C and SH-LA should bind at the tips of the long axis and display a circular shape. A small difference in the average lateral dimensions of the cysteine variants was evidenced in the *in-situ* STM imaging, indicating that the proteins adsorb in distinct orientations. The lateral sizes are 3.3 ± 0.7 nm for D50C, 4.5 ± 0.7 nm for SH-SA and 3.2 ± 0.5 nm for SH-LA (Figure 5.17(b)), which are close to
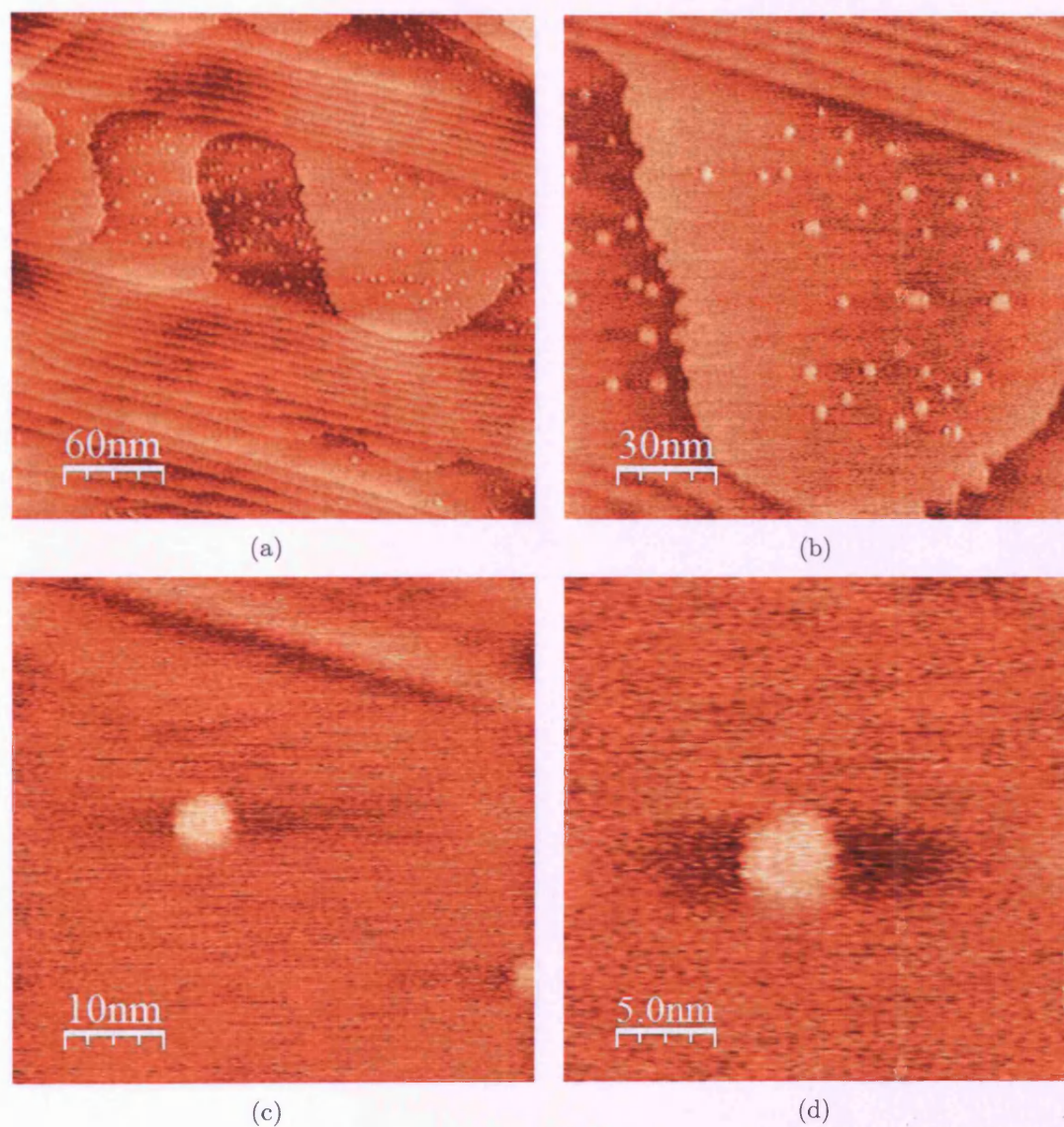
Figure 5.15: EC-STM images of SH-LA molecules self-assembled on Au(111) surfaces obtained in liquid environment (10 mM phosphate buffer, pH 6.2). Working electrode potential -0.10 V vs SCE, tunnelling current 35 pA, bias voltage -0.4 V. Scan areas: (a) 300 x 300, (b) 150 x 150, (c) 50 x 50, (d) 25 x 25 nm^2.
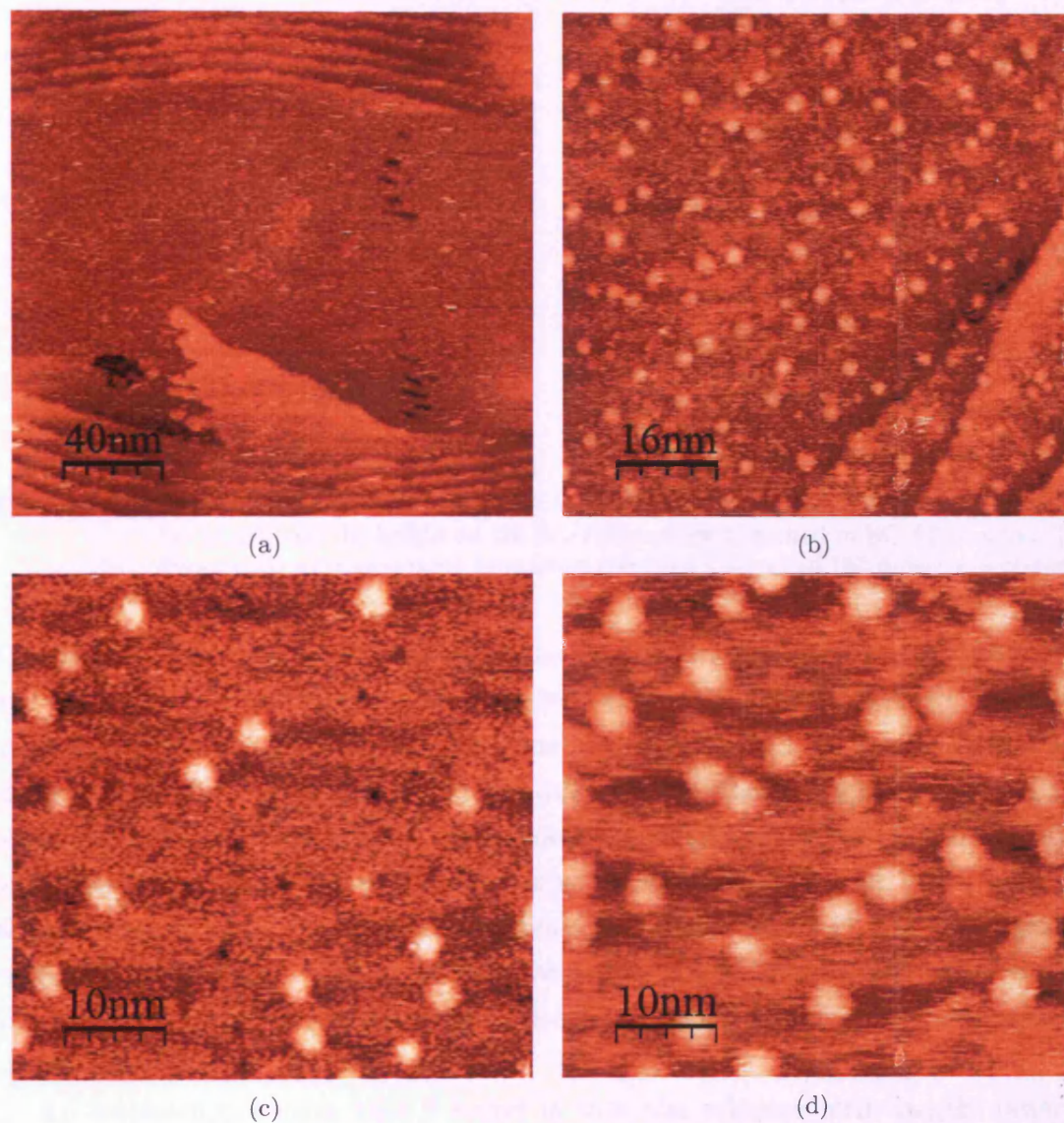
Figure 5.16: *In-situ* STM images of (a) wild-type, (b) D50C, (c) SH-SA and (d) SH-LA molecules self-assembled on Au(111) surfaces obtained under electrochemical environments (10 mM phosphate buffer, pH 6.2). Working electrode potential -0.10 V vs SCE, tunnelling current 35 pA, bias voltage -0.4 V.
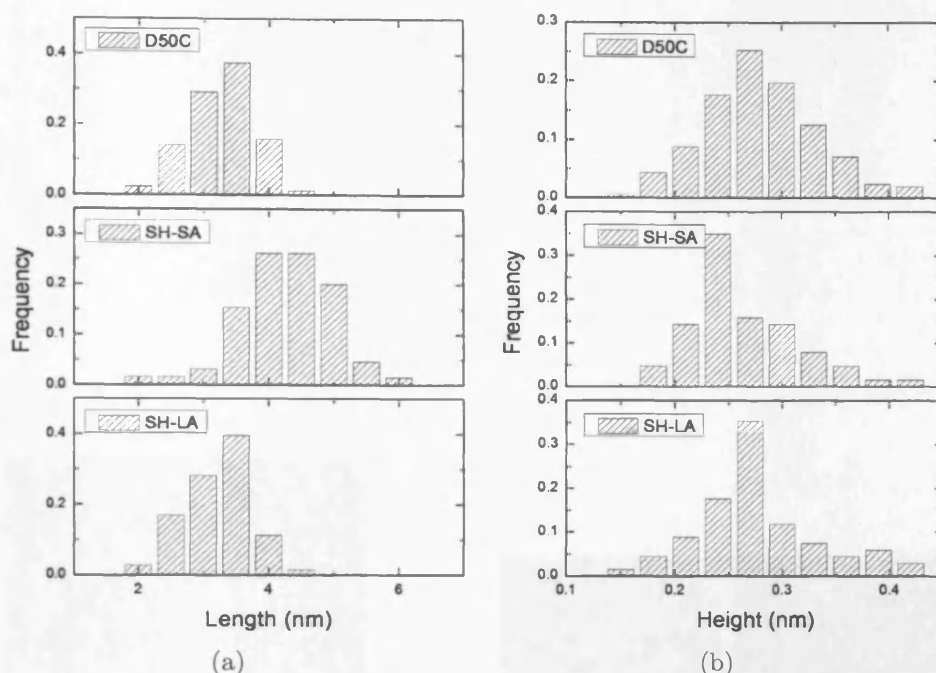
Figure 5.17: Statistical analysis of holo-D50C, holo-SH-SA and holo-SH-LA cyt b_{562} molecules (a) length and (b) height on the Au(111) surface measured in EC-STM mode. The dimensions were evaluated from cross sectional analysis of 150 different proteins.

the dimension derived from analysis of the atomic structure of the cytochrome [50] and agree within the experimental error with the values determined from statistical analysis of the STM experiments performed in air (Table 4.1). Tip convolution and the proteins' flexibility could explain the difference between the apparent lateral size of the proteins and the expected dimensions. The apparent height (0.25-0.28 nm) is one order of magnitude lower than the expected real height (2.6 nm or 5.1 nm). As already observed when imaging the proteins in air (section 4.3.1), the low apparent height of the molecules is due to their very low conductivity (10^{-15}-10^{-18} Sm^{-1}) and the STM probe compresses the molecules in order to maintain the tunnelling current set-point [23, 35, 38].

An interesting feature that I found is that the proteins form largely ordered structures onto high index surfaces like Au(111) steps (Figure 5.18(a)). The proteins seem to line up over very large surface areas probably indicating preferred adsorption sites on the Au(111) surface for the cytochrome mutants (Figure 5.18(b)).

The proteins could also be unfolded by applying high bias voltages ($V_b \geq 1.5$ V) (Figure 5.19(a)) and proteins desorption from the Au(111) surface was directly observed when the working electrode potential was brought to negative values ($\leq$ -0.8 V vs SCE) (Figure 5.19(b) and (c)). This value is close to the Au-sulphur reductive desorption potential indicating that the cysteine mutants proteins bind to

Figure 5.18: EC-STM images of (a) SH-SA molecules self-assembled on Au(111) surfaces obtained in 10 mM phosphate buffer pH 6.2 and a cartoon showing the proposed alignment of the molecules on the gold steps. (b) SH-LA molecules adsorbed on Au(111) surface. Working electrode potential -0.10 V vs SCE, tunnelling current 35 pA, bias voltage -0.4 V. Scan area: 100 nm^2

(a)   (b)   (c)
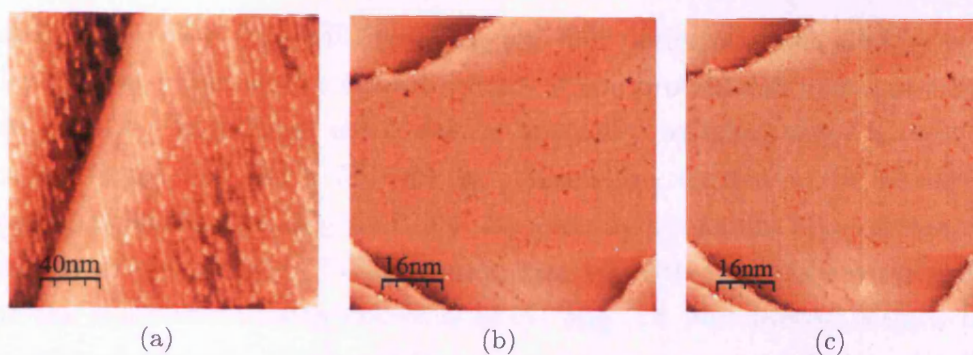
Figure 5.19: (a) STM image of D50C molecules self-assembled on Au(111) surfaces obtained under electrochemical environments (10 mM phosphate buffer, pH 6.2). Working electrode potential -0.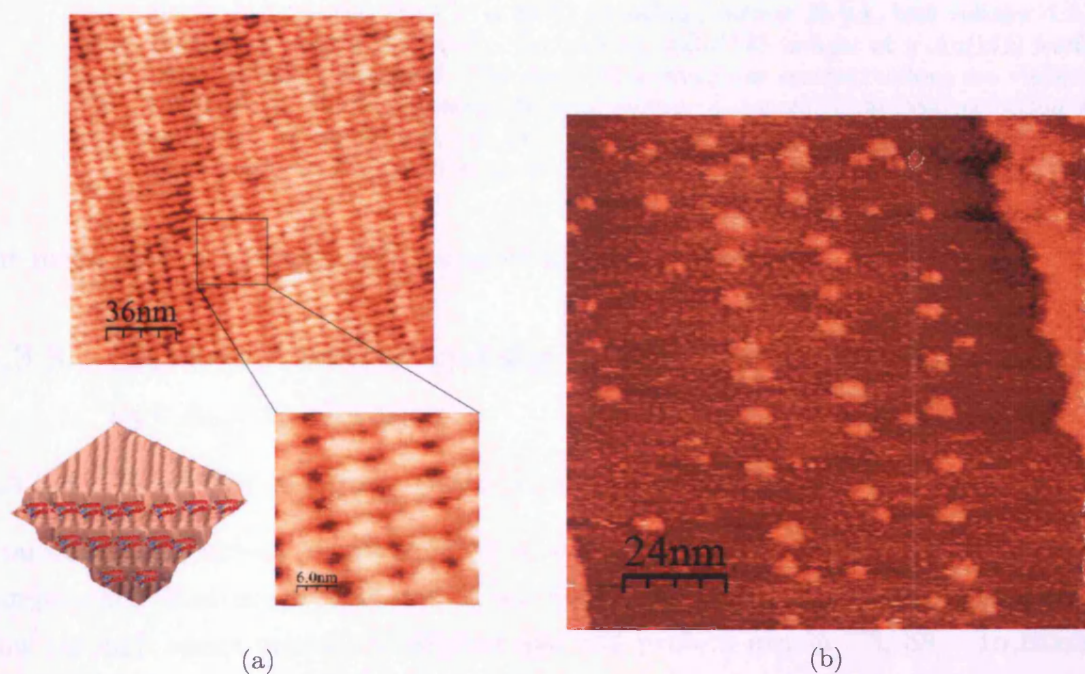10 V vs SCE, tunnelling current 35 pA, bias voltage -1.5 V. Scan area: 200 x 200 nm^2. (b) and (c) EC-STM images of a Au(111) surface after proteins desorption. The Au(111) herringbone reconstructions are visible on the surface. While scanning the gold surface a change of the reconstruction was observed. Working electrode potential -0.80 V vs SCE, tunnelling current 35 pA, bias voltage -0.2 V. Scan area: 80 x 80 nm^2.

the metal surface through their exposed cysteine residue.

5.3.3 Electrochemical gating of the conductance of single cyt b_{562} molecules

5.3.3.1 EC-STM imaging and I-V$_b$ measurements

Transistor-like current modulation is a desirable feature for molecular electronic components. Electrochemical gating has been used previously to modulate current flow through redox organic molecules and the protein azurin [73, 88]. To characterize the dependence of the electronic properties of the cyt b_{562} variants on their redox potential, protein conductance in electrolytes was measured using STM under electrochemical control [44, 137]. Keeping the bias voltage between the tip and the substrate constant and adjusting the tip and substrate potentials in parallel, the system can operate in a way similar to a conventional field effect transistor (FET). Unlike an FET where the gate electrode tunes the current flowing through a channel by changing the carrier density, in the electrochemical STM the current through a single molecule is controlled by the redox state of the molecule [116]. Thus, by adjusting substrate potential, the STM tip and substrate Fermi levels can be moved relative to the energy levels of the proteins [117].

The effect of electrochemical gating on the SH-SA and SH-LA mutants was examined both by imaging and I-V$_b$ measurement at various substrate potentials (E$_s$). In order to calculate the protein's redox potential against the platinum reference electrodes, cyclic voltammetry measurements were performed before engaging the

system (Figure 5.20). The STM imaging was first performed with a larger scan area such as 150 nm x 150 nm to obtain images of the protein sub-monolayer and then focused on a few individual molecules by gradually reducing the scan area. Small area scans (e.g. ~50 nm x 50 nm) at a tunnelling current of 35 pA show well-resolved single molecules (Figure 5.21). By keeping a constant bias voltage between the substrate and the tip, STM imaging started with the substrate potential set around the equilibrium redox potential of cyt b_{562} (i.e. zero overpotential). Imaging was continued towards either positive or negative overpotentials by adjusting the substrate and tip potentials in parallel (i.e. with fixed bias voltage) and finally returned to the equilibrium potential. As a result, a series of STM images at various overpotentials were acquired at various overpotentials. Figure 5.21 shows some representative images of the SH-SA molecules. At a negative overpotential (proteins fully reduced) an apparent height of 2.2 $\pm$ 0.2 Å was observed (Figure 5.21(a) and (b)). At more positive overpotential values the molecules display a higher apparent height (Figure 5.21(c) and (d)). Under positive potentials where the protein is fully oxidised, a decrease in apparent height to 2.8 $\pm$ 0.2 Å was observed (Figure 5.21(e)). On returning to the negative overpotentials, the original height was observed.

The experimental observations represented in Figure 5.21 can be well explained by a two-step electron transfer mechanism in the STM redox process (Figure 5.22). The energy levels of the STM substrate (or working electrode), the STM tip, and a redox molecule located in the substrate-tip gap may all be modified by changing the substrate potential, but the difference between the substrate and the tip energy levels will remain constant if the bias voltage is fixed as the experimental conditions applied for Figure 5.21. As a consequence, the redox level is shifted relative to the substrate and tip Fermi levels by the overpotential. Furthermore, the redox level is strongly coupled to the environment with an initially oxidized (vacant) level (LUMO) above the tip Fermi level and an initially reduced (occupied) level (HOMO) below the substrate Fermi level, when the bias voltage ($V_b = E_t - E_s$, where E_t and E_s are the potentials applied at the tip and the substrate, respectively) is negative as for the present case. Nuclear fluctuations bring initially the redox levels into the energy region close to the Fermi level of the electrodes, which in turn induces a two-step electron transfer process. At a negative bias voltage, electron transfer proceeds first from the tip to the vacant redox level and then from the temporarily occupied redox level to the substrate. The tunnelling current is thus gated by the molecular redox level position in respect to the metallic Fermi levels, which can be displayed directly by the changes in STM contrast. In other words, the contrast changes observed is due to the redox-gated tunnelling resonance.
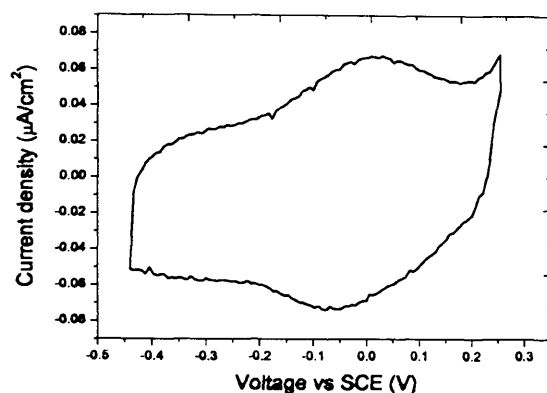
Figure 5.20: Cyclic voltammogram of cyt b_{562} SH-SA-Au(111) in 10 mM phosphate buffer (pH 6.2) recorded in the EC-STM configuration. Scan rate 50 mVs^{-1}.

Plots of applied overpotential against apparent height (Figure 5.23) display, as for the electron transfer properties obtained from cyclic voltammetry measurements (Table 5.1), no significant differences between D50C, SH-LA and SH-SA cyt b_{562} variants. The molecular height is clearly tuned by the redox state of the protein, with a maximum around the overpotential of -10 to -20 mV, very close to the equilibrium redox potential. The contrast decreases upon applying either negative or positive overpotentials, with the effects being quite symmetric. The apparent contrast enhancement can be up to 2 Å, equivalent to an increase in the tunnelling current by ca. 1 order of magnitude assuming that the decay factor of the tunnelling current is ~1.0 Å^{-1} (section 3.1). The maximum enhancement (i.e., the on/off ratio) is up to a factor of 2-3, which is slightly smaller than that observed for the protein azurin (ca. 9) [27] and significantly smaller than that for small molecules such as iron porphyrin (ca. 20) [117] or Os-polypyridine complexes [2]. The following factors may account for the relatively small apparent enhancement: (a) a relatively large bias (e.g., -0.4 V) is needed to obtain molecular resolution STM images for cyt b_{562} (Figure 5.21). (b) The tunnelling current needed to be set at a small value (35 pA) in comparison with the azurin case where the tunnelling current was set at 100-200 pA. (c) Because of a larger distance (~20 Å), electron transfer between the protein and the substrate is much slower (40-60 s^{-1}) than that either for the iron porphyrin case where iron porphyrin molecules were in direct contact with the HOPG surface and electron transfer was almost completely reversible or for the azurin case where the distance between the copper redox center and the gold surface was only 11 Å leading to an electron transfer rate larger than 500 s^{-1}.

As a comparison, similar STM imaging was performed at a fixed tip potential, which means that the bias voltage changed with changing the working electrode potential. The correlation between the apparent tunnelling contrast and the over-
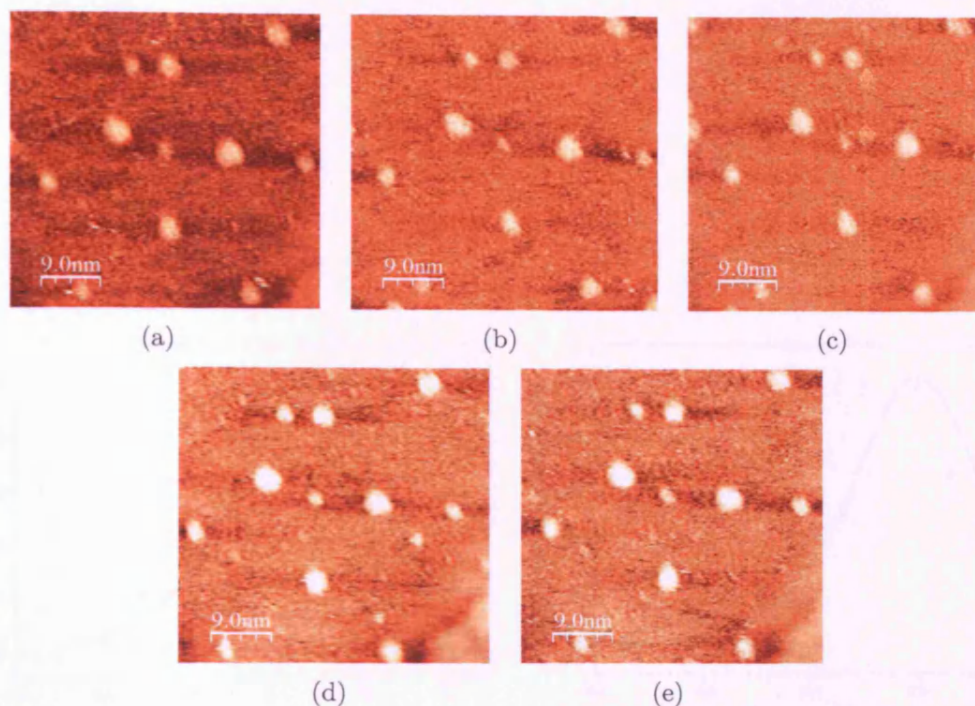
Figure 5.21: Electrochemical STM images of SH-SA molecules acquired at different overpotentials (η = -280 mV(a), η = -200 mV (b), η = -140 mV (c), η = -60 mV(d), η = 10 mV (e)) with a constant current mode. Current set-point = 35 pA, V_b= -0.40 V. Scan area: 45 nm x 45 nm, z-range = 0-2.0 nm.
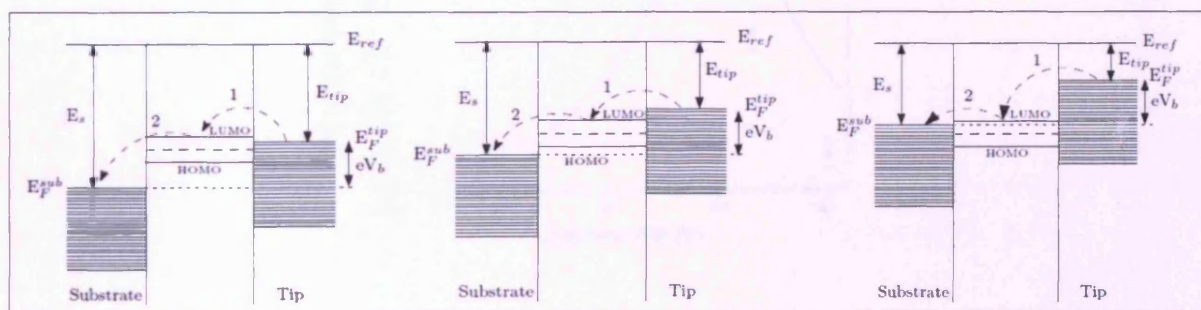
Figure 5.22: Energy diagram describing the enhancement of tunnelling current according to the sequential two step electron transport mechanism (all the energy values are related to an arbitrary reference level). The tip and the substrate Fermi levels (E_F^{tip} and E_F^{sub}) are separated by energy equal to eV_b kept constant through the experiment (eV_b=E_F^{sub}-E_F^{tip}). The two Fermi energies E_F^{tip} and E_F^{sub} can be shifted in parallel with respect to the reference Fermi level tuning the substrate electrode potential. When the substrate Fermi level is brought close to the protein equilibrium energy, electrons tunnel from the tip to a molecule vacant state (1) and, before the level relaxes vibrationally below the tip Fermi energy, electrons transfer to the substrate (2). However, for large eV_b the electrons transfer occurs also when the substrate potential is brought to more negative or positive values because some protein redox states lie between the electrode and tip states. This could explain why just a small increase in the tunnelling current can be observed in the investigated potential window.
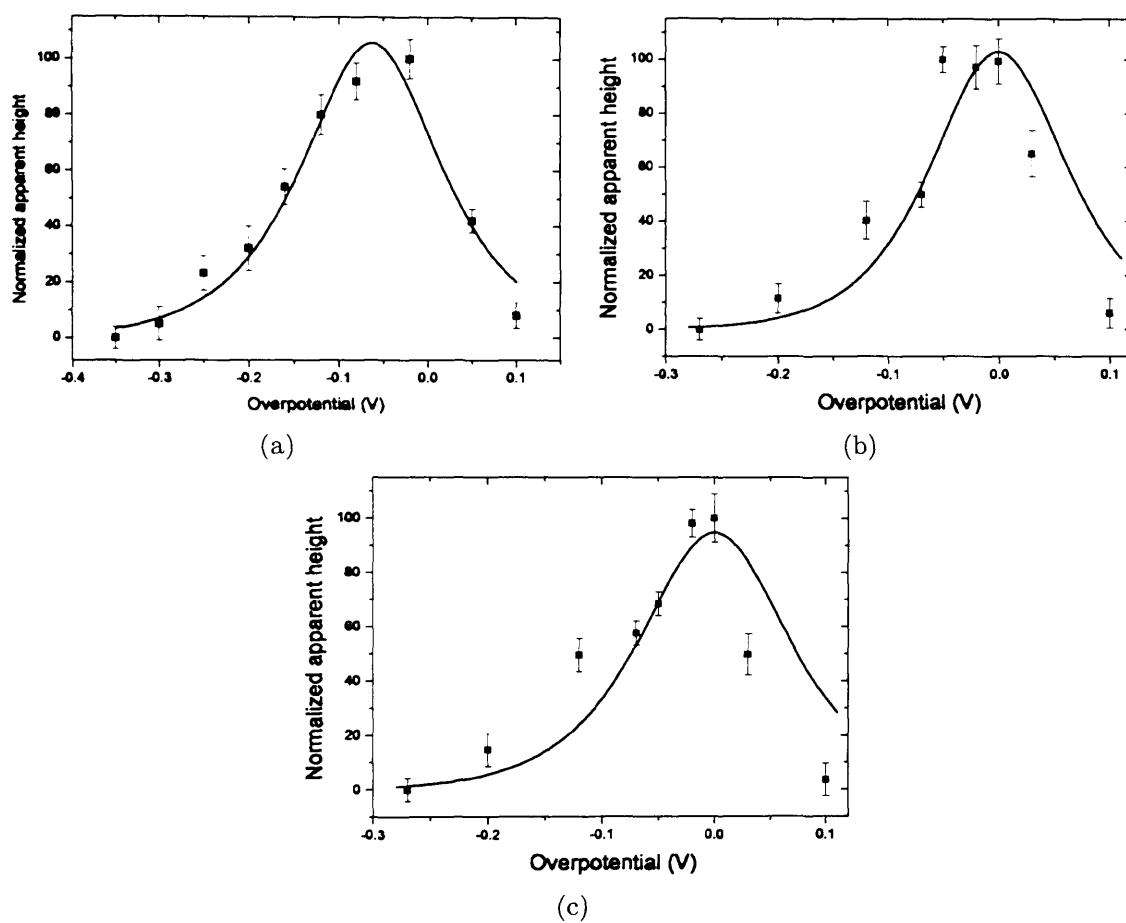
Figure 5.23: Dependence of apparent height on working electrode overpotential for (a) D50C, (b) SH-SA and (c) SH-LA molecules. The experimental data (square dots) were fitted according to equation (5.10) (solid line). The data were obtained at fixed bias voltage (-0.4 V).
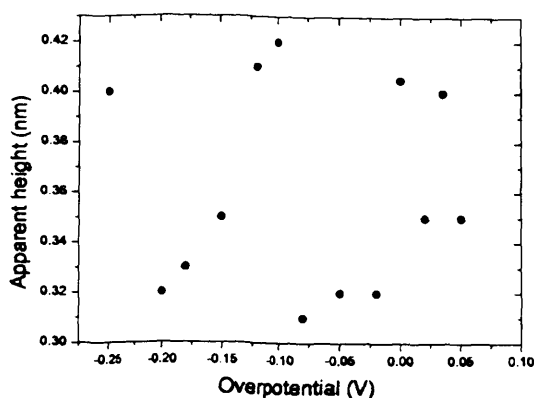
Figure 5.24: Dependence of apparent height on working potential. The data were obtained at fixed tip voltage (-0.80 V) and tunnelling current (35 pA) while changing the bias voltage (from -0.5 V to -0.80 V). Error bars are not shown for clarity.

potential (Figure 5.24) is largely unchanged across the overpotentials applied under such experimental conditions where two external parameters (i.e., the bias voltage and substrate potential) are changed simultaneously. As the molecular energy levels are mostly located either above or below the tip Fermi level, no significant resonant tunnelling is tuned by the substrate potential.

After imaging, the tip was positioned above a selected protein, the feedback loop was disengaged and I-V_b characteristics were recorded by sweeping the bias voltage from -0.2 V to 0.2 V. The I-V_b curves (Figure 5.25) were fitted with a simple third order polynomial function (equation (4.2)) and the conductance at zero bias was evaluated as a function of overpotential (Figure 5.26). The conductance peaks sharply at a substrate potential close to the equilibrium redox potential, where the molecular levels are aligned between the tip and substrate Fermi levels. The dependence of the conductance from the overpotential is largely similar to that for the molecular apparent height (Figure 5.23), but a much larger enhancement by a factor of 6-8 is observed. The large enhancement in conductivity is probably due to the lower bias at which the conductivity was calculated in respect to the bias voltage applied in the EC-STM imaging (0.4 V).

The data from the EC-STM imaging and the I-V_b experiments provide compelling evidence for a two-step electron transfer process mediated by the redox center (section 5.1.1), according to the model shown in Figure 5.22. The equation (5.10) is in quantitative agreement with the experimental measurements. As the maximum current through the molecule was measured at overpotential close to zero, I assumed that the redox center experiences all the substrate potential ($\xi = 1$) and half of the bias voltage ($\gamma = 0.5$) (the parameters ξ and γ describe the substrate-solution potential drop and bias voltage drop at the molecule redox center.). The reorganization energy can then be determined from a fit to the apparent height against overpoten-
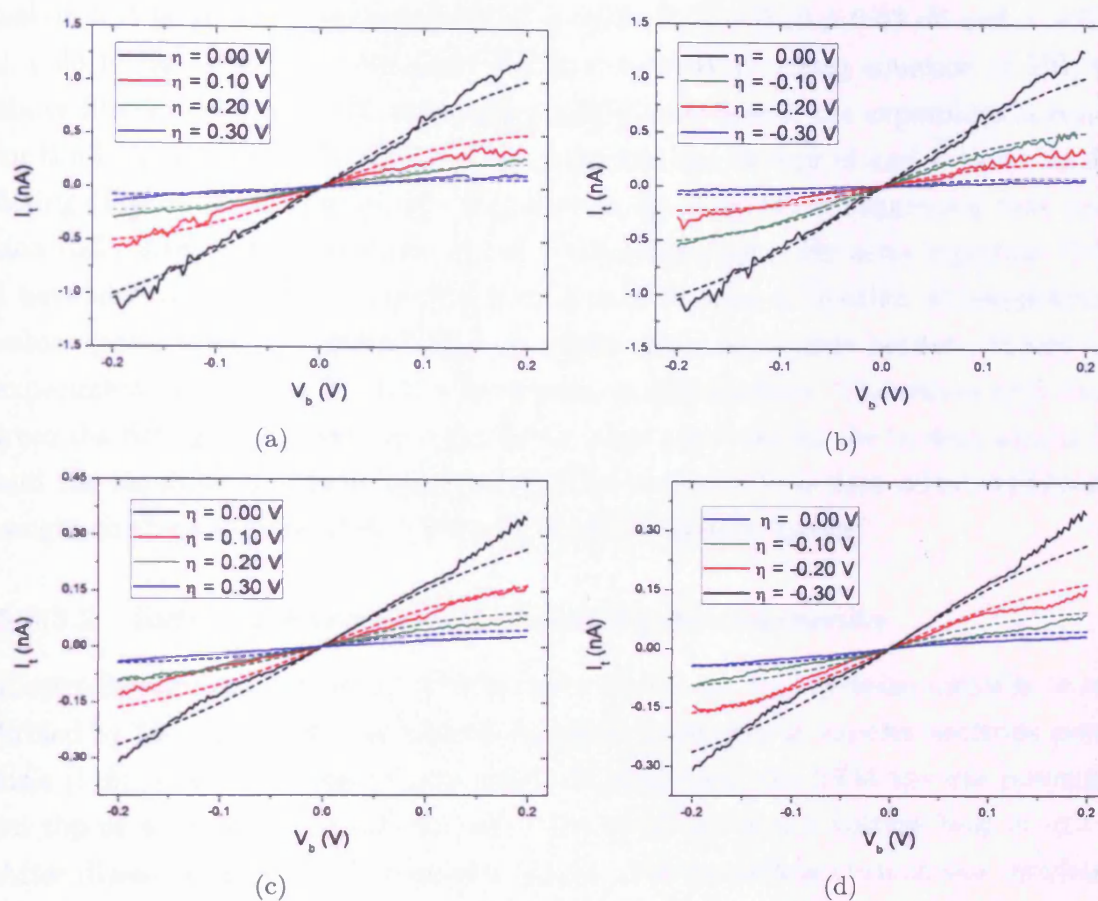
Figure 5.25: Individual I-V_b characteristics curves of single (a, b) SH-SA and (c, d) SH-LA at various (a, c) positive and (b, d) negative overpotentials. The dashed lines are calculated using equation (5.10), which are in good agreement with the experimental data (solid lines).
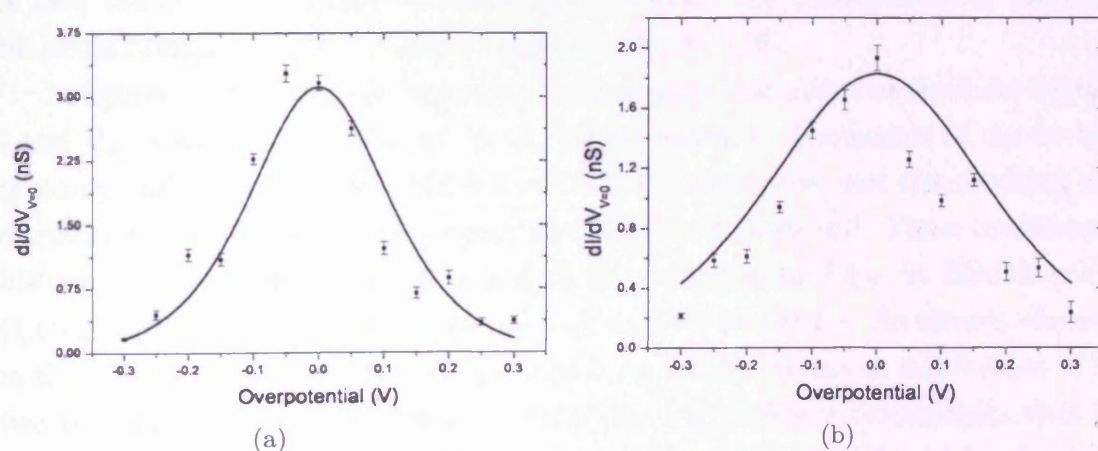
Figure 5.26: Dependence of molecular conductance at zero bias on working electrode overpotential for (a) SH-SA and (b) SH-LA. The squares and the error bars indicate the average and the standard deviation of a set of 100 data and the solid lines are curves calculated according to equation (5.10).

tial data (Figure 5.23), giving $\lambda = 0.12 \pm 0.03$ eV, $\lambda = 0.10 \pm 0.03$ eV and $\lambda = 0.15 \pm 0.03$ eV for D50C, SH-SA and SH-LA respectively. Using equation (5.10), the above fitted values of λ and adjusting a single scale factor, the experimental results for the I-V_b curves as a function of overpotential can be reproduced without further fitting (Figure 5.25, solid lines). The agreement is excellent suggesting that equation (5.1) gives a good account of the system dynamics. By using equation (5.10) I have also calculated the conductance at zero bias as a function of overpotential values (solid lines in Figure 5.26), and again good agreement between theory and experiment is achieved for both the protein configurations. The values of λ found from the fitting of our data are similar to those reported for the protein azurin [27] and the resulting accurate description of the experimental data adds considerable weight to the accuracy of the two-step electron transfer model.

5.3.3.2 Individual protein junctions: I-z measurements

Electrochemical gating of the conductance of the cyt b_{562} cysteine mutants is confirmed by I-z experiments performed on single molecules at various electrode potentials [116]. After obtaining single molecule resolution, the STM tip was positioned on top of a protein at a current set-point of 35 pA and a voltage bias of -0.1 V. After disengaging the STM feedback system, the tunnelling current was monitored as a function of tip displacement while moving the tip towards and away from the protein at fixed tip-substrate bias voltage. In this experimental setup, as the STM tip is pulled away from the surface, a single protein spans the gap and, if its free thiol binds a tip atom, a plateau of constant current can be measured until contact is lost; the current plateau can be used to identify the conductance of the single molecule bridging the two metallic contacts [73, 98, 116].

In figures 5.27(a)-(c), the molecular conductance, calculated as the ratio between I and V_b, is shown as a function of tip displacement z. Thousands of curves were typically collected for D50C, SH-SA and SH-LA molecules, and the resulting conductance values plotted in histogram form (Figures 5.27(d)-(f)). These conductance histograms show pronounced peaks at (2.47 ± 0.17) x 10^{-4} G_0 for SH-SA and at (1.65 ± 0.25) x 10^{-4} G_0 and (2.33 ± 0.17) x 10^{-4} G_0 for SH-LA. As already observed in the I-z experiments performed in air (section 4.3.4), the major implication of the two conductance peaks for SH-LA is that the two different orientations that the protein can occupy with respect to the Au(111) surface have different conductivity, due to the different distance to the haem center (Figure 1.1). The I-z traces show longer plateaus for the low conductance values than for the high conductance values (Figure 5.27(b)) perhaps related to a difference of binding of the STM tip to the
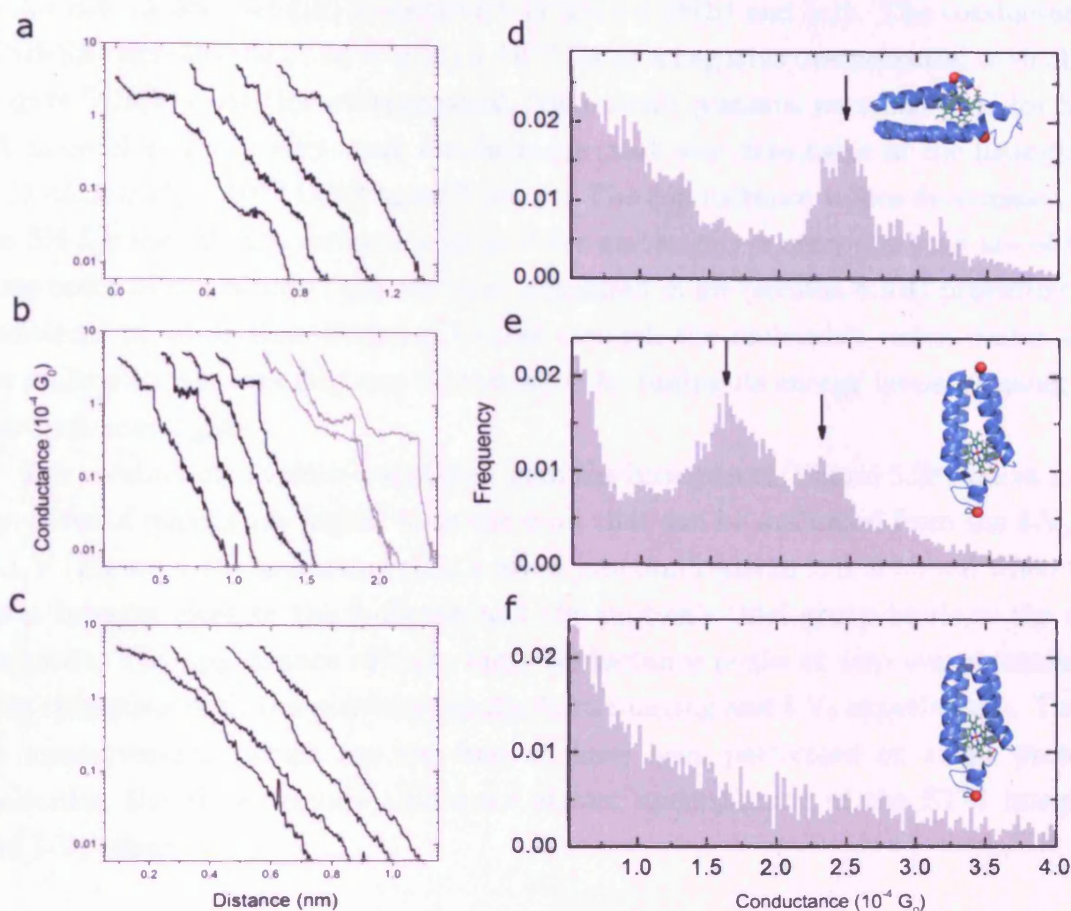
Figure 5.27: Measurements of conductance of single cyt b_{562} junctions. Individual conductance traces obtained in the I-z experiments of (a) SH-SA, (b) SH-LA and (c) D50C single cysteine mutant. Figure (b) shows the high (black) and low (gray) conductance traces. Conductance histograms constructed from 400 curves and obtained for (d) SH-SA, (e) SH-LA and (f) D50C single cysteine mutant at $V_b = -0.4$ V and $\eta = 0.0$ V. The arrows mark the peak position of the Gaussian fit (not shown for clarity).

molecule in each orientation.

As a control, the tunnelling current was probed against distance for the single cysteine mutant cyt b_{562} D50C (Figure 5.27(c)). No plateaus were observed, thus confirming that the presence of an exposed thiol on the protein structure (in addition to the thiol for binding on the Au(111)) is essential for the formation of a molecular bridge with the STM tip.

Electrochemical gating of the I-z measurements was also examined (Figure 5.28), which can be compared with the above results obtained at $\eta = 0$. The histograms calculated for the D50C did not show any conductance peak neither at positive and negative overpotentials (Figure 5.28(a)). On applying a positive overpotential (0.30 V), the conductance decreases to (1.45 ± 0.17) x 10^{-4} G_0 and (0.73 ± 0.10) x 10^{-4}

G_0 for SH-SA and SH-LA, respectively (Figure 5.28(b) and (c)). The conductance of SH-SA decreases to $(1.86 \pm 0.15) \times 10^{-4}$ G_0 at a negative overpotential of -0.30 V (Figure 5.28(b)). At this overpotential, few current plateaus were observed for SH-LA molecules, and a very weak conductance peak was detectable in the histogram at $(1.45 \pm 0.25) \times 10^{-4}$ G_0 (Figure 5.28(c)). The conductance values determined for the SH-SA and SH-LA molecules at positive and negative overpotentials are of the same order of magnitude than the ones measured in air (section 4.3.4) providing an additional proof to that electrons tunnel through the molecule's redox center and the molecule's conductivity can be enhanced by tuning its energy levels by using an electrochemical gate.

The conductance values calculated from the histograms (Figure 5.28) are at least one order of magnitude higher than the ones that can be evaluated from the I-V_b at -0.1 V (Figure 5.25) indicating that a lower junction resistance is achieved when the tip is brought close to the molecule and the protein's thiol group binds to the top electrode. The appearance of clear high-conductance peaks at zero overpotential is fully consistent with the previous results from imaging and I-V_b experiments. These I-z measurements, which are the first to have been performed on single protein molecules, therefore provide additional strong underpinning of the STM imaging and I-V_b results.

5.4 Conclusions

In this chapter I have shown that engineering the electron transfer protein cyt b_{562} to incorporate thiol linking groups allows not only the protein molecules to robustly self-assemble on a gold surface, but also opens feasible electron transfer pathway between two metallic electrodes. Electronic communication between the protein and a gold electrode can be directly detected by cyclic voltammetry with reasonably fast electron transfer rates even over a distance of 20 Å. The evaluated electron transfer rates are similar to the ones obtained for cyt b_{562} adsorbed onto Au(111) electrodes modified with amino-alkanethiols linking molecules. Therefore the thiol linking group can provide an immobilizing support as effective as a biocompatible coating of electrodes for adsorbing anionic proteins without denaturation. The calculated cysteine mutants' redox potential is the same of the wild-type cyt b_{562} indicating that the thiol moieties had no obvious effect on the structure or haem binding properties of the protein.

The current through the protein depends on the orientation of the molecule, controlled by the cysteine anchoring sites. Electrochemical STM techniques, including

(a)

(b)

(c)
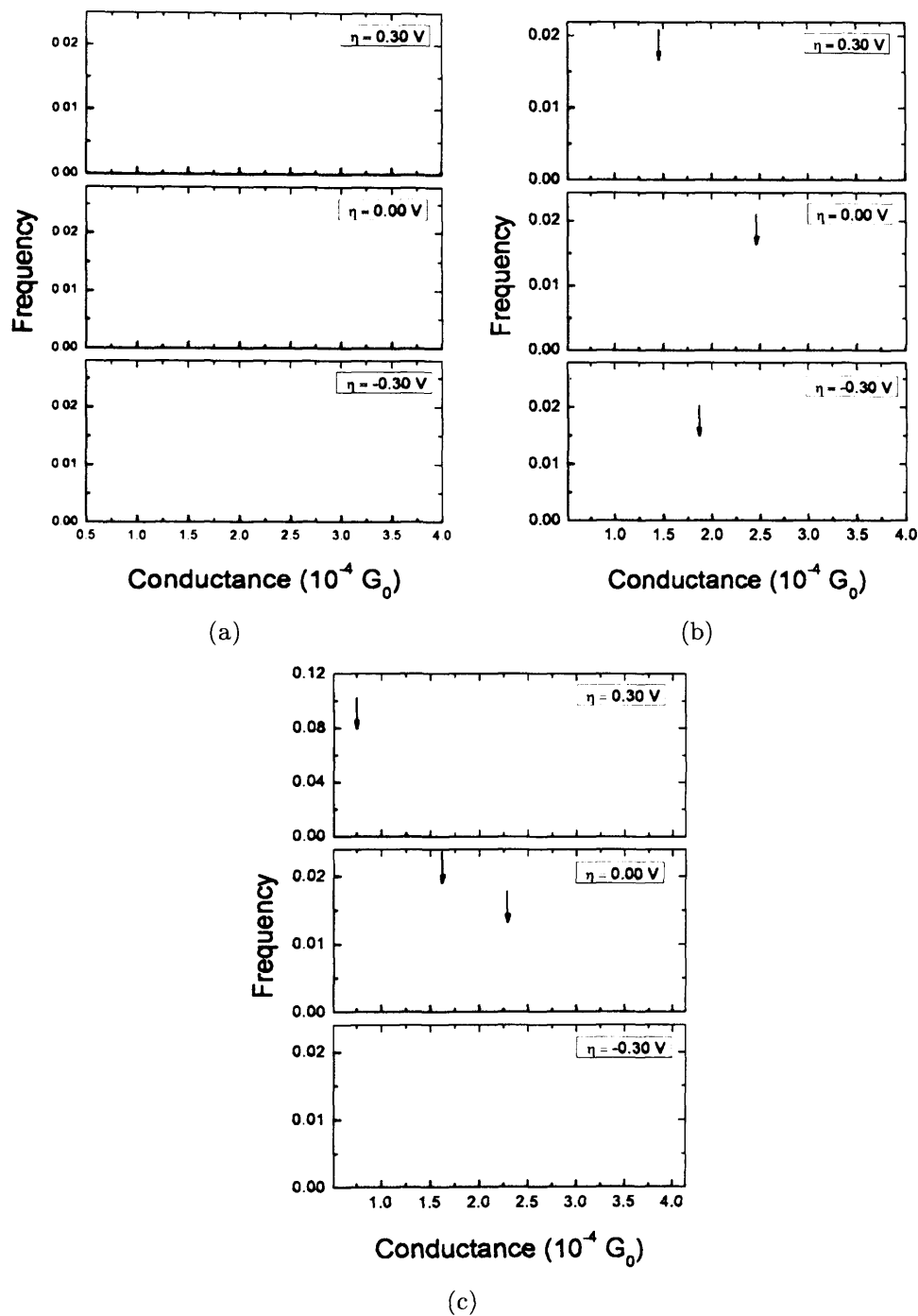
Figure 5.28: Measurements of conductance of single cyt b_{562} junctions, Conductance histograms constructed from 400 curves and obtained for (a) D50C, (b) SH-SA, (c) SH-LA at $V_b = -0.4$ V and varying the applied overpotential (reported in figure). The arrows in (b) and (c) mark the peak position of the Gaussian fit (not shown for clarity).

the first example of I-z experiments on proteins have demonstrated that the conductance of the redox protein can be reversibly modulated by electrochemical gating. The cyt b_{562} cysteine mutants show a higher conductivity when working potentials close to the redox potential are applied to the system and the energy levels of the molecules are aligned to the substrate and tip Fermi levels. Agreement with the KU theoretical model involving a two-step electron transfer mechanism in the adiabatic limit is very good, giving realistic physical values.

Chapter 6

Conclusions

This chapter summarizes the conclusions of my PhD project and presents recommendations for further work.

6.1 Achievements

Exploiting the ability of proteins to function at the single molecule level so as to, for example, integrate biomolecules as useful electronic components in solid-state devices, remains a significant and important challenge. A naturally occurring electron transfer protein, cytochrome b_{562}, has been engineered with two thiol groups introduced at different positions in the molecular structure to allow stable and robust binding and good electronic coupling to metallic electrodes in designated and defined orientations. Cyt b_{562} does not naturally contain any cysteine residues so thiol groups could be introduced at required positions to define the metal-protein interactions. The protein molecular modelling analysis revealed two different configurations ideal for the introduction of the cysteine residues. Residue pairs, Asp5 and Lys104 (SH-SA) and Asp21 and Asp50 (SH-LA), located along the short and long axes, respectively, of the protein were changed to thiol-containing cysteine residues. Residue Asp50 was also modified to cysteine (D50C) in order to study how control proteins containing only one thiol would interact with two metallic electrodes.

The cyt b_{562} gene was manipulated by site-directed mutagenesis and the proteins expressed in *E.coli* were purified according to standard techniques. Introduction of cysteines in place of the wild-type residues has no effect on the functionality of cyt b_{562}. UV-visible optical absorption spectroscopy results suggested that D50C, SH-SA and SH-LA cyt b_{562} variants retain the spectroscopic properties of the wild-type protein; both the haem binding properties and the redox characteristics of the cysteine mutants were similar to that of the non mutated cytochrome b_{562}.

Single cysteine mutant D50C and the two double cysteine mutants cyt b_{562} were immobilised on Au(111) electrodes and their electron transfer properties investigated by cyclic voltammetry. Their robust, quasi-reversible electrochemical reaction on pristine Au electrode show that the insertion of a thiol group in the protein's external surface is a suitable mean for protein immobilization on metal surfaces. The adsorption of the cysteine mutants cyt b_{562} on Au(111) through the sulfur-Au bonding was also confirmed by reductive desorption experiments. The wild-type protein (no cysteine mutation) and apo-cyt b_{562} D50C, SH-SA and SH-LA (no haem bound to protein) were used as controls and no Faradaic activity was measured indicating that the thiol anchoring group and the redox center are fundamental in promoting electron transfer at the gold-protein interface.

The voltammetric analysis showed that the electrode surface was not fully covered by electroactive proteins. STM and AFM experiments in air and *in-situ* EC-STM imaging supports the electrochemical analysis demonstrating that molecular sub-monolayers of D50C, SH-SA and SH-LA cyt b_{562} were deposited on freshly annealed Au(111) surface.

The proteins deposited directly on single crystal Au(111) electrodes were imaged to single molecule resolution and their structure was not significantly perturbed by interaction with the Au(111) surface. Stable SPM imaging of the cysteine variants showed that they can strongly bind to the gold surface while retaining their tertiary structure. The lateral dimensions of D50C, SH-SA and SH-LA were consistent with the predicted values for immobilisation via a single thiol and indicated that the cysteine variants adsorb on Au(111) in defined orientations, dictated by the thiol-pair utilised. The STM experiments performed on wild-type suggested that none of its amino acid could provide a stable binding of the protein to the gold surface and after few scans of the same surface in air the molecules were swept away.

Investigation of the protein's electronic properties by STM imaging revealed that molecular heights were strongly dependent on the current set-point value and the applied bias voltage. Analysis of the height measurements against the tunnelling current revealed a tunnelling decay constant β of 1.57 $\pm$ 0.25 Å^{-1}, indicating an efficient electron transmission through the protein.

The rod-like structure of the cyt b_{562}, containing four α-helices, gives the molecule sufficient strength to allow not only repeat STM and AFM scans, but also I-V$_b$ and I-z measurements without modification of the protein's structure and electronic properties. While STM imaging revealed that the presence of a single thiol in the protein is vital for its binding to a metal electrode, the I-V$_b$ and the I-z experiments showed that a second free thiol could provide a good means for enhancing

the molecule electrical contacts with another metal. A low lateral drift STM was designed and built to reliably measure the electronic properties of the proteins at a single molecular level. I-V_b curves recorded over time indicated that both variants were coupled tightly to the electrodes with conduction more efficient than the wild-type protein that contains no thiol groups. The I-z method, already used to probe the conduction of small organic molecules, was applied for the first time to proteins and allowed the study of the electronic properties of a single molecule controlling the tip-sample distance. The data obtained from these experiments show that the thiol groups could act as good molecular clamps and that the conductivity of the SH-SA variant was higher than the SH-LA probably due to the shorter distance between the Au electrodes and the iron center.

High-resolution STM imaging of individual D50C, SH-SA and SH-LA molecules achieved in a biological-friendly buffer and under electrochemical control demonstrated that the conductance of the cyt b_{562} can be reversibly modulated by electrochemical gating. I-V_b and I-z experiments, performed for the first time on proteins under potentiostatic control, were also used as tools to investigate the electrochemical gating of cyt b_{562} conduction. The results indicated a strong increase in conductance at working potentials close to the equilibrium redox potential of the protein due to resonant tunnelling as the redox level of the molecules are aligned to the electrodes' Fermi levels. Agreement with a theoretical model involving a two-step electron transfer mechanism is very good, giving realistic physical values.

Although the conduction mechanism of biomolecules is still debated, the relevance of this work is to show for the first time that, if properly engineered, a large and structurally complex molecule of significant biological and bionanotechnological significance as a metalloprotein can be bridged between two metal electrodes and its electronic properties can be probed at a single molecule level. The ability to utilize, measure and modulate the single molecule electron transfer characteristics of a protein directly at a metal electrode without linker molecules will further benefit the development of bioelectronics.

The work described in this PhD dissertation could be extended in several directions. A paper has already been published [43] and five other papers based on the results of this project have been or will be submitted to high-impact factor journals (see Appendix A). STM studies of the SH-SA and SH-LA double cysteine mutants under different temperature and humidity conditions deserve deep investigations in order to shed new light on the resonant tunnelling mechanism via the redox center of the cytochrome. The influence of the redox center could be also investigated by the replacement of the iron atom in the porphyrin ring by other metals. The apo-cyt

b_{562} has already been reconstructed with Cu-PP and a robust redox voltammetry signal has been measured; further investigations by EC-STM imaging at a single molecular level could help understanding the role of the redox center in determining the metalloprotein's electrical properties. Further detailed experiments of this nature will enable rigorous testing of theoretical models and investigation of biological electron transfer processes at the single molecule level.

Appendix A

List of Publications

1. **E. A. Della Pia**, Q. Chi, D. Jones, J. E. Macdonald, J. Ulstrup , M. Elliott, Single-Molecule Mapping of Long-range Electron Transport for a Cytochrome b_{562} Variant, Nano Letters,11,176-182.

2. **E. A. Della Pia**, Q. Chi, D. Jones, J. E. Macdonald, J. Ulstrup , M. Elliott, Electrochemical conductance gating for a single engineered redox-protein junction, submitted to Nature Nanotechnology.

3. **E. A. Della Pia**, M. Elliott, D. Jones, J. E. Macdonald, Engineered cytochrome b_{562} as a new nanoelectronic element, submitted to Nano Letters.

4. **E. A. Della Pia**, M. Elliott, J. E. Macdonald, D. Jones, Single molecule studies of the electron transfer protein cytochrome b_{562} engineered to contain thiol pairs, submitted to ACS Nano.

5. **E. A. Della Pia**, J. E. Macdonald, M. Elliott, Design of a low-drift scanning tunnelling microscope for operation at room temperature, manuscript in preparation.

6. **E. A. Della Pia**, Q. Chi, J. E. Macdonald, M. Elliott, D. Jones, J. Ulstrup, De-novo design and electrochemical characterization of a copper redox active protein, manuscript in preparation.

Bibliography

[1] T. Albrecht, A. Guckian, J. Ulstrup, and J. G. Vos. Transistor effects and in situ stm of redox molecules at room temperature. *IEEE Transactions on Nanotechnology*, 4(4):430–433, 2005.

[2] T. Albrecht, A. Guckian, J. Ulstrup, and J. G. Vos. Transistor-like behavior of transition metal complexes. *Nano Letters*, 5(7):1451–1455, 2005.

[3] A. Alessandrini, S. Corni, and P. Facci. Unravelling single metalloprotein electron transfer by scanning probe techniques. *Physical Chemistry Chemical Physics*, 8(38):4383–4397, 2006.

[4] K. Alston and C. B. Storm. Copper(II) protoporphyrin IX as a reporter group for the heme environment in myoglobin. *Biochemistry*, 18(20):4292–4300, 1979.

[5] L. Andolfi, A. R. Bizzarri, and S. Cannistraro. Assembling of redox proteins on au(111) surfaces: A scanning probe microscopy investigation for application in bio-nanodevices. *Thin Solid Films*, 515(1):212–219, 2006.

[6] L. Andolfi, B. Bonanni, G. W. Canters, M. P. Verbeet, and S. Cannistraro. Scanning probe microscopy characterization of gold-chemisorbed poplar plastocyanin mutants. *Surface Science*, 530(3):181–194, 2003.

[7] L. Andolfi, D. Bruce, S. Cannistraro, G. W. Canters, J. J. Davis, H. A. O. Hill, J. Crozier, M. P. Verbeet, C. L. Wrathmell, and Y. Astier. The electrochemical characteristics of blue copper protein monolayers on gold. *Journal of Electroanalytical Chemistry*, 565(1):21–28, 2004.

[8] L. Andolfi and S. Cannistraro. Conductive atomic force microscopy study of plastocyanin molecules adsorbed on gold electrode. *Surface Science*, 598(1-3):68–77, 2005.

[9] L. Andolfi, S. Cannistraro, G. W. Canters, P. Facci, A. G. Ficca, I. M. C. Van Amsterdam, and M. P. Verbeet. A poplar plastocyanin mutant suitable for adsorption onto gold surface via disulfide bridge. *Archives of Biochemistry and Biophysics*, 399(1):81–88, 2002.

[10] L. Andolfi, P. Caroppi, A. R. Bizzarri, M. C. Piro, F. Sinibaldi, T. Ferri, F. Polticelli, S. Cannistraro, and R. Santucci. Nanoscopic and redox characterization of engineered horse cytochrome c chemisorbed on a bare gold electrode. *Protein Journal*, 26(4):271–279, 2007.

[11] H. Atamna and H. Ginsburg. Heme degradation in the presence of glutathione. a proposed mechanism to account for the high levels of non-heme iron found in the membranes of hemoglobinopathic red blood cells. *Journal of Biological Chemistry*, 270(42):24876–24883, 1995.

[12] D. N. Axford and J. J. Davis. Electron flux through apo- and holo-ferritin. *Nanotechnology*, 18(14), 2007.

[13] P. D. Barker, J. L. Butler, P. De Oliveira, H. A. O. Hill, and N. I. Hunt. Direct electrochemical studies of cytochromes b_{562}. *Inorganica Chimica Acta*, 252(1-2):71–77, 1996.

[14] P. D. Barker, K. Di Gleria, H. A. O. Hill, and V. J. Lowe. Electron transfer reactions of metalloproteins at peptide-modified gold electrodes. *European Journal of Biochemistry*, 190(1):171–175, 1990.

[15] P. D. Barker, E. P. Nerou, S. M. V. Freund, and I. M. Fearnley. Conversion of cytochrome b_{562} to c-type cytochromes. *Biochemistry*, 34(46):15191–15203, 1995.

[16] N. Bennett, G. Xu, L. J. Esdaile, H. L. Anderson, J. E. MacDonald, and M. Elliott. Transition voltage spectroscopy of porphyrin molecular wires. *Small*, 6(22), 2010.

[17] B. Bhushan, H. Fuchs, and S. Hosaka. *Applied scanning probe methods*. Number v. 1 in Nanoscience and technology. Springer, 2004.

[18] G. Binnig and H. Rohrer. Scanning tunneling microscopy from birth to adolescence. *Reviews of Modern Physics*, 59(3):615–625, 1987.

[19] G. Binnig, H. Rohrer, Ch Gerber, and E. Weibel. Tunneling through a controllable vacuum gap. *Applied Physics Letters*, 40(2):178–180, 1982.

[20] G. Binnig and D. P. E. Smith. Single-tube three-dimensional scanner for scanning tunneling microscopy. *Review of Scientific Instruments*, 57(8):1688–1689, 1986.

[21] B. Bonanni, D. Alliata, L. Andolfi, A. R. Bizzarri, I. Delfino, and S. Cannistraro. Yeast cytochrome c on gold electrode: A robust hybrid system for bio-nanodevices. pages 574–576, 2004.

[22] B. Bonanni, D. Alliata, A. R. Bizzarri, and S. Cannistraro. Topological and electron-transfer properties of yeast cytochrome c adsorbed on bare gold electrodes. *Chemphyschem*, 4:1183–1188, 2003.

[23] B. Bonanni, L. Andolfi, A. R. Bizzarri, and S. Cannistraro. Functional metalloproteins integrated with conductive substrates: Detecting single molecules and sensing individual recognition events. *Journal of Physical Chemistry B*, 111(19):5062–5075, 2007.

[24] B. Bonanni, A. R. Bizzarri, and S. Cannistraro. Optimized biorecognition of cytochrome c_{551} and azurin immobilized on thiol-terminated monolayers assembled on au(111) substrates. *Journal of Physical Chemistry B*, 110:14574–14580, 2006.

[25] F. Chen, J. Hihath, Z. Huang, X. Li, and N. J. Tao. Measurement of single-molecule conductance. *Annu Rev Phys Chem.*, 58:535–564, 2007.

[26] J. Chen, T. Markussen, and K. S. Thygesen. Quantifying transition voltage spectroscopy of molecular junctions: Ab initio calculations. *Physical Review B - Condensed Matter and Materials Physics*, 82(12), 2010.

[27] Q. Chi, O. Farver, and J. Ulstrup. Long-range protein electron transfer observed at the single-molecule level: In situ mapping of redox-gated tunneling resonance. *Proceedings of the National Academy of Sciences of the United States of America*, 102(45):16203–16208, 2005.

[28] Q. Chi, J. Zhang, J. E. T. Andersen, and J. Ulstrup. Ordered assembly and controlled electron transfer of the blue copper protein azurin at gold (111) single-crystal substrates. *Journal of Physical Chemistry B*, 105(20):4669–4679, 2001.

[29] Q. Chi, J. Zhang, E. P. Friis, J. E. T. Andersen, and J. Ulstrup. Electrochemistry of self-assembled monolayers of the blue copper protein pseudomonas

aeruginosa azurin on au(111). *Electrochemistry Communications*, 1(3-4):91–96, 1999.

[30] Q. Chi, J. Zhang, P. S. Jensen, H. E. M. Christensen, and J. Ulstrup. Long-range interfacial electron transfer of metalloproteins based on molecular wiring assemblies. *Faraday discussions*, 131:181–195, 2006.

[31] Q. Chi, J. Zhang, J. U. Nielsen, E. P. Friis, I. Chorkendorff, G. W. Canters, J. E. T. Andersen, and J. Ulstrup. Molecular monolayers and interfacial electron transfer of pseudomonas aeruginosa azurin on au(111). *Journal of the American Chemical Society*, 122(17):4047–4055, 2000.

[32] J. Clavilier, R. Faure, G. Guinet, and R. Durand. Preparation of monocrystalline pt microelectrodes and electrochemical study of the plane surfaces cut in the direction of the 111 and 110 planes. *Journal of Electroanalytical Chemistry*, 107(1):205–209, 1979.

[33] S. A. Contera and H. Iwasaki. Imaging the proteins pseudoazurin and apo-pseudoazurin on gold by stm in air: Effect of the bias voltage. *Ultramicroscopy*, 91(1-4):231–243, 2002.

[34] X. D. Cui, A. Primak, X. Zarate, J. Tomfohr, O. F. Sankey, A. L. Moore, T. A. Moore, D. Gust, G. Harris, and S. M. Lindsay. Reproducible measurement of single-molecule conductivity. *Science*, 294(5542):571–574, 2001.

[35] J. J. Davis. Molecular bioelectronics. *Philosophical Transactions of the Royal Society A: Mathematical, Physical and Engineering Sciences*, 361(1813):2807–2825, 2003.

[36] J. J. Davis, D. Djuricic, K. K. W. Lo, E. N. K. Wallace, L. Wong, and H. A. O. Hill. A scanning tunnelling study of immobilised cytochrome p450cam. *Faraday discussions*, 116:15–22, 2000.

[37] J. J. Davis, C. M. Halliwell, H. A. O. Hill, G. W. Canters, M. C. Van Amsterdam, and M. P. Verbeet. Protein adsorption at a gold electrode studied by in situ scanning tunnelling microscopy. *New Journal of Chemistry*, 22(10):1119–1123, 1998.

[38] J. J. Davis and H. A. O. Hill. The scanning probe microscopy of metalloproteins and metalloenzymes. *Chemical Communications*, pages 393–401, 2002.

[39] J. J. Davis, D. A. Morgan, C. L. Wrathmell, D. N. Axford, J. Zhao, and N. Wang. Molecular bioelectronics. *Journal of Materials Chemistry*, 15(22):2160–2174, 2005.

[40] J. J. Davis, D. A. Morgan, C. L. Wrathmell, and A. Zhao. Scanning probe technology in metalloprotein and biomolecular electronics. *IEE Proceedings Nanobiotechnology*, 151(2):37–47, 2004.

[41] J. J. Davis, C. L. Wrathmell, J. Zhao, and J. Fletcher. The tunnelling conductance of molecularly ordered metalloprotein arrays. *Journal of Molecular Recognition*, 17(3):167–173, 2004.

[42] I. Delfino, B. Bonanni, L. Andolfi, C. Baldacchini, A. R. Bizzarri, and S. Cannistraro. Yeast cytochrome *c* integrated with electronic elements: A nanoscopic and spectroscopic study down to single-molecule level. *Journal of Physics Condensed Matter*, 19(22), 2007.

[43] E. A Della Pia, Q. Chi, D. D. Jones, J. E. Macdonald, J. Ulstrup, and M. Elliott. Single-molecule mapping of long-range electron transport for a cytochrome b_{562} variant. *Nano Letters*, 11(1):176–182, 2011.

[44] M. M. Dovek, M. J. Heben, S. Lewis Nathan, R. M. Penner, and C. F. Quate. *Applications of Scanning Tunneling Microscopy to Electrochemistry*, chapter 14, pages 174–201.

[45] M. J. Eddowes and H. A. O. Hill. Novel method for the investigation of the electrochemistry of metalloproteins: Cytochrome *c*. *Journal of the Chemical Society, Chemical Communications*, pages 771b–772, 1977.

[46] M. J. Eddowes, H. A. O. Hill, and K. Uosaki. The electrochemistry of cytochrome *c*. investigation of the mechanism of the 4,4'-bipyridyl surface modified gold electrode. *Journal of Electroanalytical Chemistry*, 116(C):527–537, 1980.

[47] W. R. Edwards, K. Busse, R. K. Allemann, and D. D. Jones. Linking the functions of unrelated proteins using a novel directed evolution domain insertion method. *Nucleic acids research*, 36(13), 2008.

[48] W. R. Edwards, A. J. Williams, J. L. Morris, A. J. Baldwin, R. K. Allemann, and D. D. Jones. Regulation of β-lactamase activity by remote binding of heme: Functional coupling of unrelated proteins through domain insertion. *Biochemistry*, 49(31):6541–6549, 2010.

[49] Y. Feng and S. G. Sligar. Effect of heme binding on the structure and stability of escherichia coli apocytochrome b_{562}. *Biochemistry*, 30(42):10150–10155, 1991.

[50] Y. Feng, S. G. Sligar, and J. Wand. Solution structure of apocytochrome b_{562}. *Nature Structural Biology*, 1:30–35, 1994.

[51] V. E. V. Ferrero, L. Andolfi, G. Di Nardo, S. J. Sadeghi, A. Fantuzzi, S. Cannistraro, and G. Gilardi. Protein and electrode engineering for the covalent immobilization of p450 bmp on gold. *Analytical Chemistry*, 80(22):8438–8446, 2008.

[52] M. C. Findlay, L. C. Dickinson, and J. C. W. Chien. Copper-cytochrome c. *Journal of the American Chemical Society*, 99(15):5168–5173, 1977.

[53] E. P. Friis, J. E. T. Andersen, L. L. Madsen, P. Mï¿½ller, and J. Ulstrup. In situ stm and afm of the copper protein pseudomonas aeruginosa azurin. *Journal of Electroanalytical Chemistry*, 431(1):35–38, 1997.

[54] P. Garcia, M. Bruix, M. Rico, S. Ciofi-Baffoni, L. Banci, M. C. Ramachandra Shastry, H. Roder, T. De Lumley Woodyear, C. M. Johnson, A. R. Fersht, and P. D. Barker. Effects of heme on the structure of the denatured state and folding kinetics of cytochrome b_{562}. *Journal of Molecular Biology*, 346(1):331–344, 2005.

[55] A. W. Ghosh, P. S. Damle, S. Datta, and A. Nitzan. Molecular electronics: Theory and device prospects. *MRS Bulletin*, 29(6):391–395+383, 2004.

[56] G. Gilardi, A. Fantuzzi, and S. J. Sadeghi. Engineering and design in the bioelectrochemistry of metalloproteins. *Current opinion in structural biology*, 11(4):491–499, 2001.

[57] M. Gouterman and P. Sayer. Solution absorption and luminescence studies of tetraphenylboron, -carbon, -silicon, -germanium, -tin, -lead, -phosphorus, -arsenic, and -antimony. *Journal of Molecular Spectroscopy*, 53(3):319–335, 1974.

[58] H. B. Gray and J. R. Winkler. *Electron transfer in proteins*, volume 65 of *Annual Review of Biochemistry*. 1996.

[59] H. B. Gray and J. R. Winkler. Electron tunneling in structurally engineered proteins. *Journal of Electroanalytical Chemistry*, 438(1-2):43–47, 1997.

[60] H. B. Gray and J. R. Winkler. Electron tunneling through proteins. *Quarterly reviews of biophysics*, 36(3):341–372, 2003.

[61] H. B. Gray and J. R. Winkler. Electron flow through metalloproteins. *Biochimica et Biophysica Acta - Bioenergetics*, 1797(9):1563–1572, 2010.

[62] Joseph E. Griffith and David A. Grigg. Dimensional metrology with scanning probe microscopes. *Journal of Applied Physics*, 74(9):R83–R109, 1993.

[63] David Griffiths. *Introduction to Quantum Mechanics*. 2nd edition edition, 2005.

[64] J. D. Gwyer, J. Zhang, J. N. Butt, and J. Ulstrup. Voltammetry and in situ scanning tunneling microscopy of cytochrome c nitrite reductase on au(111) electrodes. *Biophysical journal*, 91(10):3897–3906, 2006.

[65] W. Haiss, S. Martin, E. Leary, H. Van Zalinge, S. J. Higgins, L. Bouffier, and R. J. Nichols. Impact of junction formation method and surface roughness on single molecule conductance. *Journal of Physical Chemistry C*, 113(14):5823–5833, 2009.

[66] W. Haiss, R. J. Nichols, S. J. Higgins, D. Bethell, H. Heibenreich, and D. J. Schiffrin. Wiring nanoparticles with redox molecules. *Faraday discussions*, 125:179–194, 2004.

[67] W. Haiss, R. J. Nichols, H. Van Zalinge, S. J. Higgins, D. Bethell, and D. J. Schiffrin. Measurement of single molecule conductivity using the spontaneous formation of molecular wires. *Physical Chemistry Chemical Physics*, 6(17):4330–4337, 2004.

[68] W. Haiss, C. Wang, I. Grace, A. S. Batsanov, D. J. Schiffrin, S. J. Higgins, M. R. Bryce, C. J. Lambert, and R. J. Nichols. Precision control of single-molecule electrical junctions. *Nature Materials*, 5(12):995–1002, 2006.

[69] K. Hamada, P. H. Bethge, and F. S. Mathews. Refined structure of cytochrome b_{562} from escherichia coli at 1.4 å resolution. *Journal of Molecular Biology*, 247(5):947–962, 1995.

[70] A. Hamelin and A. M. Martins. Cyclic voltammetry at gold single-crystal surfaces. part 2. behaviour of high-index faces. *Journal of Electroanalytical Chemistry*, 407(1-2):13–21, 1996.

[71] A. G. Hansen, A. Boisen, J. U. Nielsen, H. Wackerbarth, I. Chorkendorff, J. E. T. Andersen, J. Zhang, and J. Ulstrup. Adsorption and interfacial electron transfer of saccharomyces cerevisiae yeast cytochrome c monolayers on au(111) electrodes. *Langmuir*, 19(8):3419–3427, 2003.

[72] M. N. Hasan, C. Kwakernaak, W. G. Sloof, W. R. Hagen, and H. A. Heering. Pyrococcus furiosus 4fe-ferredoxin, chemisorbed on gold, exhibits gated reduction and ionic strength dependent dimerization. *Journal of Biological Inorganic Chemistry*, 11(5):651–662, 2006.

[73] J. He, O. Sankey, M. Lee, N. Tao, X. Li, and S. Lindsay. Measuring single molecule conductance with break junctions. *Faraday discussions*, 131:145–154, 2006.

[74] K. W. Hipps. Molecular electronics: It's all about contacts. *Science*, 294(5542):536–537, 2001.

[75] I. Horcas, R. Fernandez, J. M. Gomez-Rodriguez, J. Colchero, J. Gimez-Herrero, and A. M. Baro. Wsxm: A software for scanning probe microscopy and a tool for nanotechnology. *Review of Scientific Instruments*, 78(1), 2007.

[76] E. Itagaki and L. P. Hager. Studies on cytochrome b_{562} of escherichia coli. i. purification and crystallization of cytochrome b_{562}. *Journal of Biological Chemistry*, 241(16):3687–3695, 1966.

[77] M. Jayadevaiah and V. Lakshminaraya nan. Design of a compact scanning tunneling microscope with a feedback to coarse approach controller for low scan ranges. *Measurement Science and Technology*, 15(5):N35–N38, 2004.

[78] D. D. Jones and P. D. Barker. Design and characterisation of an artificial dna-binding cytochrome. *ChemBioChem*, 5(7):964–971, 2004.

[79] D. D. Jones and P. D. Barker. Controlling self-assembly by linking protein folding, dna binding, and the redox chemistry of heme. *Angewandte Chemie - International Edition*, 44(39):6337–6341, 2005.

[80] A. M. Kuznetsov and J. Ulstrup. Dissipative relaxation of a low-energy intermediate electronic state in three-level electron transfer. *Chemical Physics*, 157(1-2):25–33, 1991.

[81] K. S. Kwok and J. C. Ellenbogen. Moletronics: Future electronics. *Materials Today*, 5(2):28–37, 2002.

[82] A. A. Lamola, J. Eisinger, and W. E. Blumberg. Quantitative determination of erythrocyte zinc protoporphyrin. *Journal of Laboratory and Clinical Medicine*, 89(4):881–890, 1977. Cited By (since 1996): 6.

[83] R. V. Lapshin. Automatic drift elimination in probe microscope images based on techniques of counter-scanning and topography feature recognition. *Measurement Science and Technology*, 18(3):907–927, 2007.

[84] E. Laviron. General expression of the linear potential sweep voltammogram in the case of diffusionless electrochemical systems. *Journal of Electroanalytical Chemistry*, 101(1):19–28, 1979.

[85] E. Laviron. The use of linear potential sweep voltammetry and of a.c. voltammetry for the study of the surface electrochemical reaction of strongly adsorbed systems and of redox modified electrodes. *Journal of Electroanalytical Chemistry*, 100(C):263–270, 1979.

[86] C. Li, I. Pobelov, T. Wandlowski, A. Bagrets, A. Arnold, and F. Evers. Charge transport in single au-alkanedithiol-au junctions: Coordination geometries and conformational degrees of freedom. *Journal of the American Chemical Society*, 130(1):318–326, 2008.

[87] X. Li, J. He, J. Hihath, B. Xu, S. M. Lindsay, and N. Tao. Conductance of single alkanedithiols: Conduction mechanism and effect of molecule-electrode contacts. *Journal of the American Chemical Society*, 128(6):2135–2141, 2006.

[88] Z. Li, I. Pobelov, B. Han, T. Wandlowski, A. Blaszczyk, and M. Mayor. Conductance of redox-active single molecular junctions: An electrochemical approach. *Nanotechnology*, 18(4), 2007.

[89] K. Liu, X. Wang, and F. Wang. Probing charge transport of ruthenium-complex-based molecular wires at the single-molecule level. *ACS Nano*, 2(11):2315–2323, 2008.

[90] K. K. Lo, L. Wong, and H. A. O. Hill. Surface-modified mutants of cytochrome p450(cam): Enzymatic properties and electrochemistry. *FEBS letters*, 451(3):342–346, 1999.

[91] S. Martin, D. Z. Manrique, V. M. Garcia-Surez, W. Haiss, S. J. Higgins, C. J. Lambert, and R. J. Nichols. Adverse effects of asymmetric contacts on single molecule conductances of hs(ch2)n cooh in nanoelectrical junctions. *Nanotechnology*, 20(12), 2009.

[92] Y. Mie, F. Mizutani, T. Uno, C. Yamada, K. Nishiyama, and I. Taniguchi. Direct electrochemistry of engineered cytochrome b_{562} molecules with a ligand binding pocket. *Journal of inorganic biochemistry*, 99(5):1245–1249, 2005.

[93] J. Moreland and J. W. Ekin. Electron tunneling into superconducting filaments using mechanically adjustable barriers. *Applied Physics Letters*, 47(2):175–177, 1985.

[94] R. Mukhopadhyay. Molecular level structural studies of metalloproteins/metalloenzymes by scanning tunnelling microscopy: scopes and promises. *Current Science*, 9(84):1202–1210, 2003.

[95] R. Mukhopadhyay. Kctcca, a peptide-based facilitator for bioelectrochemistry. *Journal of Biosciences*, 29(2):163–167, 2004.

[96] R. Mukhopadhyay, J. J. Davis, P. Kyritsis, H. A. O. Hill, and J. Meyer. A scanning tunnelling microscopy study of clostridium pasteurianum rubredoxin. *Journal of inorganic biochemistry*, 78(3):251–254, 2000.

[97] R. Mukhopadhyay, L. L. Wong, K. K. Lo, T. Pochapsky, and H. A. O. Hill. A molecular level study of complex formation between putidaredoxin and cytochrome p450 by scanning tunnelling microscopy. *Physical Chemistry Chemical Physics*, 4(4):641–646, 2002.

[98] R. J. Nichols, W. Haiss, S. J. Higgins, E. Leary, S. Martin, and D. Bethell. The experimental determination of the conductance of single molecules. *Physical Chemistry Chemical Physics*, 12(12):2801–2815, 2010.

[99] K. Niki, W. R. Hardy, M. G. Hill, H. Li, J. R. Sprinkle, E. Margoliash, K. Fujita, R. Tanimura, N. Nakamura, H. Ohno, J. H. Richards, and H. B. Gray. Coupling to lysine-13 promotes electron tunneling through carboxylate-terminated alkanethiol self-assembled monolayers to cytochrome c. *Journal of Physical Chemistry B*, 107(37):9947–9949, 2003.

[100] H. Nikkila, R. B. Gennis, and S. G. Sligar. Cloning and expression of the gene encoding the soluble cytochrome b_{562} of escherichia coli. *European Journal of Biochemistry*, 202(2):309–313, 1991.

[101] I. V. Pobelov, Z. Li, and T. Wandlowski. Electrolyte gating in redox-active tunneling junctions - an electrochemical stm approach. *Journal of the American Chemical Society*, 130(47):16045–16054, 2008.

[102] D. W. Pohl and R. Miller. "tracking" tunneling microscopy. *Review of Scientific Instruments*, 59(6):840–842, 1988.

[103] C. R. Robinson, Y. Liu, J. A. Thomson, J. M. Sturtevant, and S. G. Sligar. Energetics of heme binding to native and denatured states of cytochrome b_{562}. *Biochemistry*, 36(51):16141–16146, 1997.

[104] A. V. Rudnev, I. V. Pobelov, and T. Wandlowski. Structural aspects of redox-mediated electron tunneling. *Journal of Electroanalytical Chemistry*, 2010.

[105] J. Sambrook and E. F. Fritsch. *Molecular cloning: a laboratory manual*. Cold Spring Harbor Laboratory Press, Cold Spring Harbor, 1989.

[106] W. Schmickler and N. Tao. Measuring the inverted region of an electron transfer reaction with a scanning tunneling microscope. *Electrochimica Acta*, 42(18):2809–2815, 1997.

[107] P. Schmuki and S. Virtanen. *Electrochemistry at the Nanoscale*. Springer, 2009.

[108] G. Sedghi, K. Sawada, L. J. Esdaile, M. Hoffmann, H. L. Anderson, D. Bethell, W. Haiss, S. J. Higgins, and R. J. Nichols. Single molecule conductance of porphyrin wires with ultralow attenuation. *Journal of the American Chemical Society*, 130(27):8582–8583, 2008.

[109] J. M. Shifman, B. R. Gibney, R. E. Sharp, and P. L. Dutton. Heme redox potential control in de novo designed four-a-helix bundle proteins. *Biochemistry*, 39(48):14813–14821, 2000.

[110] J. G. Simmons. Low-voltage current-voltage relationship of tunnel junctions. *Journal of Applied Physics*, 34(1):238–239, 1963.

[111] S. L. Springs, S. E. Bass, G. Bowman, I. Nodelman, C. E. Schutt, and G. L. McLendon. A multigeneration analysis of cytochrome b_{562} redox variants: Evolutionary strategies for modulating redox potential revealed using a library approach. *Biochemistry*, 41(13):4321–4328, 2002.

[112] S. L. Springs, S. E. Bass, and G. L. McLendon. Cytochrome b_{562} variants: A library for examining redox potential evolution. *Biochemistry*, 39(20):6075–6082, 2000.

[113] G. Staikov and W. J. Lorenz. *Electrochemistry and Nanotechnology*, pages 13–25. Wiley-VCH Verlag GmbH, 2007.

[114] P. Steinmann and J. M. R. Weaver. Nanometer-scale gaps between metallic electrodes fabricated using a statistical alignment technique. *Applied Physics Letters*, 86(6):1–3, 2005.

[115] S. Takeda, N. Kamiya, R. Arai, and T. Nagamune. Design of an artificial light-harvesting unit by protein engineering: Cytochrome b_{562}-green fluorescent protein chimera. *Biochemical and biophysical research communications*, 289(1):299–304, 2001.

[116] N. Tao. Measurement and control of single molecule conductance. *Journal of Materials Chemistry*, 15(32):3260–3263, 2005.

[117] N. J. Tao. Probing potential-tuned resonant tunneling through redox molecules with scanning tunneling microscopy. *Phys. Rev. Lett.*, 76(21):4066–4069, May 1996.

[118] N. J. Tao. Electron transport in molecular junctions. *Nature nanotechnology*, 1(3):173–181, 2006.

[119] A. V. Tivanski, Y. He, E. Borguet, H. Liu, G. C. Walker, and D. H. Waldeck. Conjugated thiol linker for enhanced electrical conduction of gold-molecule contacts. *Journal of Physical Chemistry B*, 109(12):5398–5402, 2005.

[120] R. M. Tromp. Spectroscopy with the scanning tunnelling microscope: A critical review. *Journal of Physics: Condensed Matter*, 1(51):10211–10228, 1989.

[121] B. Ulgut and H. D. Abruï¿½a. Electron transfer through molecules and assemblies at electrode surfaces. *Chemical reviews*, 108(7):2721–2736, 2008.

[122] L. E. C. Van De Leemput and H. Van Kempen. Scanning tunnelling microscopy. *Reports on Progress in Physics*, 55(8):1165–1240, 1992.

[123] H. Van Zalinge, D. J. Schiffrin, A. D. Bates, W. Haiss, J. Ulstrup, and R. J. Nichols. Single-molecule conductance measurements of single- and double-stranded dna oligonucleotides. *ChemPhysChem*, 7(1):94–98, 2006.

[124] A. Vilan. Analyzing molecular current-voltage characteristics with the simmons tunneling model: Scaling and linearization. *Journal of Physical Chemistry C*, 111(11):4431–4444, 2007.

[125] A. Vilan and D. Cahen. How organic molecules can control electronic devices. *Trends in biotechnology*, 20(1):22–29, 2002.

[126] G. von Jagow and W. Sebald. b-type cytochromes. *Annual Review of Biochemistry*, 49:281–314, 1980. Cited By (since 1996): 6.

[127] Z. Wang, N. R. Kumar, and D. K. Srivastava. A novel spectroscopic titration method for determining the dissociation constant and stoichiometry of protein-ligand complex. *Analytical Biochemistry*, 206(2):376–381, 1992.

[128] Roland Wiesendanger. *Scanning Probe Microscopy and Spectroscopy: Methods and Applications*. Cambridge University Press, 1994.

[129] X. Xiao, B. Xu, and N. Tao. Conductance titration of single-peptide molecules. *Journal of the American Chemical Society*, 126(17):5370–5371, 2004.

[130] X. Xiao, B. Xu, and N. J. Tao. Measurement of single molecule conductance: Benzenedithiol and benzenedimethanethiol. *Nano Letters*, 4(2):267–271, 2004.

[131] S. Yasuda, S. Yoshida, J. Sasaki, Y. Okutsu, and T. Nakamura. Bond fluctuation of s/se anchoring observed in single-molecule conductance measurements using the point contact method with scanning tunnelling microscopy. *J. Am. Chem. Soc*, 128:7746–7747, 2006.

[132] P. Zahl, T. Wagner, R. Mï¿½ller, and A. Klust. Open source scanning probe microscopy control software package gxsm. *Journal of Vacuum Science and Technology B: Microelectronics and Nanometer Structures*, 28(3), 2010.

[133] J. Zhang, Q. Chi, T. Albrecht, A. M. Kuznetsov, M. Grubb, A. G. Hansen, H. Wackerbarth, A. C. Welinder, and J. Ulstrup. Electrochemistry and bio-electrochemistry towards the single-molecule level: Theoretical notions and systems. *Electrochimica Acta*, 50(15):3143–3159, 2005.

[134] J. Zhang, Q. Chi, A. M. Kuznetsov, A. G. Hansen, H. Wackerbarth, H. E. M. Christensen, J. E. T. Andersen, and J. Ulstrup. Electronic properties of functional biomolecules at metal/aqueous solution interfaces. *Journal of Physical Chemistry B*, 106(6):1131–1152, 2002.

[135] J. Zhang, Q. Chi, J. U. Nielsen, E. P. Friis, J. E. T. Andersen, and J. Ulstrup. Two-dimensional cysteine and cystine cluster networks on au(111) disclosed by voltammetry and in situ scanning tunneling microscopy. *Langmuir*, 16(18):7229–7237, 2000.

[136] J. Zhang, H. E. M. Christensen, B. L. Ooi, and J. Ulstrup. In situ stm imaging and direct electrochemistry of pyrococcus furiosus ferredoxin assembled on thiolate-modified au(111) surfaces. *Langmuir*, 20(23):10200–10207, 2004.

[137] J. Zhang, A. M. Kuznetsov, I. G. Medvedev, Q. Chi, T. Albrecht, P. S. Jensen, and J. Ulstrup. Single-molecule electron transfer in electrochemical environments. *Chemical reviews*, 108(7):2737–2791, 2008.

[138] X. . Zhou, Y. . Wei, L. Liu, Z. . Chen, J. Tang, and B. . Mao. Extending the capability of stm break junction for conductance measurement of atomic-size nanowires: An electrochemical strategy. *Journal of the American Chemical Society*, 130(40):13228–13230, 2008.

[139] P. Zuo, T. Albrecht, P. D. Barker, D. H. Murgida, and P. Hildebrandt. Interfacial redox processes of cytochrome b_{562}. *Physical Chemistry Chemical Physics*, 11(34):7430–7436, 2009.